PHOTOPHYSICS OF ATOMICALLY THIN MoS_2 DEVICES

Daniele Vella

Doctoral Dissertation
Jožef Stefan International Postgraduate School
Ljubljana, Slovenia

Supervisor: Assoc. Prof. Dr. Christoph Gadermaier, IPS and Jožef Stefan Institute, Ljubljana, Slovenia

Evaluation Board:
Prof. Dr. Viktor Kabanov, Chair, Jožef Stefan Institute, Ljubljana, Slovenia
Asst. Prof. Dr. Miha Škarabot, Member, Jožef Stefan Institute, Ljubljana, Slovenia
Dr. Nataša Vujičić, Member, Institute of Physics, Zagreb, Croatia

MEDNARODNA PODIPLOMSKA ŠOLA JOŽEFA STEFANA
JOŽEF STEFAN INTERNATIONAL POSTGRADUATE SCHOOL



Daniele Vella

PHOTOPHYSICS OF ATOMICALLY THIN MoS_2 DEVICES

Doctoral Dissertation

FOTOFIZIKA ATOMSKO TANKIH MoS_2 NAPRAV

Doktorska disertacija

Supervisor: Assoc. Prof. Dr. Christoph Gadermaier

Ljubljana, Slovenia, November 2016

With love to my son ... sorry but I, mummy and Taras still didn't decide how to name you

Acknowledgments

First of all I would like to express my deepest gratitude to my supervisor Assoc. Prof. Dr. Christoph Gadermaier for giving me the opportunity to grow as a person and as a researcher; for his patience, positivity and great ideas. Even in the difficult moments his "don't give up because what you are doing it is really important" was like a gasoline for me to continue.

I would like to thank Assoc. Prof. Dr. Andras Kis for his availability and his professionalism. At the time when I arrived to Switzerland with my mind full of projects ... he really believed in me and I already knew that my destiny was strongly dependent on this mission. In this part my special thanks go to Dmitry Ovchinnikov, Dr. Dumitru Dumcenco and Kung Yen-Chen, who helped me to realize it. Simone Bertolazzi and Adrien Allen, thank you for your advice.

I would like to express my gratitude to Prof. Giulio Cerullo and Prof. Guglielmo Lanzani and the members of their groups: the doors to their lab were always open for our group and coming back to Italy was always a happy moment for me. Thanks to them I was able to achieve important results and learn a great deal.

I would like to thank Asst. Prof. Dr. Tomaž Mertelj who always has the answer and a practical advice to solve an experimental problem. Thanks to Dr. Nataša Vujičić I was able to work on the setup after spending two days in the laboratory. For critical reading and helping me with the Slovenian part of the manuscript, I would like to thank Dr. Jure Strle. In general I would like to thank the entire Department of Complex Matter for such a nice environment, I felt like at home. I wish to acknowledge the ITN Marie Curie MoWSeS project for the financial support.

Special thanks go to my colleagues Victor, Tania, Matej, Pero ... simply friends. We helped each other during these three years, we discussed a lot, we carried out experiments, we spent several nights in the lab and most importantly, we enjoyed ourselves a lot. I will never forget it. The help of my Italian friends Dr. Giorgio Mirri and Dr. Daniele Biglino is sincerely acknowledged.

But the most beautiful surprise of this experience were Jelena and Taras. I met them at the beginning of my journey in Slovenia and now they are a part of my life. Thank you for that. My warmest thanks go to my parents Nino and Pina and my sister Cristina for their continuous support. Although from far a way they were always following and encouraging me. Grazie.

Abstract

Two-dimensional semiconductors, in particular transition metal dichalcogenides, such as MoS_2, offer vast opportunities for optoelectronics and photonics since they combine easy fabrication and mechanical flexibility with particularly strong light-matter interaction. To explore some open questions related to charge carrier photogeneration and the response of excitonic spectra to electric fields we employ femtosecond microspectroscopy and confocal modulation spectroscopy techniques combined with an in-plane and a transverse electric field, which were set up on purpose for the presented experiments.

The first part of this thesis shows how in monolayer MoS_2, despite its large exciton binding energy of several 100 meV, a moderate in-plane electric field of a few 10 $kVcm^{-1}$ can significantly increase the dissociation yield of electron-hole pairs into charge carriers. As a first step, we show that the photoluminescence (PL) of the MoS_2 FET is progressively quenched upon the application of increasingly strong in-plane electric fields. Subsequently, we perform femtosecond optical pump-probe microspectroscopy to directly monitor the photogenerated electron-hole pairs and the excitons and free carriers arising from their relaxation. For increasing field strengths, we observe an enhanced formation of carriers during the first few ps of the dynamics. This could have a strong implication in the design of new photodetectors and photovoltaic devices based on vertical heterostructures.

Successively, we present a strong transverse electroabsorption signal in a monolayer of the two-dimensional semiconductor MoS_2. We observed an electroabsorption spectrum dominated by an apparent linewidth broadening of around 15% at a modulated voltage of only $V_{pp} = 0.5$ V. Contrary to known variants of the Stark effect, the broadening increases linearly with the applied field strength, and arises from a linear variation of the distance between the strongly overlapping exciton and trion resonances. The achievable modulation depths exceeding 0.1 dB nm^{-1} and the working principle not based on changes in the population of levels bear the scope for extremely compact, ultrafast, energy-efficient electroabsorption modulators for integrated photonics, including on-chip optical communication.

This proof of concept in the monolayer limit opens the way for a possible employment of the principle in a more simple structure based on materials exfoliated in liquid. As a starting point to demonstrate its feasibility we carried out femtosecond optical experiments to study the dynamics of excitons and charges in few-layer MoS_2 flakes from exfoliation in water. We compare samples with different amounts of adsorbed sodium cholate, obtained by repeated washing of the dried flakes. We find that the femtosecond dynamics is remarkably stable against the surfactant adsorption, with a slight increase of the initial exciton quenching occurring during the first few picoseconds as the only appreciable effect.

Povzetek

Dvodimenzionalni polprevodniki, zlasti dihalkogenidi prehodnih kovin, kot je MoS_2, so izjemno obetavni za optoelektroniko in fotoniko, ker združujejo enostavno izdelavo in mehansko prožnost z močno interakcijo med svetlobo in snovjo. Za raziskovanje nekaterih odprtih vprašanj smo uporabili metode femtosekundne mikrospektroskopije in konfokalne modulacijske spektroskopije v vzdolžnem in prečnem električnem polju, ki smo ju namenoma uporabili v predstavljenih eksperimentih.

Prvi del disertacije prikazuje, kako lahko v monoplasti MoS_2, kljub njegovi veliki ekscitonski vezavni energiji več 100 meV, zmerno električno polje nekaj 10 kV cm^{-1} vzdolž plasti znatno poveča izkoristek relaksacije vročih parov elektron-vrzel v proste nosilce naboja. V prvem koraku pokažemo, da se fotoluminiscenca MoS_2 poljskih tranzistorjev z naraščajočim vzdolžnim električnim poljem čedalje bolj zmanjšuje. Nato smo izvedli femtosekundno optično črpalno-testno mikrospektroskopijo za neposredno opazovanje fotogeneriranih parov elektron-vrzel in nosilcev naboja, ki nastajajo iz njihove relaksacije. Pri močnejših poljih opažamo povečano nastajanje nosilcev v prvih nekaj pikosekundah dinamike. To ima lahko močne posledice na razvoj novih fotodetektorjev in fotovoltaičnih naprav, osnovanih na vertikalnih heterostrukturah.

Nadalje predstavimo močno prečno elektroabsorpcijo signala v monoplasti dvodimenzionalnega polprevodnika MoS_2. Opazili smo, da je elektroabsorpcijski spekter dominiran z navidezno razširitvijo spektralne črte za okrog 15% pri modulirani napetosti zgolj V_{pp} = 0,5 V. Nasprotno od različic Starkovega efekta se razširitev povečuje linearno z jakostjo električnega polja in je pravzaprav posledica linearnega razmikanja močno prekrivanih ekscitonske in trionske resonance. Dosežena modulacijska globina, ki presega 0,1 dB nm^{-1}, in princip delovanja, ki ni osnovan na spremembah zasedenosti nivojev, omogočata razvoj izjemno kompaktnih, ultrahitrih, energijsko učinkovitih elektroabsorpcijskih modulatorjev za integrirano fotoniko, tudi z optično komunikacijo na čipu.

Omenjeni dokaz koncepta v monoplastni limiti odpira možnosti za uporabo takega delovanja v bolj enostavnih strukturah, osnovanih na materialih, ki jih eksfoliiramo v tekočini. Za začetek smo kot prikaz izvedljivosti opravili več femtosekundnih optičnih eksperimentov, s katerimi smo raziskovali dinamiko ekscitonov in nabojev v nekajplastnih luskah MoS_2 eksfoliiranih v vodi. Primerjali smo vzorce z različnimi količinami adsorbiranega natrijevega holata, dobljene z večkratnim spiranjem suhih lusk. Odkrili smo, da je femtosekundna dinamika izjemno stabilna glede na adsorpcijo surfaktantov, z blagim povečanjem začetnega ekscitonskega gašenja v prvih nekaj pikosekundah kot edino opaženo razliko.

Contents

List of Figures **xv**

List of Tables **xvii**

Abbreviations **xix**

1 Introduction **1**
1.1 Motivation . . . 1
1.2 Transition Metal Dichalcogenides: Overview . . . 2
1.3 Crystal and Electronic Structure of MoS_2 . . . 4
1.3.1 Crystal structure . . . 4
1.3.2 Electronic structure . . . 7
1.3.3 Lattice vibrations . . . 8
1.4 Optical Properties . . . 10
1.4.1 Electrical tuning of the optical properties . . . 11
1.5 Time-Resolved Optical Response . . . 14
1.6 Device Applications . . . 18
1.6.1 Field effect transistors . . . 18
1.6.2 Single layer MoS_2 transistors . . . 20
1.6.3 Digital electronics . . . 22
1.6.4 Optoelectronic devices . . . 23

2 Device Fabrication and Experimental Techniques **25**
2.1 Single Layer MoS_2 Field effect Transistor: Microfabrication . . . 25
2.1.1 Wet transfer techniques . . . 26
2.1.2 Transport measurements . . . 29
2.2 Transient Transmission Spectroscopies . . . 31
2.3 Ultrashort Laser Pulses . . . 32
2.4 Nonlinear Optics for Transient Spectroscopies . . . 34
2.4.1 White light generation . . . 35
2.4.2 Second harmonic generation (SHG) . . . 36
2.5 Pump-Probe Setup . . . 37
2.5.1 Pump-probe microscope . . . 39
2.6 Modulation Spectroscopy . . . 40
2.7 Equipment for Basic Optical Characterizations . . . 41

3 Field-Induced Charge Separation in Monolayer MoS_2 **43**
3.1 Introduction . . . 43
3.2 Photoluminescence and Electric Field . . . 44
3.3 Femtosecond Optical Spectroscopy and Electric Field . . . 45
3.4 Photoluminescence Consideration . . . 49
3.5 Pump-Probe Fluence Consideration . . . 51

4 Electroabsorption in Monolayer MoS_2 **53**
4.1 Unconventional Electroabsorption in Monolayer MoS_2 53
4.2 Experimental Resuls 54
4.3 Origin of the Electroabsorption Signal 55
4.3.1 Discussion of Possible Origins of the Electroabsorption Signal 57
4.4 Electrostatic Consideration 58
4.5 Assessing the Use in an Electroabsorption Modulator 61
4.6 Possible Strategies to Increase the EA Signal 62

5 Femtosecond Spectroscopy on MoS_2 Flakes from Liquid Exfoliation: Surfactant Independent Exciton Dynamics **65**
5.1 Introduction to the Topic 65
5.2 Sample Preparation 66
5.3 Results and Discussion 66

6 Conclusions **73**

Appendix A Electroabsorption: Supplementary Materials **75**
A.1 Surface Analysis of the Transfer Method 75
A.2 Details and Accuracy of the Used Fits 77

References **83**

Bibliography **97**

Biography **99**

List of Figures

Figure 1.1: Mechanically exfoliated flakes. . . . 3
Figure 1.2: Chemical vapor deposition and liquid exfoliation processing. . . . 5
Figure 1.3: Crystal structure and polytypes of MoS_2. . . . 6
Figure 1.4: Band structure of MoS_2. . . . 7
Figure 1.5: Lattice dynamics of MoS_2. . . . 9
Figure 1.6: Optical properties of mono- and few layer MoS_2. . . . 10
Figure 1.7: Excitonic Rydberg series for single layer WS_2. . . . 12
Figure 1.8: Electrical tuning of the optical properties in monolayer MoS_2 and WS_2 . 13
Figure 1.9: Transient absorption spectra of MoS_2. . . . 16
Figure 1.10: Short channel effects. . . . 19
Figure 1.11: Single layer MoS_2 FET. . . . 21
Figure 1.12: Logic inverter based on a single layer of MoS_2. . . . 22
Figure 1.13: Optoelectronics based on a single layer of MoS_2. . . . 24

Figure 2.1: Schematic of the transistor geometry. . . . 26
Figure 2.2: Process flow of the transfer method based on PMMA and KOH. The sketch inside the blue square is a variation of the method if HfO_2 is used as a gate oxide. . . . 26
Figure 2.3: AFM on CVD MoS_2. . . . 27
Figure 2.4: Process flow for the realization of the strips made from glass/PDMS/PLLA/flakes employed in the PLLA transfer method. . . . 28
Figure 2.5: Manipulator for transfer nanomaterials. . . . 29
Figure 2.6: Electrical characteristic of a 1L-MoS_2 FET in air. . . . 30
Figure 2.7: Electrical characteristic of a 1L-MoS_2 FET in vacuum. . . . 31
Figure 2.8: Three level system: one ground state and two excited states. . . . 32
Figure 2.9: Absorption and emission spectra of the Ti:sapphire laser. . . . 33
Figure 2.10: Mode-locking. . . . 33
Figure 2.11: White light generation. . . . 35
Figure 2.12: Schematic illustration of a pump-probe experiment. . . . 38
Figure 2.13: Pump-probe setup. . . . 38
Figure 2.14: Pump-probe microscopy setup 39
Figure 2.15: Electroabsorption setup 40

Figure 3.1: FET used for the experiment of field induced dissociation. . . . 44
Figure 3.2: Photoluminescence and electric field. . . . 45
Figure 3.3: Pump-probe microspectroscopy. . . . 46
Figure 3.4: Spectral contribution from the cascade model fit. . . . 47
Figure 3.5: Pump-probe signal and electric field. . . . 48
Figure 3.6: Excitonic PL increasing with the bias voltage. . . . 50
Figure 3.7: Pump-probe microspectroscopy: comparison real data and fit at 5V . . 52

Figure 4.1: Optical and electrical characterization of monolayer MoS_2 transistors. . 54
Figure 4.2: Electroabsorption spectra of monolayer MoS_2 transistors. 56
Figure 4.3: Electroabsorption and transmission maps of monolayer MoS_2 transistors. 60
Figure 4.4: Simulation: Absorption spectra with and without field 63

Figure 5.1: Optical density of MoS_2 thin films 67
Figure 5.2: Raman characterization of MoS_2 thin films 68
Figure 5.3: Pump-probe spectra of few layer MoS_2 69
Figure 5.4: Pump-probe dynamics of few layer MoS_2 70

Figure A.1: AFM topographical image of the HfO_2. 75
Figure A.2: AFM topography image of a single layer of MoS_2 transferred with PLLA. 76
Figure A.3: First and second derivative fits of the EA signal. 77
Figure A.4: First and second derivative fits of the EA signal: $A + \Delta A$. 79
Figure A.5: Fits EA signal–Device 2– with separate A^0 exciton and A^- trion. . . . 80
Figure A.6: Fits EA signal–Device 1– with separate A^0 exciton and A^- trion. . . . 81

List of Tables

Table 1.1: Properties of TMDCs. 3

Table A.1: Linear combination fit coefficients. 78

Abbreviations

1L ... single layer
2D ... two-dimensional
3D ... three-dimensional
AFM ... atomic force microscope
ALD ... atomic layer deposition
BBO ... beta barium borate
CBS ... conduction band splitting
CPG ... charge carrier photogeneration
CCD ... charge-coupled device
CVD ... chemical vapor deposition
CMOS ... complementary metal-oxide-semiconductor
CB ... conduction band
DFT ... density functional theory
DI ... deionized
DC ... direct current
EA ... electroabsorption
EAM ... electroabsorption modulators
EMIM ... 1-ethyl-3-methylimidazolium
FET ... field effect transistor
FWHM ... full width at half maximum
IL ... insertion loss
IPA ... isopropanol
ITO ... indium tin oxide
ITRS ... international technology roadmap for semiconductors
MD ... modulation depth
NA ... numerical aperture
OD ... optical density
PB ... photobleaching
PA ... photoinduced absorption
PL ... photoluminescence
PDMS ... polydimethylsiloxane
PLLA ... poly(L-lactic acid)
PMMA ... polymethyl methacrylate
QCSE ... quantum confined Stark effect
QY ... quantum yield
RT ... room temperature
SC ... sodium cholate
SE ... stimulated emission
SF ... self-focusing
SHG ... second harmonic generation
SPM ... self phase modulation

SCE ... short channel effect
SS ... subthreshold swing
SWNT.. single wall carbon nanotubes
TMDC.. transition metal dichalcogenide
TEM ... transmission electron microscope
TFSI ... (trifluoromethylsulfonyl)imide
UV ... ultraviolet
VB ... valence band

Chapter 1

Introduction

1.1 Motivation

For the past half-century silicon-based electronics has been the cornerstone of the technological revolution we see in our daily lives, not just for computing, but also for communications, optoelectronics, photovoltaics and sensors. The exponential growth in computing power and reduction in cost is generally powered by the continued miniaturization of silicon devices as well as dictated by Moore's law [1], currently down to 14 nm. In this context the discovery of graphene [2], [3], a single atomic layer of graphite, has been a groundbreaking discovery in material science, with the potential to create new technology and explore new physics. For the immense novelty of its physical properties, Andre Geim and Konstantin Novoselov were awarded the Nobel Prize in Physics in 2010.

Graphene is considered the first, never reported until 2004, two-dimensional (2D) material, where the confinement of electrons in the vertical dimension gives rise to novel extraordinary properties. However, graphene is only one example among a large number of 2D crystals available in nature. Among these, monolayers of transition metal dichalcogenides (TMDCs), such as MoS_2, WS_2 or WSe_2 provide a broad spectrum of electronic and optical properties alternative to those of graphene; thus, they are also termed as *beyond graphene*.

Because of their properties in the last few years these materials have attracted the attention of researchers worldwide, from the graphene community and elsewhere, leading to a rapid evolution of the field. For instance, while graphene is a zero-gap semimetal, monolayer Mo and W based TMDCs are semiconductors with a direct bandgap ranking between 1–2 eV [4] and are therefore suitable for applications in digital electronic switches and optoelectronic devices. In the last five years, TMDCs and in particular monolayer MoS_2, the best studied TMDC to date, have revealed to be promising semiconductors for proceeding the miniaturization of field effect transistors (FET) beyond the limit of silicon technology. Due to the atomic thickness ($\sim$0.6 nm) and sizeable bandagap, monolayer TMDCs offer the possibility to be implemented in the FET geometry with minimal short-channel effects and low standby power dissipation [5]. The 2D semiconductors gained such considerable attention that the International Technology Roadmap for Semiconductors (ITRS) has included them in the list of emerging research materials already in 2011.

The growth of the research field has shown that TMDCs offer a vast opportunity for optoelectronics, photovoltaics and photonics since they combine flexible processing and easy fabrication [6] with a strong light matter interaction and a large optical absorption in the visible range ($\sim$ 10%) [7], [8]. However, a lot of challenges need to be addressed before the first optoelectronic or photonic components based on 2D TMDCs will step into the market. One critical aspect is that high efficiency solar cells are desired by industry

and TMDCs have been engineered in different ways, from p-n junction diodes [9] to van der Waals heterostructures [10], resulting in the realization of solar cells with a power conversion efficiency ranging from 0.2 to 5% [11], [12], whereas for the actual silicon based technology it is around 30%. Hence, one of the main challenges in the use of 2D TMDCs for optoelectronics applications is to develop a good understanding of exciton dissociation and photoresponse. This issue is essential to the design of structures and devices for efficient optoelectronic devices.

Furthermore, research on 2D material-based light modulators, particularly graphene-based, has already revealed several distinct advantages of 2D material modulation technology such as broad operation bandwidth from the visible to terahertz range, small footprint, low cost, easy integration and large flexibility [13]. All of these characteristics have led to several photonic devices ranging from multifunctional modulator and photodetector [14] to spatial light modulators [15]. In the next years we expect to see, like for graphene, a rapid growth of the research focusing on TMDC-based optical modulators. However, production of large-area and high-quality 2D materials remains a crucial point. If this work out with success, TMDC material-based optical modulators might create a new market to address emerging applications.

The electric field induced separation of hot electron-hole pairs and electroabsorption effect of monolayer MoS_2 in a field effect transistor are the subjects of the present work. Both phenomena are interesting in terms of fundamental physics and practical applications. As I show in this work a moderate in-plane electric field can induce generation of free carriers by increasing the dissociation yield of electron-hole pairs; this could be implemented in the actual generation of 2D van der Waals heterostructures to increase their photoresponse. Later on in this work I show, from a practical point of view, that the electroabsorption in monolayer MoS_2 may enable an electro-optical modulator of sub-wavelength dimensions, that could replace the actual, relatively bulky technology that currently impedes further photonic integration.

1.2 Transition Metal Dichalcogenides: Overview

TMDCs are a class of materials with the formula MX_2, where M is a transition metal element (*e. g.* Mo, W, Nb, Ta, Re), and X is a chalcogen (S, Se or Te). These materials form layered structures, such as X-M-X, with the chalcogen atoms in two hexagonal planes separated by a plane of metal atoms [16], [17] (see Figure 1.1a,b). They are formed by stacks of atomic planes that interact between each other through van der Waals forces, whereas the atoms in each plane are held together by strong covalent bonds. In contrast to graphene, which is a semimetal, several 2D TMDCs possess sizable bandgaps around 1–2 eV [4], becoming a suitable platform for new field-effect transistors [18], digital switches [19] and optoelectronic devices [20]. For instance, monolayer MoS_2 is a semiconductor with a direct bandgap of $\sim$1.8 eV [21], [22], while some other TMDCs exhibit exotic behaviour, such as charge density waves and superconductivity [17], [23] (see Table 1.1).

In the last six years most of the know-how from the graphene community was transferred to the TMDCs leading a rapid evolution of the research field concerning the fundamental physics, applications and material processing. The latter is significant and aims to scale up the production of thin flakes with systematic control of flake thickness and size. As shown in Figure 1.1c,d TMDCs can be peeled from their bulk crystals (mineral or synthetic source) by micromechanical cleavage using adhesive tape [3], [18], [21], [22], [24] and deposited onto Si/SO_2 with an oxide thickness of 270 nm (optimum thickness for the identification by light interference [25], [26]). This method produces single-crystal flakes of high purity for fundamental characterization and single device fabrication, however, it

Table 1.1: Electronic characteristics of different layered TMDCs, classified as a semiconducting, metallic, superconducting or charge density wave (CDW). Adapted from [6].

MX_2	$-S_2$	$-Se_2$	$-Te_2$
Mo	SEMICONDUCTING 1L: 1.8 eV Bulk: 1.2 eV	SEMICONDUCTING 1L: 1.5 eV Bulk: 1.1 eV	SEMICONDUCTING 1L: 1.1 eV Bulk: 1.0 eV
W	SEMICONDUCTING 1L: 1.9 eV Bulk: 1.4 eV	SEMICONDUCTING 1L: 1.7 eV Bulk: 1.2 eV	SEMICONDUCTING 1L: 1.1 eV
Nb	METAL SUPERCONDUCTING CDW	METAL SUPERCONDUCTING CDW	METAL

is not scalable and empiric without any control of the flake thickness and size.

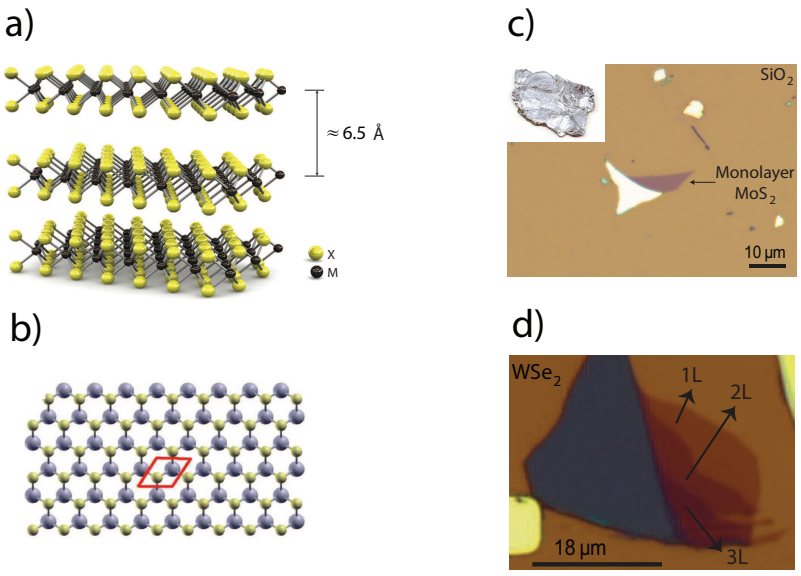


Figure 1.1: a) Schematic representation of a typical MX_2 structure, with the chalcogen atoms (X) in yellow and the metal atoms (M) in grey. b) In-plane structure of monolayer MS_2: Mo (gray) and two overlapped S (yellow) atoms. c) Optical micrographs of MS_2 monolayer mechanically exfoliated on oxidized silicon substrate (270 nm thick SiO_2). d) Optical image of mechanically exfoliated flakes of WSe_2: from three to one layer. a) is adapted from [6], c) from [18].

The most promising method for this purpose is the chemical vapor deposition (CVD), a technique that is widely utilized in the microelectronics industry for the deposition of a broad range of thin films. A lot of CVD methods for growing atomically thin films of MoS_2 on insulating substrates have recently been reported. These methods use different solid precursors like sulphur powder and MoO_3 powder which are vaporized and co-deposited onto a substrate at high temperatures, see Figure 1.2a. In fact, as reported by Y. C. Lin *et al.* [27] the MoO_3 is reduced to MoO_2 through thermal annealing at 500 °C in an Ar/H_2

atmosphere. Afterwards, the samples are exposed to sulphur vapor and a second annealing step at 1000 °C is performed to convert MoO_2 into a thin layer ($\sim$ 2 nm thick) of MoS_2. A similar procedure was reported by Y. Zhan *et al.*, based on the direct sulphurization of a thin layer of Mo metal deposited onto a wafer [28]. Y. H. Lee *et al.* [29] were the first to report on the growth of MoS_2 films with single-layer regions on SiO_2 by using gas-phase reaction of MoO_3 and S powders both vaporized inside a CVD furnace. It was found that special treatment of the surface, such as perylene-3,4,9,10-tetracarboxylic acid tetrapotassium salt (PTAS) molecules, promote nucleation and growth. It is important to note that the merging of islands with different shapes and orientation can bring the formation of grain boundaries that destroy the electrical and mechanical properties of the material. Regarding this problem D. Dumcenco *et al.* [30] made important progress by proving that the lattice orientation during growth can be controlled by engineering the substrate surface. An epitaxial-like growth was observed on the *c*-plane surface of sapphire, which was thermally annealed at 1000 °C in air to produce atomically smooth terraces. The strong van der Waals interaction between the substrate and MoS_2 was found to enable the growth of islands with a limited number of lattice orientations, therefore after merging a large monocrystalline domain (see Figure 1.2b) can be formed with a very low concentration of grain boundaries. Overall, the density of impurities and other defects still represents a bottleneck to transfer this technique into an industrial scenario.

Alternatively, TMDCs can be exfoliated by ultrasonication in appropriate liquids, including organic solvents, aqueous surfactant solutions, or solutions of polymers in solvents [33], [34]. Ultrasonication of the powder material, in bath or with a tip, results in the mechanical exfoliation of the bulk (powder) to give flakes that are a few hundred nanometres in size (see Figure 1.2d). In 2011 J. Coleman *et al.* [32] published a comprehensive study on liquid phase exfoliation of layered compounds. They showed that these materials can be exfoliated through ultrasonication in common organic solvents without the use of intercalated ions. The energy required to exfoliate layered crystals can be quantified from the surface energy, which is the energy to remove a monolayer from the crystal divided by twice the monolayer surface area. By choosing the surface energy of the solvent to be equal to the one of the layered compound it is possible to minimize the enthalpy of exfoliation. The surface energy for the principal TMDC materials was found to be between 65–75 mJ m^{-2}. Successive studies from the same group proved that it is possible to introduce in the liquid exfoliation process the control parameters to select nanosheet size, thickness or concentration. This important step made by C. Backes *et al.* [35] can be applied to a range of two-dimensional materials including MoS_2, WS_2, $MoSe_2$ and WSe_2. Furthermore in another publication they overcome a low yield of monolayer flakes by designing and optimizing a centrifugation cascade (see Figure 1.2c) to enrich liquid exfoliated dispersions, *e. g.* WS_2, up to monolayer contents of 75% [31]. Coleman and coworkers have also demonstrated that layered TMDCs can be mixed with different types of materials in hybrid dispersions and polymer composites [32], [36]. In this context, further progress is expected to enable advanced composite materials and bring TMDCs toward potential low-cost flexible electronics and energy harvesting devices.

1.3 Crystal and Electronic Structure of MoS_2

1.3.1 Crystal structure

The crystal structure of MoS_2 was reported for the first time in 1923 by Dickinson and Pauling [37] who used X-ray diffraction to reveal the hexagonal lattice and the structural parameters of MoS_2. Adjacent layers of MoS_2 are weakly held together to form the bulk crystal in a variety of polytypes. The bulk structure has three different polytypes namely

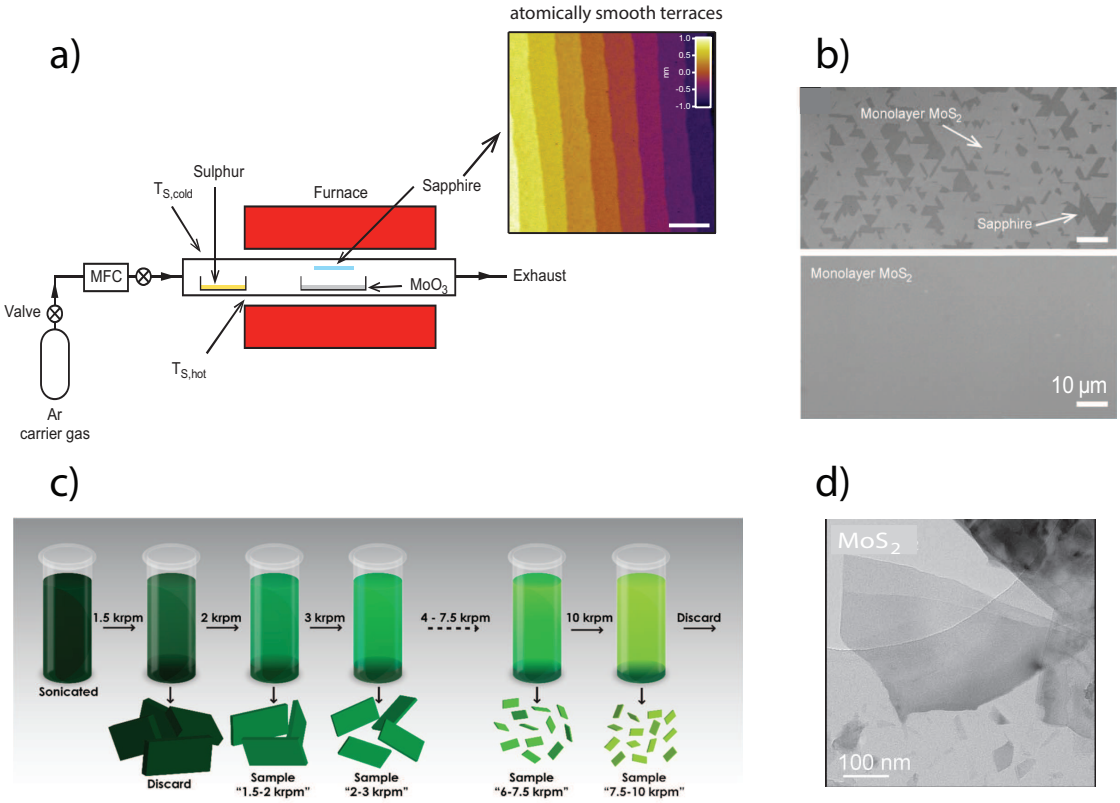


Figure 1.2: a) Schematic drawing of the CVD growth system. b) Optical microscopy images of the CVD MoS_2 show incomplete coverage close to the edges of the chip and full coverage close to the center of the growth substrate. c) Schematic illustration of the basic centrifugation cascade to exfoliate nanosheets. d) Transmission electron microscope image (TEM) of liquid exfoliated flakes. a) and b) are adapted from [30], c) from [31]. d) from [32].

2H, 3R and 1T, as shown in Figure 1.3a. 2H consists of a stack of S-Mo-S layers, where each Mo atom is covalently bonded to six S atoms with two layers per unit cell in hexagonal symmetry while 3R has three layers per unit cell in rhombohedral symmetry. Both polymorphs have the same space group D_{3h} with trigonal prismatic coordination. On the other hand the 1T phase MoS_2 is arranged with only one layer per unit cell with octahedral coordination (O_h) and tetragonal symmetry [6]. In the single layer limit only the two phases 2H and 1T exist (Figure 1.3b), however the most stable phase is 2H which is an intrinsic semiconductor [38]. 3R is uncommon and tends to transform into 2H upon heating [39]; 1T is metastable and has metallic behavior.

The metallic T phase was reported for the first time in 1991 by D. Yang *et al.* [40] who carried out X-ray diffraction and Raman scattering experiments on a single layer of MoS_2 produced by lithium intercalation. They reported that a structural transformation from trigonal prismatic to octahedral coordination occurs when MoS_2 is intercalated by lithium and it was suggested that the transformation is driven by a lowering of the electronic energy for the octahedral structure when electrons are donated from Li to the MoS_2 layers during intercalation [41]. Such chemical exfoliation methods, more recently performed on a wide set of TMDCs, enable the production of submicrometre-sized monolayers with different structural and electronic properties for the bulk materials [42]. For

example MoS_2 changes, in the exfoliation process, the electronic structure from semiconducting to metallic [42], [43], [44]. By annealing at 300 °C it is possible to restore the Mo atom coordination and the semiconducting bandgap of the pristine material, as highlighted by the re-emergence of bandgap photoluminescence[42]. More recently, G. Eda *et al.* revealed through TEM investigations that the 2H and 1T phases can coexist in monolayers obtained through chemical exfoliation and suggest potential for exploiting molecular scale (Figure 1.3c) electronic device designs in atomically thin 2D layers [45]. Moreover, recent reports have also shown the possibility to locally control the crystal structure by inducing phase changing by exposing the flakes to *n*-butyllithium [46] or electron beam irradiation [47].

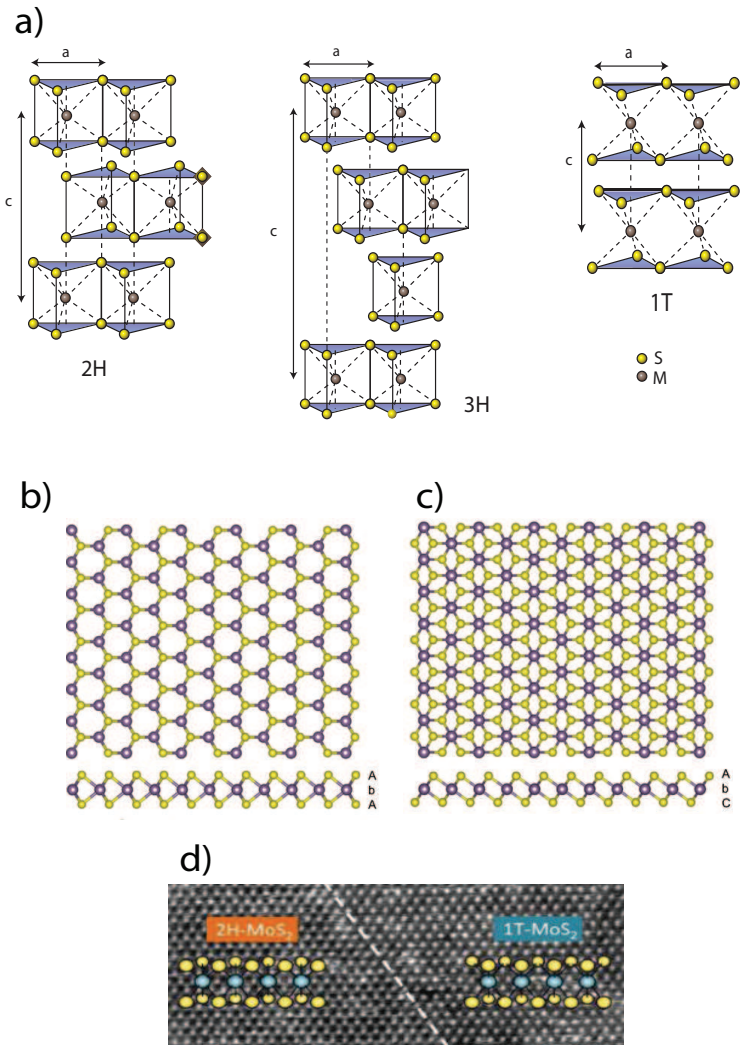


Figure 1.3: a) Schematic illustration of different MoS_2 polytypes: 2H (two layers per repeat unit, hexagonal symmetry, trigonal prismatic coordination), 3R (three layers per repeat unit, rhombohedral symmetry, trigonal prismatic coordination) and 1T (one layer per repeat unit, tetragonal symmetry, octahedral coordination). The lattice constant is $a = 3.16$ and the vertical distance between the molybdenum layers is ∼6.15 Å. Adapted from [6]. b,c) In-plane section of MoS_2 monolayer with trigonal prismatic (b) and octahedral (c) coordination. Adapted from [17]. d) TEM image of monolayer MoS_2 with both 2H and 1T phases [45].

1.3.2 Electronic structure

Bulk MoS_2 is an indirect bandgap semiconductor ($E_g \sim 1.2$ eV) where the valence band (VB) maximum lies at the high-symmetry point Γ and the conduction band (CB) minimum at a low-symmetry point between K and Γ. Calculations [22], [48] suggested that the electronic band structure of the thin TMDC materials depends dramatically on the number of layers, mainly due to the quantum confinement effects [4]. As shown in Figure 1.4a, as the

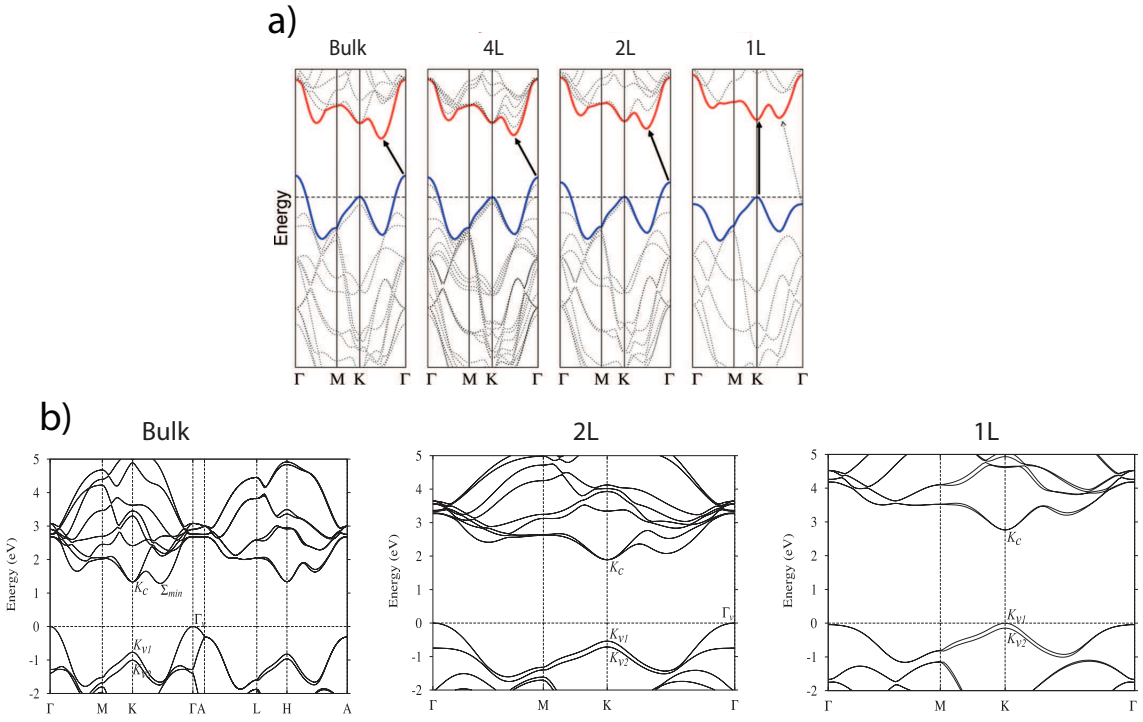


Figure 1.4: a) Evolution of the band structure of MoS_2 with decreasing thickness. From left to right: bulk crystal, four-layer (4L), bilayer (2L) and monolayer (1L). Highest VB (blue) and lowest CB (red). Adapted from [22]. b) Band structures of monolayer, bilayer and bulk of MoS_2, adapted from [49].

number of layers decreases the indirect gap becomes larger, but the direct gap at the K point remains almost unaffected. This leads to the shift in the monolayer towards the K point of both (CB) minimum and (VB) maximum. Moreover, a prominent photoluminescence has been reported to be much stronger in monolayer than in the ticker layers [21], [22]. In addition to quantum confinement, A. Splendiani *et al.* [22] ascribed the change in the band structure to the change in the hybridization between p_z orbitals on S atoms and d orbitals on Mo atoms. Density functional theory (DFT) suggested that the conduction band states at the K-point are mainly due to d orbitals of molybdenum, located in the middle of the sandwich structure S-Mo-S and unaffected by layer coupling. On the other hand, the states near the Γ point are due to the combinations of the anti-bonding p_z-orbitals on the S-atoms and d orbitals on Mo atoms, and have a strong interlayer coupling effect, therefore the transition at the Γ point shifts significantly from indirect to direct bandgap [22]. Similar calculation, by T. Li *et al.*, involves the variation of the orbital compositions of the electronic states [50].

However, recent calculation based on quasiparticle self-consistent *GW* method by T. Chei-

wchanchamnangij *et al.* [49] revealed that also the direct gap changes strongly upon reducing the number of layers. Although both bulk and bilayer MoS_2 have indirect gaps, the smallest gap for the bulk is from Γ to Σ_{min} that is located between the K and Γ points, while for the bilayer is from Γ to K (see Figure 1.4b). In the case of monolayer MoS_2 the direct gap is located at the K point. Therefore, in the bilayer, the CB minimum shifts from Σ to K, but the VB maximum remains at the Γ point. From bilayer to monolayer, the VB maximum shifts from Γ to K. The calculated indirect band gap of the bulk material was found in good agreement with the experimental data [21]. However, the calculated direct gap is about 0.5 eV larger than the optical absorption and fluorescence peaks. Indeed, their calculations revealed the quasiparticle gap (electrical gap), which is offset by the exciton binding energy with respect to the optical gap. Hence, by introducing the Mott-Wannier effective-mass theory, then adding the excitonic effect, they showed that for the monolayer the optical gaps from K_{v1} to K_c and K_{v2} to K_c agree very well with the experimentally reported (by K. F. Mak *et al.*) A and B exciton peaks. Overall they estimated for monolayer an effective Bohr radius of 9.3 Å and an exciton binding energy of 0.897 eV, almost two times bigger than in the bilayer [49]. That reveals an optical bandgap much lower than the quasiparticle bandgap and a strong increase in both the exciton binding energy and the quasiparticle band gap upon reducing the number of the layers. This scenario of the band structures is important to understand the optical properties of TMDC materials presented in Section 1.4.

1.3.3 Lattice vibrations

One of the first experimental investigations of lattice vibration in MoS_2 was carried out by T. J. Wieting and J. L. Verble [51], who reported infrared and Raman measurements in bulk MoS_2. Figure 1.5a shows the calculated phonon dispersion curves [52] as well as the experimental data (black points) obtained with neutron inelastic scattering spectroscopy, measured by N. Wakabayashi *et al.* [53]. The 2H polytype of bulk MoS_2 presents a total of 18 phonon branches, 3 of which are acoustic and 15 are optical. The longitudinal acoustic (LA) and the transverse acoustic (TA) modes have a linear dispersion, near the Γ point of the Brillouin zone, and higher energy than the out of plane acoustic (ZA) mode. ZA displays a q^2 dependence analogous to the ZA mode in graphene. The low-frequency optical modes, namely E^2_{2g} and B^2_{2g} (inactive mode), are found at 35.2 and 57.7 cm^{-1} and correspond to rigid-layer shear and vertical motion, respectively (analogous with the low-frequency optical modes in graphite). The remaining 12 optical phonons are separated from the low-frequency modes by a gap of $\sim$ 220 cm^{-1}. Raman spectroscopy studies identified a total of four Raman-active modes [52], [54], [55]. The most investigated are E^1_{2g} and A_{1g} that correspond to in-plane and out-of-plane vibrations, respectively. On the other hand monolayer MoS_2 has only 3 atoms per unit cell, thus the number of phonon modes is reduced to 9, where 3 branches are acoustic and 6 are optical. The dispersion relation is illustrated in Figure 1.5b. The most significant difference between monolayer and bulk is the absence of low-frequency optical phonons in the monolayer. It is worth to mention that the lack of an inversion center in the monolayer requires the use of a different notation, so that the main investigated Raman-active modes in the monolayer are usually referred to E' (E^1_{2g} in bulk) and A'_1 (A_{1g} in bulk) [55]. Figure 1.5c shows the motion of the optical modes of vibration of monolayer MoS_2 [56]. The first two pairs (from the top figure) are optical phonons that correspond to interlayer shearing modes. The two S planes move whereas the Mo plane is stationary, giving rise to a lattice vibration E'' (E_{1g} in bulk). In the second pair, both S and Mo planes move in counter phase, resulting in a vibration E'. The third pair shows the intralayer breathing mode A'_1, where the S planes vibrate in counter phase along the direction perpendicular to the layer and the Mo plane

is fixed. At the highest frequency another intralayer breathing mode A_2'' (A_{2u} in bulk), where both Mo and S planes participate in the vibration.

The first who investigated the evolution of the Raman signal scaling with the number of the layers down to the monolayer limit were C. Lee *et al.* [57]. They observed that the A_{1g} mode undergoes a red shift as the thickness is reduced from bulk to monolayer due to the presence of lower interlayer interactions, whereas the E^1_{2g} mode blue shifts. The unexpected behaviour of E^1_{2g} suggests a role for the stacking-induced changes in intralayer bonding and/or the presence of Coulombic interlayer interactions in MoS_2 (see Figure 1.5d,e). The most important finding of this research work is that the difference between the frequencies E^1_{2g} and A_{1g} can be used as a reliable parameter to establish the number of layers in a MoS_2 nanosheet. In the monolayer $\Delta\omega$ is usually less than 20 cm^{-1}, and the shift recorded from mono- to bilayer is approximately 3 cm^{-1}. A similar study of Raman metrics on WS_2 [58] revealed a similar trend as observed in MoS_2. The hardening of the A_{1g} mode (blue shift) was found to be consistent with the increasing restoring force caused by van der Waals interactions among layers. The E^1_{2g} phonon mode, however, shows a discrete blue shift when decreasing the number of the layers, but the change in frequency was found to be of the order of magnitude of the error bar. For this reason it is difficult to find for WS_2 a reliable correlation between $\Delta\omega$ and the number of layers. It is worth to mention that the Raman signal, in particular the position and the width, can be affected by several factors, such as thermal [59] and doping [60] influences, as well as strain [61] and the dielectric environment [62].

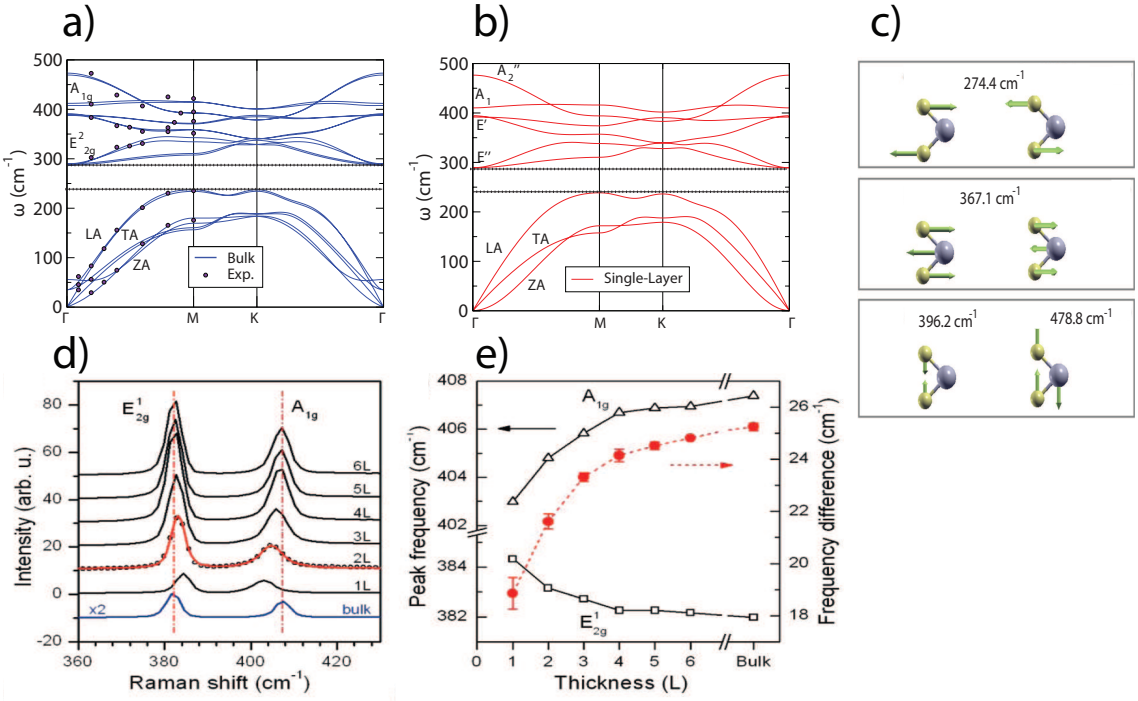


Figure 1.5: a,b) Phonon dispersion curves of bulk (a) and monolayer (b) MoS_2 obtained from DFT calculations. Adapted from [52]. c) Schematics of the 6 optical phonon modes of monolayer MoS_2. In-plane vibrations can be longitudinal (L) or transverse (T). Out-of-plane modes are indicated with Z. Adapted from [56]. d) Raman spectra evolution from bulk to monolayer MoS_2. e) Frequencies of E^1_{2g} and A_{1g} Raman modes and their difference as a function of layer thickness. d) and e) adapted from [57].

1.4 Optical Properties

The optical properties of MoS_2 in bulk form have been investigated for the first time in the 1960's [63], [64], [65]. Successively R. Coehoorn *et al.* carried out a first principle calculation providing an explanation for the presence of two resonant transitions, namely A (1.88 eV) and B (2.06 eV) peaks [66], [67]. These transitions are related to direct interband transitions occurring at the K point of the first Brillouin zone, between the split VB and the CB. The evolution of the optical properties of MoS_2 as a function of the number of layers until the monolayer limit was reported for the first time in 2010 by A. Splendiani *et al.* [22] and by K. F. Mak *et al.* [21]. Photoluminescence (PL) spectra of the MoS_2 crystals exhibit a crossover from an indirect- to a direct gap semiconductor in the monolayer limit.

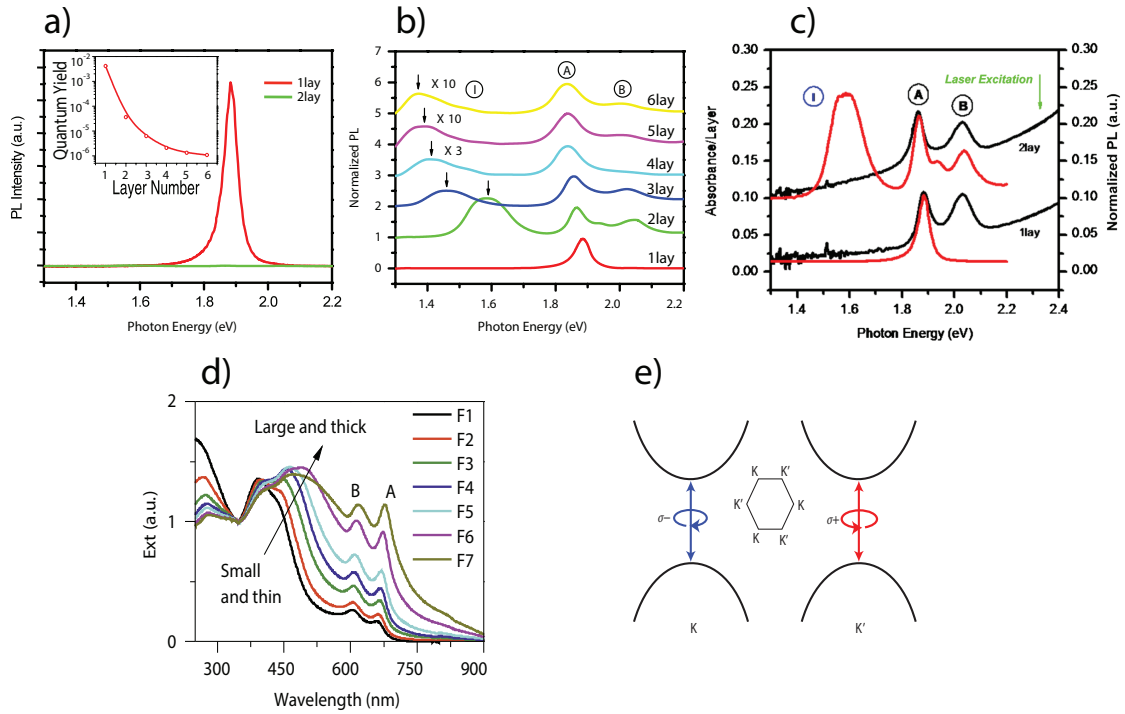


Figure 1.6: a) PL spectra for mono- and bilayer MoS_2. Inset: PL QY of thin layers for N = 1–6. b) PL spectra normalized by the intensity of peak A, from one to six layers of MoS_2. c) Normalized absorption spectra (left axis) and the corresponding PL spectra (right axis, normalized by the intensity of the peak A). d) Extinction spectra of liquid exfoliated and thickness selected MoS_2, normalized to the local minimum at 345 nm. Adapted from [35]. e) Selection rules for interband transitions in monolayer MoS_2. a), b), c) adapted from [21], e) from [28].

The PL in multilayer MoS_2 is a phonon-assisted process and is known to have negligible quantum yield (QY)(Figure 1.6a inset). The PL spectrum of a monolayer consists of a single feature centered at 1.9 eV, while few-layer samples show multiple emission peaks, namely A, B, I, as shown in Figure 1.6b. Peak A coincides with the monolayer emission peak and shifts to the red with increasing the number of layers (N). The B peak was found blue-shifted by 150 meV with respect to the A peak, while the I peak shifts with increasing N approaching the bulk indirect-gap of 1.29 eV. The PL spectra reflect the evolution of the electronic band structure reported by A. Splendiani et al. [22] with a QY

of the monolayer relatively higher (4×10^{-3}, which indicates a direct electronic transistion and a radiative efficency much higher than in bulk [21]). The absorption spectrum of bulk MoS_2 is characterized by two prominent excitonic resonant transitions A and B (see Figure 1.6c). The splitting of the VB of the monolayer at the K point is correlated to the spin orbit effect and the lack of inversion symmetry. The same splitting for the bilayer is due to the combination of the interlayer interaction and the spin orbit effect. Calculations reported by T. Cheiwchanchamnangij *et al.* [49] estimated VB splittings of 146 meV in the monolayer and 174 meV in the bilayer, which are in agreement with the energy difference between the A and B exciton peaks in the absorption spectrum reported by K. F. Mak *et al.* [21]. The position of the exciton resonances was found to be slightly blue shifted with decreasing of N. Analogously, also the A exciton absorption peak shifts progressively to higher energies for thinner samples, as shown recently by C. Backes *et al.* [35] (Figure 1.6d). It is worth noting that this confirms the theoretical calculation presented in Section 1.3.2 [49], thus with decreasing the number of the layers, the exciton binding energy increases but also the quasiparticle gap increases giving rise to a combined effect that shifts the exciton resonance to the blue. We need to stress the fact that PL emission from ultrathin TMDCs can be influenced by several factors such as the underlying substrate [68], the adsorption of molecular species from the environment (*e. g.* O_2 and H_2O) [69], the bonding of oxygen to the material's intrinsic defects (*e. g.* sulphurization vacancies) [70], the crystalline phase [42] and also by the doping in the material [71].

In addition, monolayer 2D crystals have been proposed as a suitable material for valleytronics by manipulating the valley index through an electric or magnetic field and by optical pumping [68], [72], [73], [74]. In monolayer MoS_2 at the K and K′ valleys in momentum space, the VB splitting is ~ 160 meV and the spin is well defined. The two degenerate bands (at K and K′) are of spin down $E_{\downarrow}(k)$ and spin up $E_{\uparrow}(k)$ in character implying that the valley and spin of the valence bands are coupled. This sets valley-dependent selection rules for interband transitions, so that valley polarization can be easily achieved through optical pumping by circularly polarized light and detected using circularly-polarized PL spectroscopy [68], [75]. Left and right circularly polarized light selectively excites the K and K′ valleys, respectively (Figure 1.6e). Moreover the presence of valleys and VB spin-splitting in the electronic structure of monolayer MoS_2 and other 2D TMDCs, gives rise to a series of novel opportunities in optoelectronics. For example, these materials can emit light with selective dichroism [76] and could therefore serve as switchable chiral-light sources, as a consequence of valley polarizations [77].

1.4.1 Electrical tuning of the optical properties

The basic excitonic properties of a three-dimensional (3D) bulk semiconductor differ fundamentally from those of a 2D monolayer of the same material. Generally in a common 3D system (*e. g.* GaAs) the formed excitons are weakly bound (binding energy less than 10 meV) [78] and visible only at low temperature. To observe excitonic effects at room temperature and employ them for optoelectronics applications requires engineered quantum confinement structures such as quantum wells [79]. In contrast the electron and hole forming an exciton (at room temperature) in monolayer TMDCs are strongly confined to the plane of the monolayer and additionally a reduced Coulomb screening due to the change in the dielectric environment leads to an exciton binding energy $\gtrsim 0.5$ eV [49], [80], [81] (for few layers it is ~ 100 meV for the A exciton [82]). Compared to the bulk, for the monolayer both the quasiparticle band gap and the exciton binding energy are expected to increase. Moreover, in the 2D limit the dielectric screening is also reduced because the electric field lines joining the electron and hole begin to extend outside of the sample as shown in Figure 1.7a. A close view of the excitonic transitions has been reported recently

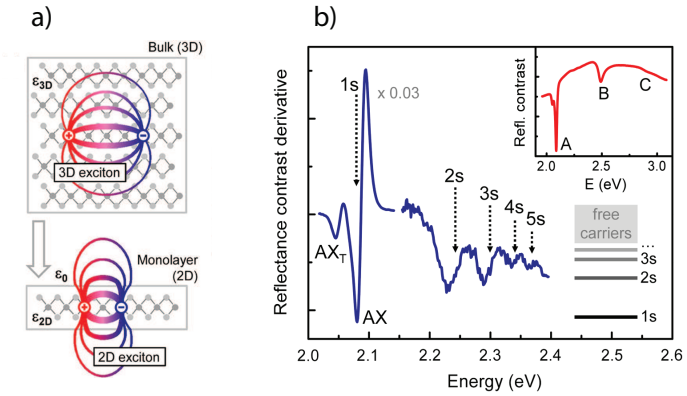


Figure 1.7: a) Representation of electrons and holes bound into excitons for the 3D bulk and a quasi-two-dimensional monolayer. The dielectric environment is indicated by different dielectric constants ε_{3D} and ε_{2D} and by the vacuum permittivity ε_0. b) The derivative of the reflectance contrast spectrum of the WS_2 monolayer. The exciton ground state and the higher excited states are indicated by their equivalent quantum numbers n. The spectral region around the 1s shows the transition (AX) and the trion peak (AXT) of the A exciton. The inset shows the reflectance contrast and the A, B and C transitions, respectively. Adapted from [83].

by A. Chernikov *et al.* [83] and by H. M. Hill *et al.* [84] giving comprehensive studies of the exciton states in WS_2 and MoS_2 monolayer.

Figure 1.7b shows the excitonic Rydberg series for a single layer WS_2 performing reflectance contrast measurements at 5 K. Figure A shows the energy separation of these resonances corresponds to a hydrogenic progression for Wannier-like excitons for a WS_2 monolayer. This model predicts exciton transition energies of $E_g - E_b^{(n)}$, where E_g is the quasiparticle gap and

$$E_b^{(n)} = \frac{\mu e^4}{2\hbar^2 \epsilon^2 (n - 1/2)^2} \tag{1.1}$$

is the binding energy of the nth excitonic state [83]. By fitting the excitonic peaks to a hydrogenic Rydberg series in a 2D system they estimated a quasiparticle gap of ~ 2.41 eV and a binding energy for the ground state exciton (1s) of ~ 0.32 eV. However the energies of the excited excitonic states 1s and 2s deviate strongly from a simple 2D hydrogenic model due to the nonuniform dielectric environment, leading the author to use a non-hydrogenic model to fit also the two lower exciton states. This is due to the fact that the electric field between the electron and hole is not confined in the plane of the material but also extends into the surrounding medium, hence the effective screening of the Coulomb interaction depends on the separation between the charges [83]. A similar experiment, carried out on MoS_2, shows the Rydberg series of the B exciton (Figure B). In this case the presented theoretical analysis yields a band gap of 2.47 eV, implying that the binding energy of the B exciton in MoS_2 is 0.44 eV. It is worth to know that the author of this paper interpreted the peak position as a signature of the B exciton and assumed that the A and B excitons have similar properties [84].

The enhanced Coulomb interaction between the charge carriers due to the quantum confinement and the reduced dielectric screening leads to several phenomena which are called many-body effects. Among them strongly bound excitons, charged excitons (trions) [85] and excitonic molecules [86] are significant both for the fundamental understanding of the materials and for their use in device applications. The ability to tune excitonic states

using external control has been reported in the MoS_2 [85] and the WS_2 monolayer [87], respectively, by K.F. Mak *et.al* and A. Chernikov *et al.* These studies are relevant for a better understanding of our experiments (discussed in Chapters 3 and 4).

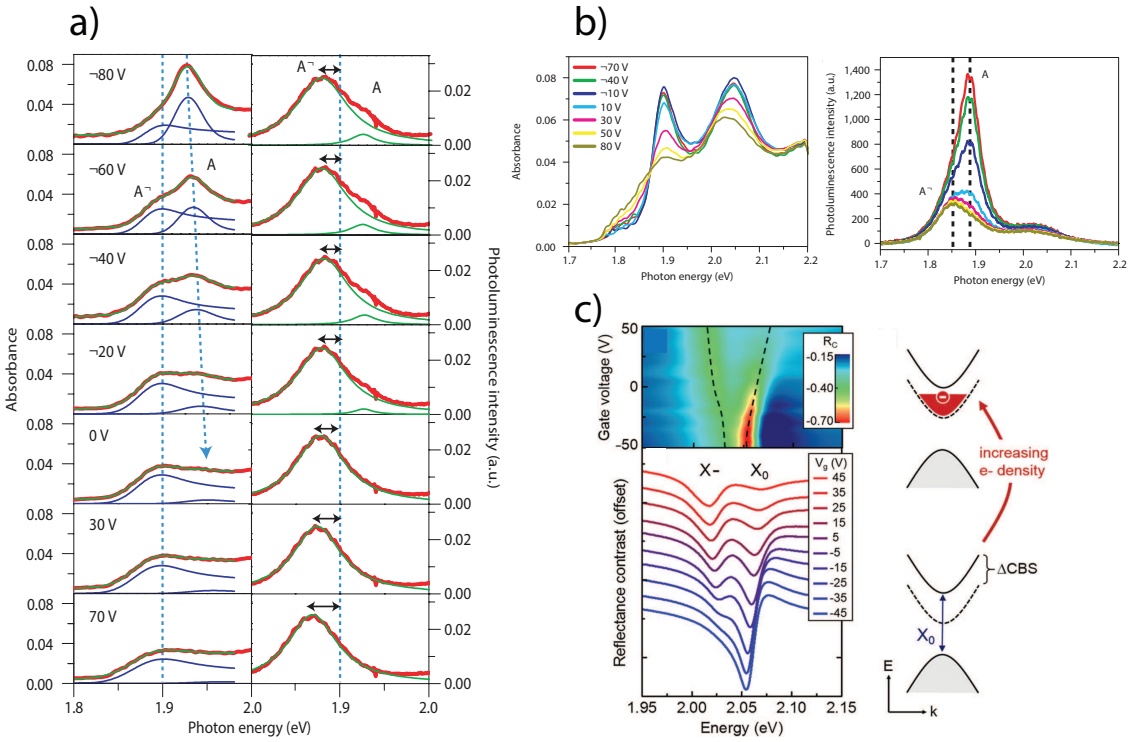


Figure 1.8: a) Absorption and PL spectra (red lines) for different back-gate voltages. The exciton (A) and trion (A^-) peaks behave differently with gate voltage. Absorption spectra with the dashed blue lines that show the peak energies of A and A^- features (left). The PL spectra of the A and A^- features (right) are fitted by Lorentzian functions (green lines). The dashed blue line indicates the absorption peak of the (A^-) resonance and the arrows show the doping-dependent shift of the trion PL. b) Absorption and photoluminescence spectra at different back-gate voltages, room temperature measurements. c) Density plot of the reflectance contrast spectra of WS_2 for different gate voltages at a temperature of $T = 50$ K (top panel). The dotted lines indicate the evolution of the charged and neutral exciton peaks. Reflectance contrast spectra for selected gate voltages (bottom panel). Schematic illustration of the WS_2 band structure at the band edge transition, with and without electron doping. a,b) adapted from [85], c) adapted from [87].

They investigated the optical response of MoS_2 FET under gate voltages from -100 to 80 V, corresponding to approximate charge neutrality to a doping density of $\sim 10^{13}$ cm^{-2}. By increasing the electron density they observed a reduction of the optical absorbance in correspondence of the A transition and the emergence of a lower energy resonance marked as A^- (Figure 1.8a,b). This feature was identified as a bound state of an exciton to a charge (electron or hole (A^+)), the so-called trion. In contrast to the neutral exciton that for $V_g > 0$ disappears in the background, A^- broadens and approximately maintains its spectral weight [68]. The same consideration was made for the photoluminescence. The PL intensity of the A exciton, like its absorbance, can be switched off by doping and this is visible at low temperature as well as at room temperature, as shown in Figure 1.8a,b. The trion feature emerges with increasing of the doping and with the reduction of the neutral

exciton absorption and photoluminescence. The reason for that was mainly ascribed to a combined effect of Pauli blocking and many-body interactions. From the linear fit of the splitting A-A^- as a function of the gate voltage they calculated, for the undoped sample, a trion binding energy of 18 meV at 10 K and 30 meV at room temperature [85].

This research work was corroborated by a successive study on the WS_2 monolayer. Figure 1.8c shows the shift of the resonance transitions of single layer WS_2, indicated as X^0 (neutral exciton) and X^- (trion), as a function of the gate-induced doping. The author found exciton transitions that shift due to the combined effect from the reduced binding energies and band gap renormalization. It is worth to know that the conduction band in WS_2 band has a finite spin splitting of about 30–40 meV (ΔCBS). Therefore for the highest doping density used in this experiment 8×10^{12} cm^{-2} more than 75% of the electrons reside in the lower conduction band. This enables WS_2 as a suitable 2D material to separate the screening phenomena from the Pauli-blocking effects and for device application. The screening of the attractive interaction, due to the free charge, gives rise to a reduced exciton oscillator strength and binding energy. The reduction of the repulsive interaction induces a decrease of the quasiparticle energy and thus leads to the renormalization of the band gap to lower energies. So then in the doping region the band gap shifts to lower energies and the exciton peaks broaden and decrease in oscillator strength. As a result for the lowest quantum number ($n = 1, 2$) the blue shift of the excitonic states corresponds to the reduction of the exciton binding energy with increased gate voltage, while for the $n = 3$ transition shifts to lower energies following the trend of the quasiparticle gap [87]. Overall the relative shift between trion and neutral exciton is almost linear with the doping.

1.5 Time-Resolved Optical Response

In this section I will introduce the interesting studies of ultrafast spectroscopy as well as of dynamics of the excited states, useful for the interpretation of our results (discussed in Chapters 3 and 5). The optical behaviour of the material under pulsed laser excitation was found significantly correlated to the photogenerated excitons density and to the many-body effects during the relaxation process as well. This leads to strong implications for employing TMDCs in optoelectronic and photonic devices.

We need to consider the definition of time-resolved spectroscopy for better understanding the experiments presented in this section. Time-resolved experiments explore the temporal evolution of the spectra (transmission, absorption or reflectance) after photoexcitation. The first laser pulse (pump) excites the material inducing a change of the optical response, the second pulse (probe, temporally delayed) senses either transmission or absorption change induced by pump pulse. Hence, it is possible to monitor the time evolution of the spectra by scanning the pump-probe delay, either wavelength by wavelength or by using a broadband white-light continuum pulses. In the text we will often report the terms photobleaching (PB) and photoinduced absorption (PA). For measurements in transmission geometry, PB indicates an increase of the transmission (positive signal) and PA indicates a decrease of the transmission (negative signal). Overall, these concepts will be explained in chapter 2 (Section 2.2).

A large number of often controversial interpretions of the femtosecond behaviour of TMDCs were proposed, ranging from carrier-induced broadening [88] to exciton-biexciton transitions [89] and band-gap renormalization (BGR) [90]. One of the first research works on femtosecond electron relaxation in TMDCs was done by H. Shi *et al.* [91] and represents a comprehensive analysis of the ultrafast response of MoS_2 few and mono-layers within 500 fs time resolution and the multiexponential nature of the relaxation process. Figure 1.9a

shows the photoinduced bleaching (PB, positive signal) near the A exciton resonance that they ascribe to a band filling effect. Photoinduced absorption (PA, negative signal) was also observed symmetrically situated on both sides of the PB bands and assigned to a carrier-induced mechanism. They compare exciton dynamics in the sample with a different thickness showing a fast interband relaxation of the photoexcited exciton from the created C exciton level to the A exciton band. The transient absorption of mono and few layers revealed a rapid interband relaxation time of less than 500 fs, while for the thick crystal a much slower interband relaxation was observed. In the bulk sample they assigned the fast rise time constant of 2 ps to carrier-carrier scattering and the slower rise time constant to the carrrier-phonon scattering process followed by a single exponential decay of 2.6 ns probably due to an inter-valley scattering process between the A exciton and the indirect gap. To explain the enhancement of the interband relaxation observed in the monolayer, they tentatively identified surface traps or interfacial defects as an additional cooling channel for the relaxation of the high energy carriers. The intermediate decay time constant for few- and monolayer was found similar to the interband carrier-phonon scattering time observed in photoluminescence lifetime measurements and depending on temperature. Finally, they tentatively assigned the slowest decay component to a direct interband electron-hole recombination.

Similar kind of work in a low fluence regime ($\sim 1\ \mu J/\mathrm{cm}^2$) was done by Q. Cui *et al.* [92] on monolayer WSe_2. By comparing the PL line shape with the transient transmission spectra in the spectral window of the A exciton of a monolayer and bulk WSe_2 they observed a similarity of the PL peak with the transient transmission spectra at 5 ps. In this report the transient spectra were measured tuning the probe, wavelength by wavelength, covering the range of the A exciton and the explanation of the spectral shape and its origin has not been properly considered. However, by varying the distance between pump and probe they recorded a spatiotemporally-resolved measurement and successively estimated a diffusion coefficient of $\sim 15\ \mathrm{cm}^2/\mathrm{s}$ and a diffusion length of the excitons of 160 nm for WSe_2 monolayer.

For the high carrier density regime (10^{13}–$10^{14}\ \mathrm{cm}^{-2}$) Z. Nie *et al.* [93] reported an ultrafast dynamics dominated by free carriers rather than excitons. By probing the dynamics with ultrashort pulses of ~ 10 fs they observed a thermalization that occurs in less than 20 fs mediated via both carrier-carrier and carrier-phonon scattering, and a 600 fs decay component indicating carrier cooling via phonon emission. This estimated lifetime increases with higher fluence and temperature, thus resulting in the hot phonon effect: the majority of phonons have a slow relaxation rate (> 10 ps), which impedes cooling via phonon emission.

The ultrafast optical response of TMDCs is strongly affected by the excitation density. Among the many body-effects, exciton-exciton annihilation is important because such non-radiative recombination channels limit the intrinsic exciton lifetime and frequently influence the efficiency of semiconductor lasers and light-emitting diodes. In this process one exciton is destroyed and its energy is transferred to another exciton. The dynamics of excitons can be efficiently modeled by a decay channel that varies quadratically with exciton density. A recent report by D. Sun *et al.* [94] revealed a decay of the A exciton population in MoS_2 that is strongly influenced by the pump fluence (or injected exciton density). The intensity of the pump probe signal was found to be in the linear regime in the range of fluence 8–46 $\mu\mathrm{J}/\mathrm{cm}^2$ that corresponds to an injected exciton density between 0.5–2.5 $10^{12}\ \mathrm{cm}^{-2}$. From the rate equation they estimated an annihilation rate of $\sim 4 \times 10^2\ \mathrm{cm}^2/\mathrm{s}$ and a lifetime for the A exciton of 11 ps at an exciton density of $10^{12}\ \mathrm{cm}^{-2}$. Similar analysis was carried out on a single layer of $MoSe_2$ by N. Kumar *et al.* [95] that revealed a linear regime up to $5 \times 10^{11}\ \mathrm{cm}^{-2}$ and an annihilation rate of $\sim 0.33\ \mathrm{cm}^2/s$.

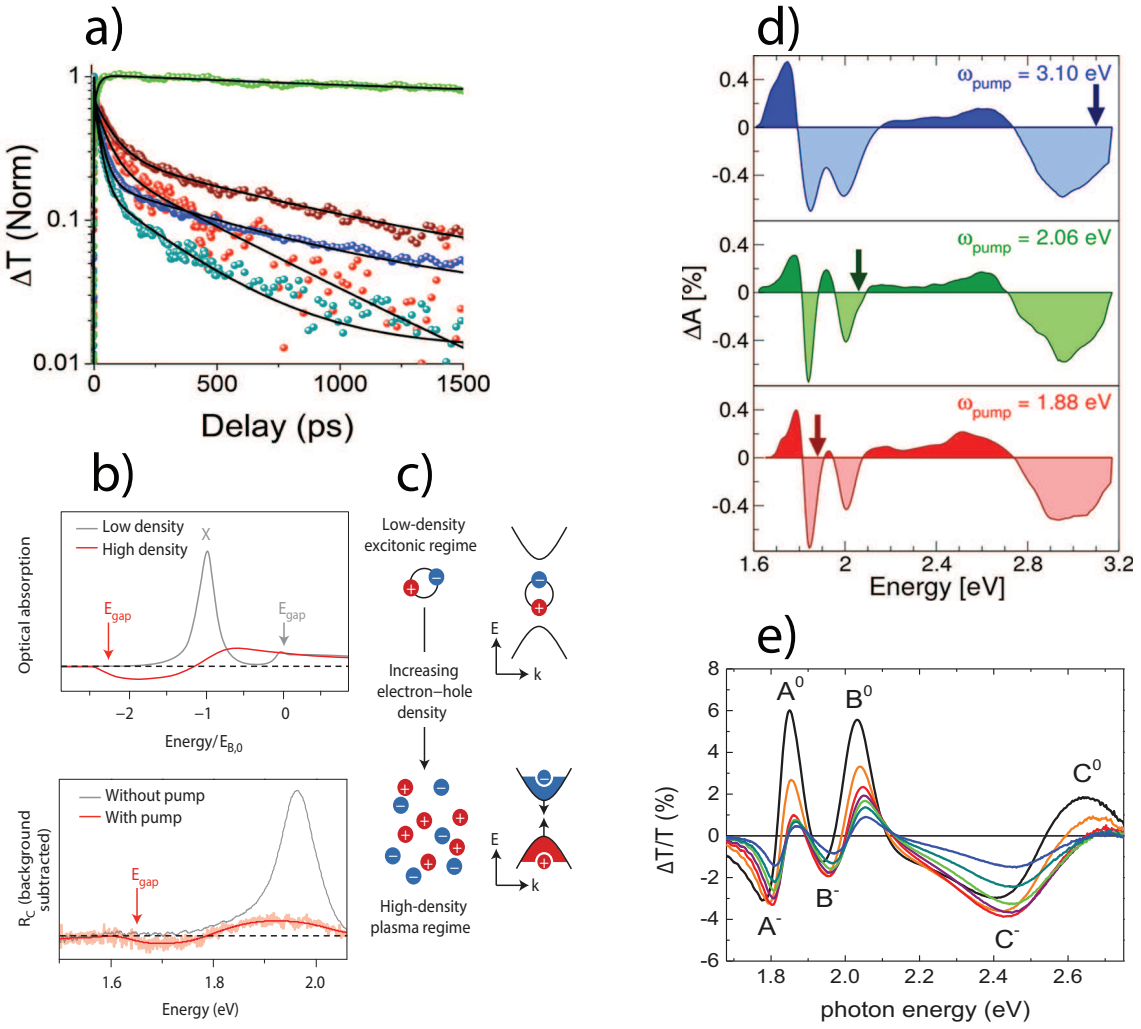


Figure 1.9: a) Transient absorption dynamics with pump wavelength of 387 nm and a probe wavelength of 670 nm. The color legend indicates different positions on the sample, which is made of a multi- and monolayer region: monolayer (brown and red) few layers (blue and dark cyan), bulk (green). Exciton dynamics in the bulk is probed at 690 nm. The solid lines are fits of a triexponential decay function convoluted with a Gaussian response function. Adapted from [91]. b) Schematic representation of the optical absorption of a two-dimensional semiconductor for regimes of low and high carrier density (top panel). WS_2 bilayer data for strong optical excitation (bottom panel). c) Sketch of the transition from the low-density excitonic regime to a dense electron-hole plasma. d) Transient absorption spectra of MoS_2 monolayer, recorded at fixed pump-probe delay $\tau = 300$ fs, for three pump photon energies. Adapted from [90]. e) Pump-probe spectra of multilayer MoS_2 at delays: 300 fs (black), 1 ps (orange), 3 ps (red), 10 ps (purple), 30 ps (green), 100 ps (dark cyan), and 300 ps (blue). Adapted from [96]. b) and c) adapted from [97].

The renormalization of the quasiparticle bandgap in TMDCs was theoretically predicted by A. Steinhoff *et al.* on MoS_2 monolayer [98] and experimentally proved for the first time by A. Chernikov *et al.* [97] on mono- and bilayer of WS_2. This research work shows the response of WS_2 after a strong photoexcitation on the femtosecond timescale. By pumping in resonance with the B exciton (2.4 eV) with a fluence of 840 μ/cm^2 or an

effective density of excitons approaching 1×10^{14} cm^{-2}, they revealed a drastic change in the optical response of the material. Figure 1.9b (bottom panel) shows the exciton resonance A (black curve) that disappears when a pump pulse is sent to the sample. Together with the drop of the signal a negative spectral feature appears at low energy, around 1.6 eV. To explain the scenario the authors consider the Coulomb interaction to be strongly screened due to the high density regime. This reduces the exciton binding energy to zero, that means the semiconductor undergoes a Mott transition from the insulating excitonic regime to a dense electron-hole plasma (Figure 1.9c). Therefore, the exciton is no longer a spectral signature of the optical response. On the other hand the reduction of the repulsive Coulomb interaction results in a decrease of the quasi particle gap. This produces a bandgap renormalization shifting it below the energy of the initial exciton peak. Moreover, filling the CB and VB states with electrons and holes leads to the Pauli blocking on the exciton resonance and to inversion of the carrier population near the band edge. This is shown in the spectral region as a negative optical absorption, starting at the renormalized bandgap energy and extending to a point where the absorption crosses zero. They estimated a renormalization of 500 meV in the bilayer and showed an optical response that fully returns to the initial condition after $\sim$ 250 fs. A similar effect was reported in the same paper for the monolayer at 70 K and at room temperature upon increasing the pump fluence at 3400 μJ/cm^2. In the monolayer the inversion spectral feature is present at lower energies and it has a broader spectral width compared to the bilayer.

Bandgap renormalization (BGR) was also discussed by E. A. A. Pogna *et al.* [90] on a single layer MoS_2 in a relatively low carrier density regime of $\sim 3 \times 10^{12}$ cm^{-2}. Figure 1.9d shows the measured transient absorption spectra for three different photon energies. Despite the different excitation conditions, the spectra reveal a remarkable similarity with a negative photobleaching (A, B and C exciton resonances) and a positive photoinduced absorption. Time domain *ab initio* simulations where also compared with the experimental data showing that the model does not reproduce the experiments. Therefore they deduced that the Pauli blocking alone cannot be used to explain the simultaneous rise of the photobleaching features. By introducing to the model screening of the Coulomb interaction and a charge density variation they found out a better agreement with the experimental data. Electronic screening leads to a simultaneous renormalization of both exciton binding energy and bandgap (BGR), that means two opposite effects that partially compensate each other: a red-shift of the optical spectra due to electronic gap shrinkage, and a blue-shift arising from binding energy reduction. Since the compensation is only partial, it gives rise to an overall peak shift of a few tens of meV. This shift appears as a first derivative line shape in the pump-probe spectrum.

Although BGR was used to explain the early stage of the optical response after photoexcitation, the model was not implemented to explain the evolution of the transient spectra during the relaxation process. In our research group this significant aspect has been taken into consideration even before the recent BGR theory. The measurements were carried out on multilayer MoS_2 obtained from liquid exfoliation since this processing enables an easier preparation of the samples on a transparent substrate by directly coating it with exfoliated material solutions in water and surfactants [99] or blend TMDCs with an organic polymer. The research work published by T. Borzda *et al.* [96] reveals the primary role of the exciton dissociation and charge formation during the first few ps of the relaxation process. They observed a photoinduced absorption feature red-shifted with respect to the A exciton energy that grows during the first few ps of the dynamics. This effect is accompanied with a reduction of the photobleaching spectral features. Overall the resulting spectrum is the overlap of the positive and negative peaks which change shape during the time evolution (Figure 1.9e). A derivative line shape induced by BGR could

not explain alone a non-uniform change in the spectral shape. They identified the negative spectral signature as a photoinduced absorption of the charges that grow together with the reduction of the bleaching peak, during the relaxation process from higher excited state (C exciton) to lower (A exciton band). To untangle the two close spectral signatures (exciton and charge) they modeled the evolution of the transient transmission spectrum by considering excitons as a primary photoexcited species, and these excitons dissociate into pairs of charges with the characteristic time τ_1. The two kinetic equations used in a cascade model take into account the dissociation of excitons into charges, that happens within 700 fs, and the relaxation of the charge through most probably non-radiative channels on a few hundred ps time scale. The estimated 100% dissociation yield was ascribed to the surplus energy of the created hot exciton, which increases their probability of dissociation during the relaxation process. In addition, defects, such as surface defects, flake edges, metallic inclusions, and crystal faults, can facilitate the dissociation. A similar study was done by V. Vega-Mayoral *et al.* [100] on a multilayer WS_2 that modified the simple model, efficiently used for MoS_2, by adding an intermediate kinetic equation to the cascade model. Like in the case of the work done by T. Borzda *et al.* the charges originate from the exciton dissociation and the intermediate state was associated with a diffusion of the charges that get trapped in defects and successively recombine in a non-exponential mode. We estimated a first characteristic life time of 1.3 ps and the second lifetime of 5.5 ps, that is the time for a charge to escape its counter-charge or the time to meet a trap.

1.6 Device Applications

The technological interest in 2D TMDCs and their rapid evolution in nanotechnology was initiated in 2011 by B. Radisavljevic *et al.* [18] who demonstrated the first single-layer MoS_2 double gate transistor with promising performance. In the nanodevices field thin layers of MoS_2 are the best studied among the two-dimensional TMDCs. Their atomic-scale thickness and the presence of a semiconducting energy bandgap enable these materials for applications where an ideal electrostatic control and low standby power dissipation are required. Moreover, due to the presence of a bandgap, these materials are suitable for optoelectronics devices, such as solar cells and photodetectors. In the last few years a lot of proof-of-principle devices were reported showing an improvement of the actual technology as well as enabling new concepts in device physics and fabrication. In this section I will introduce more significant research works mainly based on single layer MoS_2 that was carried out in A. Kis group, where I have also spent a part of my research work to develop transparent field effect transistors.

1.6.1 Field effect transistors

The FET is a three-electrodes device where the electric current flowing between a pair of electrodes (source and drain) is modulated by the voltage applied onto the gate electrode. The current I_{ds} flows through a semiconducting material (channel), which is separated from the gate electrode by a thin insulating layer of dielectric (illustrated in Figure 1.10a). In n-type devices, for gate voltages V_g smaller than the threshold voltage V_{th}, the channel should behave as an open circuit, with negligible off-current I_{off}. On the other hand, for $V_g > V_{th}$ the channel becomes conducting and a high current I_{on} flows. In order to use these kinds of devices as a switch in digital electronics, a large ratio from 10^4 to 10^7 between the on-state and off-state current is required [101].

Figure 1.10b shows the evolution during the last four decades of the size of MOSFET device gate length and the corresponding change in the number of transistors per processor

chip [1]. The exponential increase of the transistor per processor chip follows the law described in 1965 by Gordon Moore, who predicted that the density of transistors should double every 18 months. However, scaling theories affirm that Moore's law is approaching its limit, due to the quantum effect, as the transistor dimensions get close to the interatomic distance. In fact the performance of the transistors is strongly correlated with the length of the channel (L) because it corresponds to the path that the charge carriers have to travel to carry information. Improving the FET speed means reducing their dimensions. Nevertheless, if the channel length L is reduced and comparable with the thickness of the semiconducting channel, a number of phenomena occur, so called short channel effects (SCEs) which are detrimental for the correct operation of the devices.

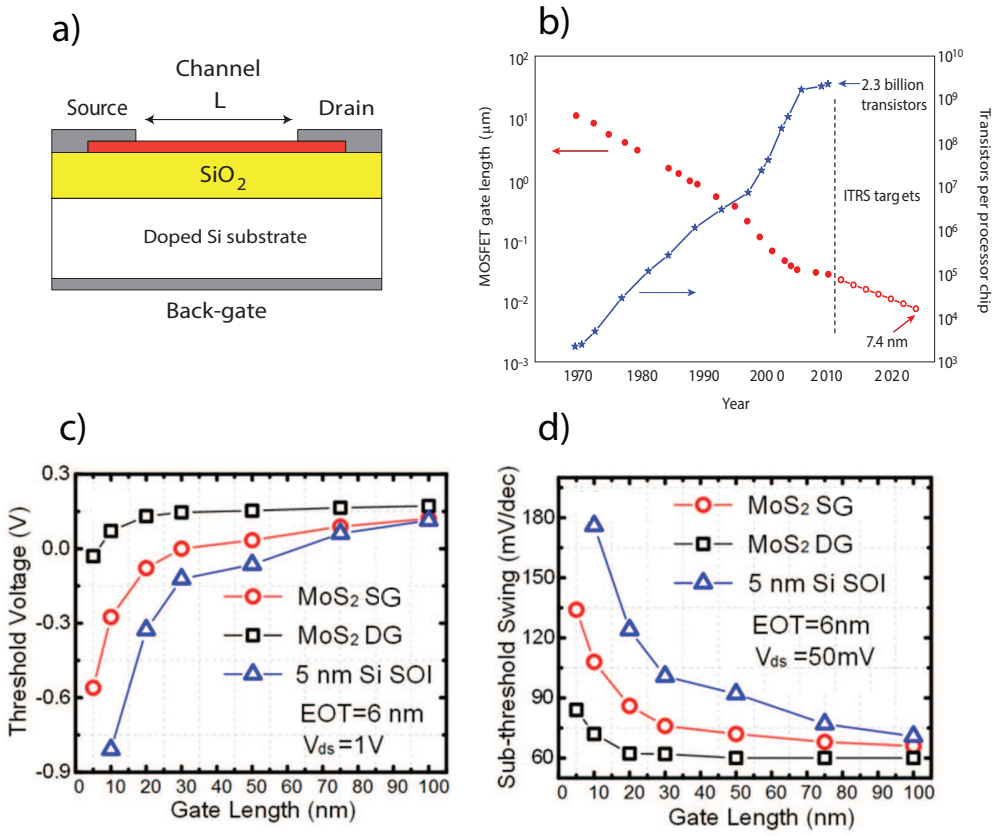


Figure 1.10: a) Schematic geometry and electrical connections of a back-gated FET. b) Evolution of gate length L and the number of transistors per processor chip. Adapted from [1]. c) Calculated dependence of the threshold voltage on the gate length L. d) Calculated SS (subthreshold swing) degradation with gate-length scaling. c) and d) adapted from [102].

An electrostatic model based on Poisson's equation can be used to evaluate SCEs that are induced by the penetration of the drain-electrode field (in-plane direction) into the transistor channel [103]. Overall we can define a quantity called natural length λ, which gives the position of the maximum of the electrostatic potential inside the channel, expressed as:

$$\lambda = \sqrt{\frac{\varepsilon_{\mathrm{ch}}}{N \cdot \varepsilon_i} \cdot t_{\mathrm{ch}} \cdot t_i}, \tag{1.2}$$

where t_{ch} (t_i) and $\varepsilon_{\mathrm{ch}}$ (ε_i) are the thickness and the dielectric constant of the channel material (dielectric insulator), respectively. N is the effective gate number and depends on

the architecture of the device. FETs can be considered immune from SCEs when $L \gtrsim 6\lambda$. Minimizing λ it is possible to make transistors robust against SCEs. Possible strategies for that are increasing the gate capacitance by using a gate oxide with high dielectric constant and small thickness, increasing the number of the gates in the architecture and a vertical scaling of the channel materials. However N and t_i can increase the fabrication cost and the risk of leakage currents. Therefore the thickness of the channel represents a reasonable option.

It is worth describing SCEs that can occur in the operating FET. Scaling the channel length the two main effects are the voltage roll-off and the degradation of the subthreshold characteristics that is estimated as the reciprocal of the subthreshold slope. The first case is the shift of the threshold voltage: V_{th} can significantly shift from the long-channel value to the point that a non-negligible current may flow in the device also when no gate voltage is applied. In the second case, the subthreshold swing (SS), which indicates how sharply the subthreshold current changes with increasing the gate voltage, can increase over the lowest ideal value of 60 mV/dec degrading the switching behavior of the FET. Figure 1.10c,d shows simulations based on the non-equilibrium Green's function (NEGF) formalism carried out by W. Cao *et al.* [102]. The two parameters V_{th} and SS are displayed as a function of the channel length for MoS_2 FETs with a single and double gate architecture and for 5 nm Si on SiO_2. For a Si FET the deviation of both parameters becomes evident when L is reduced below 40 nm. On the contrary, MoS_2 FETs show a much better behaviour. As predicted from Equation 1.2 the combined use of the double gate produces the best results with a V_{th} still positive for $L \sim 10$ nm and SS value approaching ~ 70 mV/dec. This confirms the opportunity, in the future, to overcome the limits of the silicon technology by using semiconducting layered materials.

1.6.2 Single layer MoS_2 transistors

The first FET based on TMDCs was reported in 2004 by V. Podzorov *et al.* [104], who shows a WSe_2 crystal liquid gate FET with a mobility comparable of 500 $cm^2\ V^{-1}\ s^{-1}$, ambipolar behaviour and a 10^4 $I_{\mathrm{on}}/I_{\mathrm{off}}$ ratio at 60 K. After this research work a comprehensive investigation on several TMDCs was carried out by K. S. Novoselov *et al.* [3], however the back-gate FETs based on single layer $NbSe_2$ and MoS_2 show a mobility ranked between 0.5 and 2 $cm^2\ V^{-1}\ s^{-1}$.

The implementation of a single layer MoS_2 with dual gate geometry was first reported by B. Radisavljevic *et al.*, who revealed better electrical transport parameters and a real prospective of a new technology [18]. A schematic illustration of the transistor is given in Figure 1.11a. MoS_2 layers were first isolated by scotch-tape-based exfoliation onto a doped silicon substrate, covered with 270 nm thick SiO_2. After the deposition of 50 nm thick gold electrodes, the device was annealed at 200 °C to remove resist residue and decrease the contact resistance. To avoid the effect of the Coulomb scattering, which in 2D TMDCs is caused by random charged impurities located within the 2D TMDCs or in their surface, gate dielectric materials with a high dielectric constant were applied. Therefore, in order to screen the Coulomb scattering they used 30 nm of HfO_2 with dielectric costant of 19 and bandgap of 5.7 eV. The HfO_2 film was further capped with a metal layer (Cr/Au) that functioned as a top-gate electrode. Figure 1.11b shows a set of current-voltage transfer characteristics (I_{ds} *vs.* V_{tg}) acquired from such a device for different drain-source voltage biases V_{ds}. For these measurements the back-gate electrode V_{bg} was grounded, whereas a top-gate voltage V_{tg} was applied and swept in the range of ± 4 V. From the curve at $V_{\mathrm{ds}} =$ 500 mV it was possible to extract $I_{\mathrm{on}}/I_{\mathrm{off}} \sim 10^8$, with $I_{\mathrm{off}} \sim 100$ fA and $I_{\mathrm{on}} \sim 10$ μA. The highest transconductance ($g_{\mathrm{m}} = \frac{\partial I_{\mathrm{ds}}}{\partial V_{\mathrm{tg}}}$) was $\sim 4\mu$S (1μS/μm) and the subthreshold swing was found to be ~ 74 mV/dec. Values of mobility for this device, which were found to be

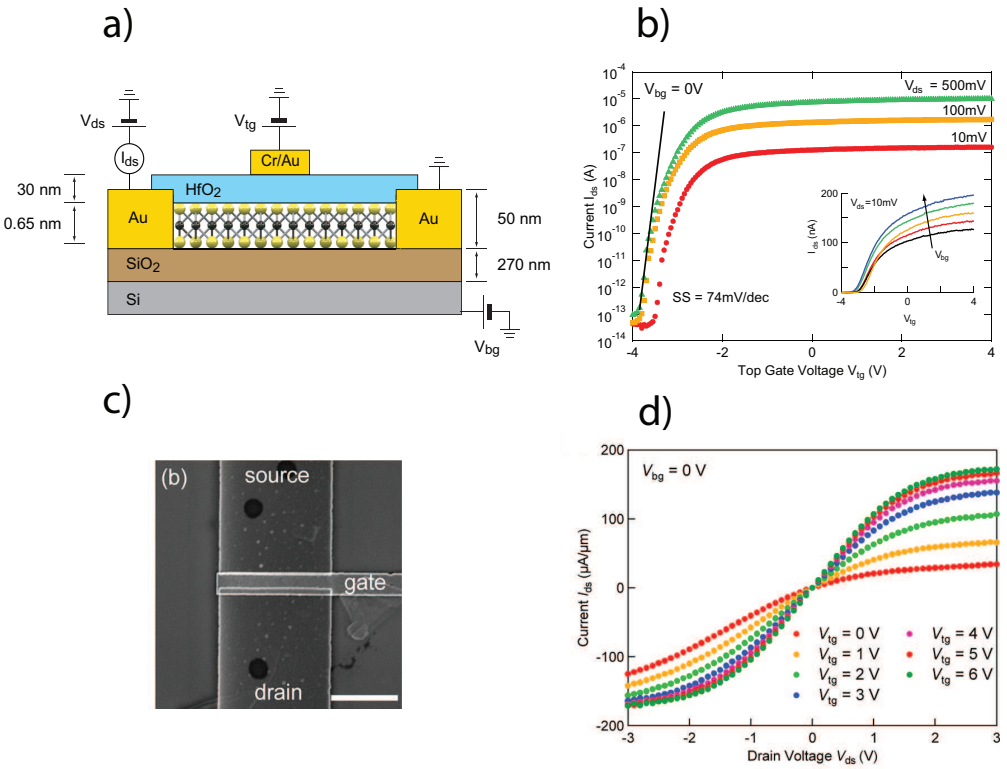


Figure 1.11: a) Cross-sectional view of a dual-gated transistor based on single-layer MoS_2. b) Transfer characteristic: drain-source current I_{ds} as a function of top-gate voltage V_{tg} for different bias voltages V_{ds}. Inset: I_{ds} *vs.* V_{tg} for different values of back-gate voltage V_{bg}. c) Scanning electron microscopy (SEM) image of a single-layer MoS_2 FET with top-gate electrode covering the entire channel area. d) Output characteristics (I_{ds} *vs.* V_{ds}) showing current saturation at large V_{ds}. a) and b) adapted from [18], c) and d) adapted from [5].

around 200 $cm^2\ V^{-1}\ s^{-1}$, are not comparable with the highest values of mobility found for graphene at room temperature, exceeding 15 $\times$ 10^4 $cm^2\ V^{-1}\ s^{-1}$ [105]. It is worth noting that the first transistor suffered from high access resistance and a limited gate control due to the partial spatial overlapping of the top-gate electrode with the channel area.

The transistor performance was optimized in 2012 by D. Lembke and A. Kis [5] with full gate-channel overlap, Figure 1.11c. They show a mobility value on silicon-level $\sim$ 1090 $cm^2\ V^{-1}\ s^{-1}$, a two orders of magnitude increase in I_{on} and 30 times improvement in g_m. For the first time, the saturation behaviour of the current in the output characteristic for $V_{ds} > 1$ V (see Figure 1.11d) and the achievement of the drain-source conductance g_{ds} ($g_{ds} = \frac{\partial I_{ds}}{\partial V_{ds}}$) smaller than 2.1 $\mu S/\mu m$ was shown. In addition, MoS_2 FETs can offer a gain $G = \frac{g_m}{g_{ds}}$ larger than 10, enabling the possibility to use them in analog electronic circuits. Lembke and Kis also studied the breakdown current density in MoS_2 which is close to 5 $\times$ 10^7 A/cm^2. The maximum current density was found to be two orders of magnitude smaller than in graphene but still extremely high and 50 times larger than the limit set for metals (*e. g.* copper) by electromigration. This is due to strong intralayer Mo-S covalent bonds which are much stronger than metallic bonds. This study demonstrates that single-layer MoS_2 could be used in analogue circuit applications where it could provide power gain and support large current densities. Recently D. Krasnozhon et al. [106] demonstrated the high-frequency operation of a MoS_2 transistor. In the paper they show current, voltage, and power gains in the gigahertz range in transistors based on 1–3 layer thick MoS_2 with

a channel length of 240 nm. This shows that the mobility of MoS_2 is large enough to allow device operation in the technologically relevant gigahertz frequency range.

1.6.3 Digital electronics

After realizing a room temperature double-gate field effect transistor, B. Radisavljevic *et al.* [19] implemented a more complex digital and analog electronic device integrated on the same chip. They reported the first digital logic inverter built on monolayer MoS_2. Figure 1.12a shows the electronic architecture consisting of two FETs connected in series with the common electrode serving as the output, whereas the input signal is on the top gate of the *lower* FET. The drain contact of the *upper* FET is connected to a voltage supply of 2V (V_{DD}) while the other terminal (source) is connected to the ground. In this configuration the transistor connected to the ground acts as a switch, while the other connected with the voltage supply acts as an active load. The MoS_2 integrated circuit operates as a logic inverter converting a logical 0 (low input voltage) into logical 1 (high output voltage) and *vice versa*. For input voltages corresponding to logic 0, the switch transistor offers a high resistance and is turned off. Then the output measured will be close to the supply voltage of $V_{DD} = 2$V applied to the drain electrode. By increasing the input voltage above -1V, the lower FET becomes more conductive and the output voltage V_{out} will be in the low range. The gain G of the inverter is calculated as $G = \frac{-dV_{out}}{dV_{in}}$, from the plot in Figure 1.12b, this inverter has a voltage gain higher than 4 and, therefore, it is suitable for integration in arrays of logic gates.

It was proven that the same device could also operate as an analog small-signal amplifier [107]. They showed an amplification of the amplitude output voltage by applying an AC voltage with the amplitude of 100 mV and frequency ranking from 10 Hz and 2 kHz to the imput terminal. The gain factor G was found to be ~ 4 at low frequency (< 200 Hz) and greater than one for $f < 2$ kHz, with cut-off frequency limited by parasitic capacitance and contact resistance of the FETs.

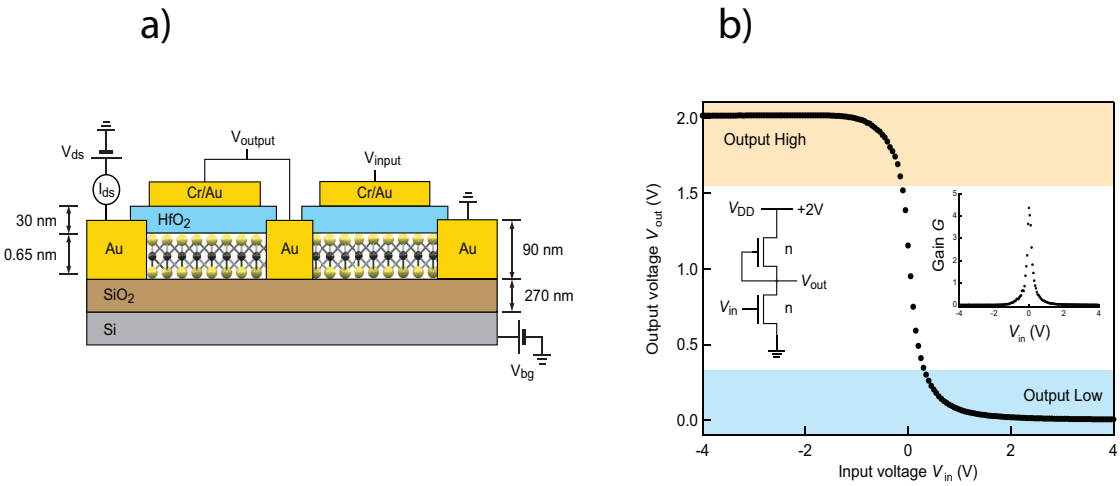


Figure 1.12: a) Cross-sectional view of the logic inverter made of two dual-gated FETs connected in series. b) $V_{out} - V_{in}$ characteristic of the fabricated inverter. Insets: circuit sketch (left) and gain G as a function of V_{in} (right). Adapted from [19].

1.6.4 Optoelectronic devices

The direct bandgap of TMDCs and its tuning with the number of the layers make them suitable for optoelectronic applications including flexible light-emitting devices or transparent ultrasensitive photodetectors. The first single layer MoS_2 phototransistor was reported in 2012 by Z. Yin *et al.* [108] and showed a photoresponsivity of 7.5 mA/W. Although this value is comparable to the one obtained with graphene devices, it is significantly lower than in the case of Si-based photodetectors (few hundred mA/W). However, the relatively low mobility (0.1 cm^2 V^{-1} s^{-1}) and high contact resistance in these devices offset the advantage of using a material with direct bandgap. In 2013, O. Lopez-Sanchez *et al.* [20] reported a record photoresponsivity of 880 A/W. The measurement was performed on a backgate monolayer MoS_2 FET, with better mobility and contact quality. By illuminating the channel with a green laser ($\lambda = 561$ nm, 2.21 eV), as shown in Figure 1.13a, the drain-source current I_{ds} was found to increase over the entire investigated gate-voltage range. This indicates a strong contribution of the photo excited carriers to the current in both off and on state. However, they did not explain the origin of the charge considering the fact that MoS_2 has a quasiparticle gap around 2.34 eV. It was also shown that, in the off-state, the dark current I_{off} can be extremely small, thanks to the sizeable energy gap that results in a low level noise in the 2D limit with respect to the bulk case. In monolayer phototransistors NEP (noise equivalent power) can be 1.5×10^{-15} $W/\sqrt{Hz}$ that is one order of magnitude better than in commercial Si avalanche photodiodes.

The possibility to generate light in TMDCs was first reported by R. S. Sundaram *et al.* [110], however they observed electrically excited luminescence from a small region of the MoS_2 channel close to the metal contact edge. They ascribed the observed electroluminescence to hot carrier processes when a high electric field is applied, that means a device with high power threshold. The solution to overcome these limiting factors was suggested by O. Lopez-Sanchez *et al.* [109] by building light-emitting diodes based on vertical p-n junction, resulting in an increase of the junction area. The p-n junction was made of a vertical heterostructure of p-doped Si and n-type MoS_2. In this device the radiative recombination process takes place at the interface Si/MoS_2 involving electrons injected into the monolayer and holes in p-type Si, Figure 1.13b. Moreover, it was also proved that the same device can generate current upon light irradiation acting as a solar cell with external quantum efficiency exceeding 4%.

Different from MoS_2, which is naturally n-doped, WSe_2 occurs in nature with low levels of doping and both electrons and holes can be injected and transported [111]. Figure 1.13c shows the ambipolar transfer characteristic of a single layer WSe_2 FET that I realized during the PhD. In this case the microfabrication of the FETs in dual gate configuration for optical experiments required more steps (presented in Chapter 2 for MoS_2 but suitable for several TMDCs), but they are simplified by using the polymer electrolyte as a top gate. In the literature many combinations of ion liquid and polymers are used to develop electric-double-layer FETs, in our case I chose a blend of 1-ethyl-3-methylimidazolium bis(trifluoromethylsulfonyl)imide (EMIM [TFSI]) as ions, and a polystyrene-poly(methyl methacrylate)-polystyrene (PS-PMMA-PS) triblock copolymer. The polymer electrolyte can be easily spin-coated in order to achieve a homogeneous surface on the sample. Recently researchers have exploited WSe_2 properties to build up light emitting diodes from lateral p-n junctions based on monolayer WSe_2, where the p and n regions were formed by a simple double back-gate control on the ambipolar 2D sheet [11]. Moreover, the presence of valley degrees of freedom could enable a new generation of optoelectronic devices. For instance, recently Y. J. Zhang *et al.* [77] demonstrated the implementation of a novel chiral light source that exploits to advantage the valley degrees of freedom in ambipolar WSe_2.

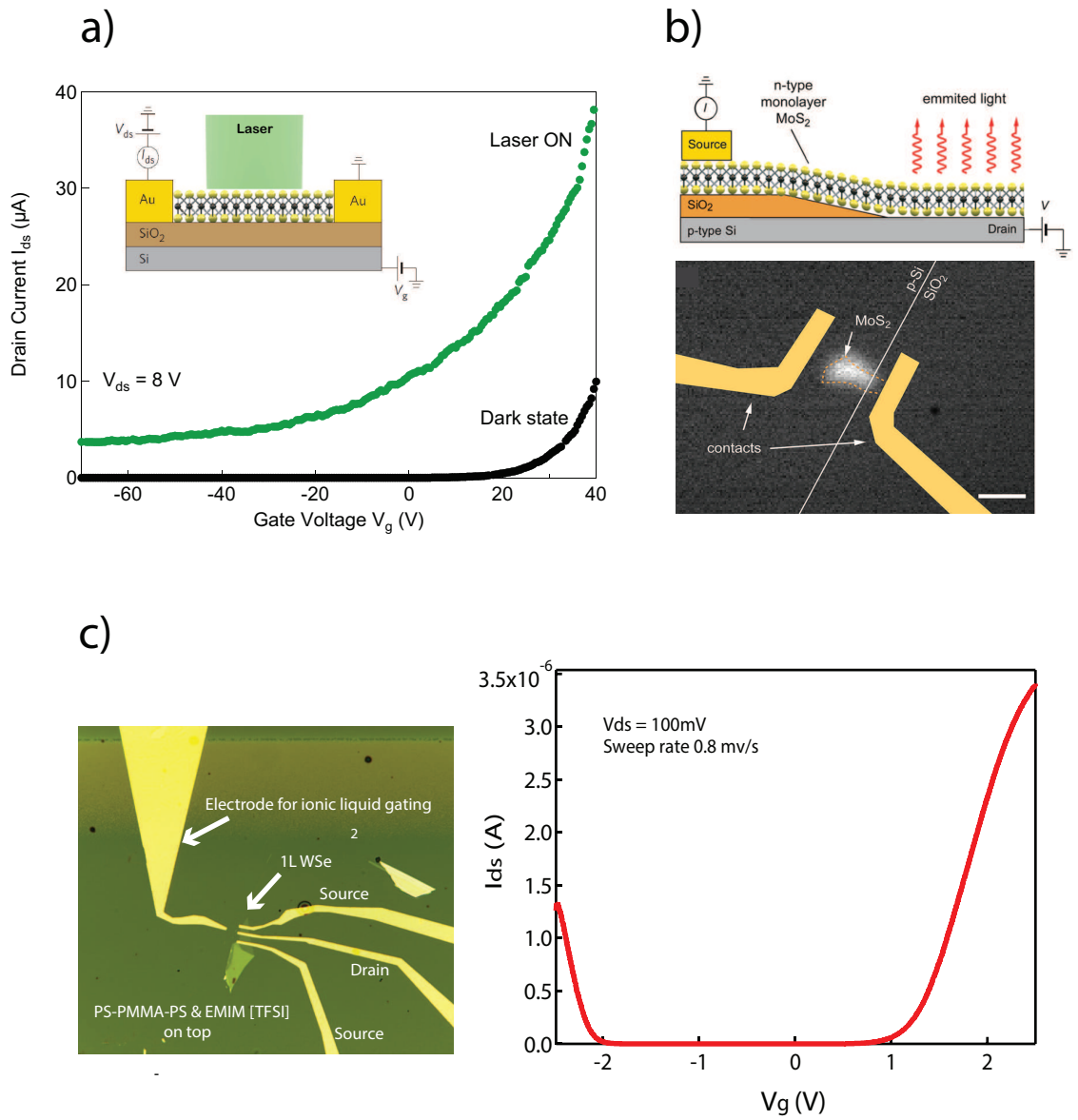


Figure 1.13: a) Transfer characteristics of a back-gated monolayer MoS_2 FET. The curves were acquired with (green) and without (black) laser illumination. The inset shows a schematic structure of the phototransistors. Adapted from [20]. b) Cross-sectional view of the p-n junction based on a vertical heterostructure of MoS_2 and p-doped Si (top panel). Map of electroluminescence intensity (bottom panel). Adapted from [109]. c) Optical image of a monolayer WSe_2 transparent field effect transistor gated by ionic gel (left). Ambipolar transfer characteristic for a bias voltage of 100 mV (right).

Chapter 2

Device Fabrication and Experimental Techniques

In this chapter I will discuss the method employed to fabricate the FETs and the spectroscopy techniques used in this thesis work. In particular the process flow, the transfer techniques for developing the transparent devices, and the electrical transport measurements will be discussed in details. Subsequently, I will introduce a basic background of the laser systems employed and the nonlinear optical processes involved in our experiments. Finally, I will introduce the optical pump-probe setup and the modulation spectroscopy apparatus. Several *conventional* spectroscopy techniques used for basic characterization such as Raman, photoluminescence, and UV-visible spectroscopy were carried out with commercial instruments and will be briefly discussed in this chapter, however the interpretation of the obtained data will be described in the following chapters for each specific purpose.

2.1 Single Layer MoS_2 Field effect Transistor: Microfabrication

Mechanically-exfoliated layered materials on Si/SiO_2 substrates represent a simple approach to build FETs in back gate configuration and then probing the physical properties of transition metal dichalcogenide materials. However, all our experiments are carried out in transmission geometry that requires a transparent sample. The transistor is built according to the structure in Figure 2.1 [18], using *c*-plane sapphire as the transparent substrate and 50 nm of ITO as the transparent back-gate electrode, deposited by using a silicon nitride stencil mask and an electron beam evaporator. The gate dielectric consists of 30 nm of HfO_2 deposited by atomic layer deposition (ALD). Monolayer MoS_2 has been grown by chemical vapour deposition on *c*-plane sapphire [30] and as synthesized MoS_2 was transferred from the sapphire to the target substrate (sapphire/ITO/HfO_2). This was done by using a wet transfer method that in general employed an organic polymer as a matrix to hold the flakes and a solvent to dissolve the polymer in a second step (these methods will be described in Section 2.1.1). After transferring the flakes, a surface analysis by atomic force microscope (AFM) is usually carried out in order to see if the layer suffered some mechanical damages during the process. Lithography is then carried out to pattern the flakes before the final deposition of the metal contacts. However, the presence of sapphire as an isolating substrate needs an extra step in the process flow. To disperse electrons and not to accumulate electrostatic charge during the electron beam lithography, a thin layer of Cr (15 nm) is deposited (by thermal evaporation) on the double-layer resist before the

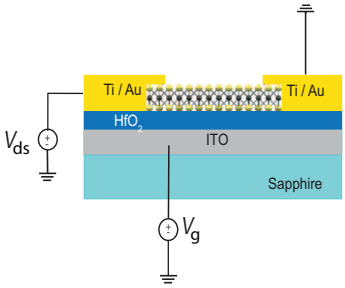


Figure 2.1: Schematic of the transistor geometry.

lithographic process.

2.1.1 Wet transfer techniques

In order to transfer the 1L-MoS_2 [112] two different approaches were adopted, both named *wet*. The first involves exposing the 2D materials to a solution of potassium hydroxide (KOH), and the second one exposing them to deionized water (DI). This can result in the adsorption of a large amount of ions (OH^- and K^+) and water, which is highly unfavourable to the charge transport properties and leads to some change in the optical properties of the 2D materials.

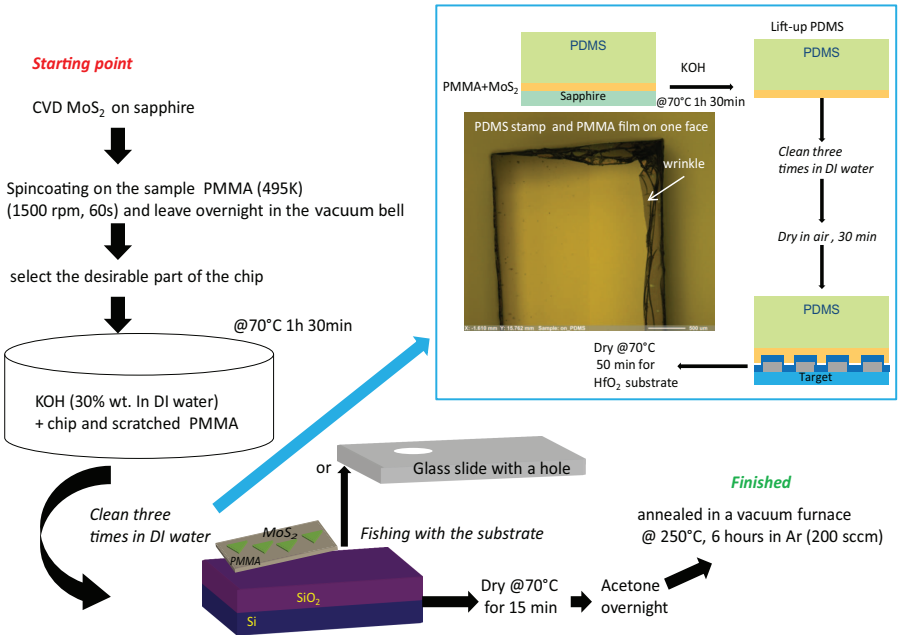


Figure 2.2: Process flow of the transfer method based on PMMA and KOH. The sketch inside the blue square is a variation of the method if HfO_2 is used as a gate oxide.

The process flow of the method which employed PMMA and KOH (30%) [30] is described in Figure 2.2. The monolayers of MoS_2 are first grown by chemical vapour deposition on *c*-plane sapphire. The sapphire carrying the flakes is then spin-coated at 1500 rpm with a 8% solution of PMMA (495k) in anisole and subsequently left overnight in

a vacuum bell. Afterwards the substrate is immersed in a 30 wt% solution of KOH in DI water, which is heated to 70 °C. Intercalation of KOH between the PMMA layer and the substrate promotes the detachment of the polymer film holding the flakes, which typically starts floating after almost 1 hour and 30 minutes. The film, containing the flakes, goes through three baths with DI water and after that a *fishing* procedure is carried out with a target substrate. Although this method allows to transfer intact large area films on SiO_2, the use of HfO_2 needs a modification of the protocol as well as more time and the employment of polydimethylsiloxane (PDMS) as a stamp. Since the hydrophobicity of HfO_2 does not allow the adhesion (or fishing) of the PMMA/MoS_2 films floating in deionized water, we use the system PDMS/PMMA/MoS_2 to contact the target chip under the optical microscope. The formed stack PDMS/PMMA/MoS_2/HfO_2/ITO/sapphire is kept at 70 °C for 50 minutes to dry the sample and to facilitate a better adhesion. Subsequently, a bath in acetone is carried out overnight to dissolve the PMMA. Then the chip (sapphire/ITO/HfO_2/MoS_2) is finally annealed at 250 °C in low vacuum (10^{-2} mbar) for 6 hours at 250 °C in a flow of argon gas (200 sccm).

Figure 2.3a,b shows an AFM image of a transferred flake, where the residues of polymer are still present on the MoS_2 surface. We are aware that for our experiments PMMA is optically inert and a more efficient cleaning procedure, such as brushing the surface of the flake with the tip of an AFM, could lead to a complete removal of the polymer, which is significant for transport properties.

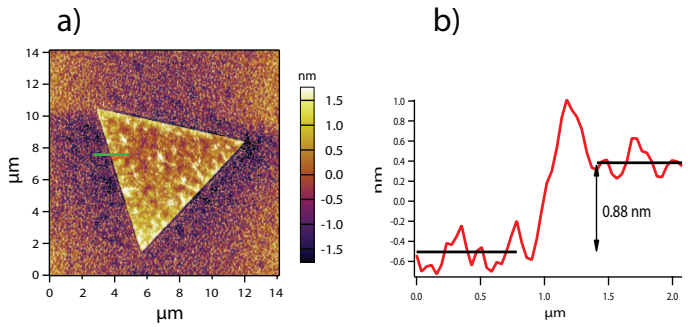


Figure 2.3: a) Topography map of a transferred flake. b) Line profile at the edge of the flake (green line) shows the estimated thickness of 0.88 nm. The estimation is close to the optimum value of 0.68 nm, nevertheless it is difficult to measure the real thickness of the transferred flakes due to polymer residues and solvents employed that result in a change of the electrostatic interaction between tip and sample.

In the second transfer approach a poly(L-lactic acid) polymer film (PLLA) is used. This method has been developed for the fabrication of transparent transistors based on selenides (*e. g.* WSe_2) and it was found suitable to transfer MoS_2 too. In fact, it is possible to clean the flakes after the process by using solvents while avoiding the annealing temperature which can lead to a deterioration of the electronic properties of the flakes as in the case of single layer WSe_2. As-synthesized MoS_2 was transferred from the sapphire to the target substrate (sapphire/ITO/HfO_2) using a glass slide covered with PDMS as a stamp, a film of PLLA as the holder for the flakes and deionized water promoting the detachment of the polymer. The process flow is described in Figure 2.4. The PLLA is first spin coated at 3000 rpm for 1 minute and then baked at 50 °C for 3 minutes. Successively, the polymer is scratched at the edge and approached with a glass slide covered with PDMS. Now that the two interfaces are stuck, a drop of DI water is gently placed onto the back

part of the chip (the glass slide is flipped over, see Figure 2.4). Intercalation of DI water from this drop between the PLLA layer and the substrate promotes the detachment of the polymer film holding the flakes. By peeling off the substrate we obtain the stack PDMS/PLLA/MoS_2 that is then placed in a homemade transfer station setup (Figure 2.5) and vertically aligned with the target. After approaching the target substrate, the system PDMS/PLLA/MoS_2/target (all in contact with each other) was kept at 100 °C for 4 hours to allow a better adhesion of the flakes. As the next step we carried out the following cleaning procedure: 1 hour in dichloromethane (PLLA solvent) that allows the separation of the target + flakes from the glass + PDMS stamp, bath of the chip in acetone (1 hour) and in isopropanol (2 hours), drying in N_2 for each step. Final annealing at 250 °C in low vacuum (10^{-2} mbar) for 6 hours in a flow of argon gas (200 sccm). The annealing in furnace is excluded from the process flow that concerns the structures based on WSe_2. In this case the temperature of the target, located in the manipulator, is kept at 90 °C and the final annealing in vacuum furnace is not carried out.

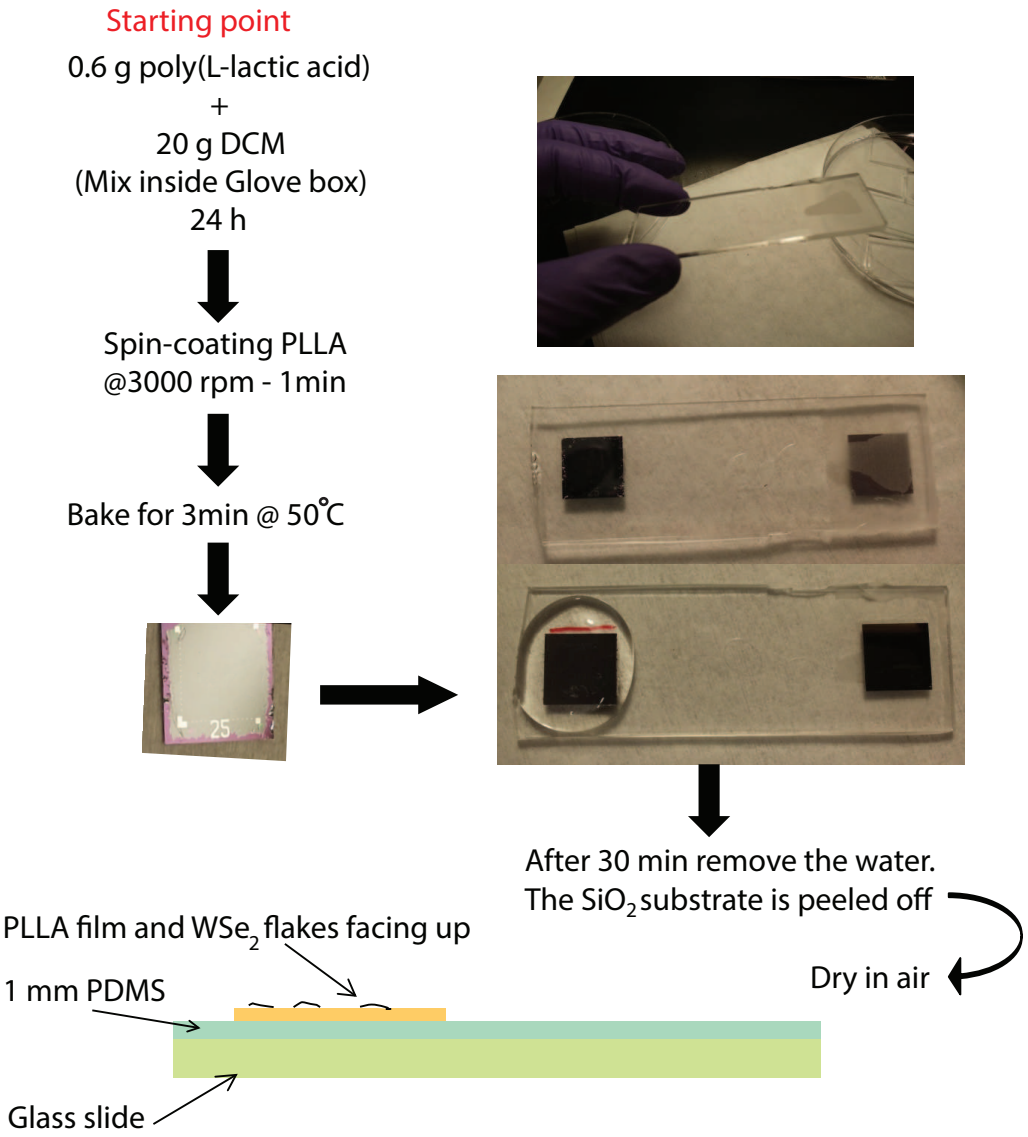


Figure 2.4: Process flow for the realization of the strips made from glass/PDMS/PLLA/flakes employed in the PLLA transfer method.

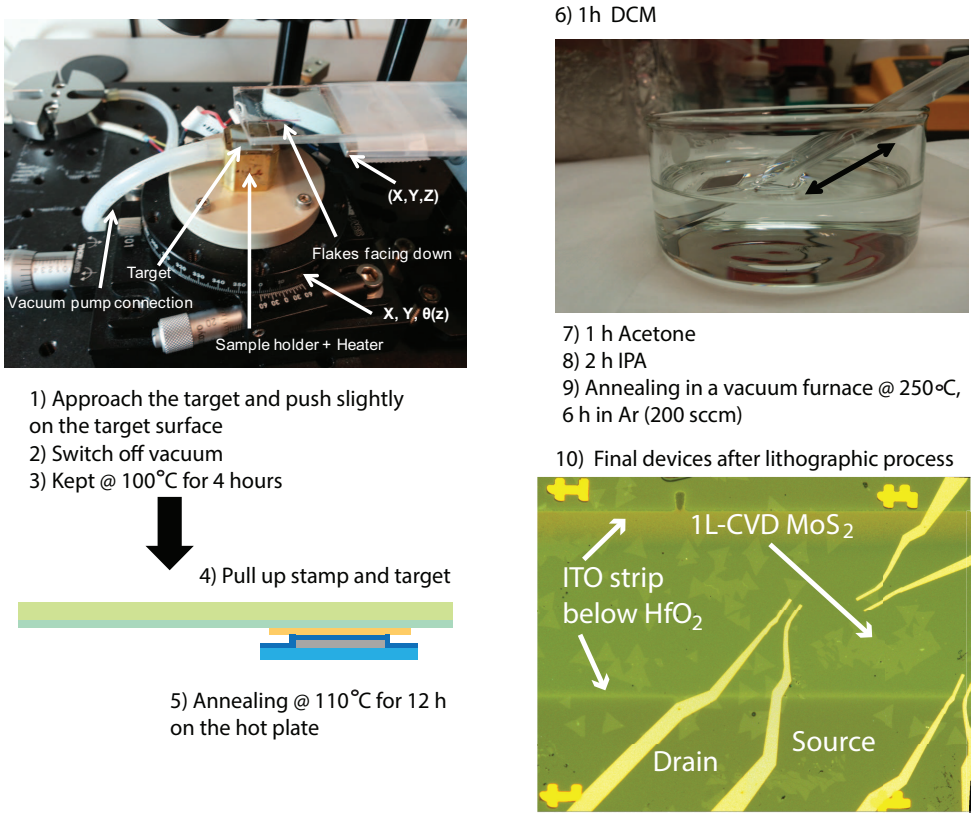


Figure 2.5: Manipulator station for a deterministic transfer of the nanostructures and subsequent cleaning procedure. In step 10) an optical image of the final FETs after lithographic process.

2.1.2 Transport measurements

After microfabrication we characterize our two-probe devices by using an Agilent E5270B parameter analyser and a home-built shielded probe station with micromanipulated probes. First of all we characterize our devices in air. Figure 2.6a shows the typical transfer characteristic for these devices. We observe a turn-on voltage V_{on} at positive values indicating that the 2D material is p-doped. Since the MoS_2 from any synthesis method is usually n-doped, which means a negative value of V_{on}, we ascribe the observed behaviour to adsorption doping such as molecular oxygen and water acting as electron acceptors [113]. As shown in Figure 2.6a,d we increase the gate voltage up to 5 V which is considered a safe value since the breakdown voltage of 30 nm of HfO_2 is around 7 V [114]. Since our aim is to vary the carrier density in the material, we are not interested in the realization of a performing device with a visible saturation region in the transfer characteristic [5]. The carrier density is calculated using the parallel-plate capacitor model [115] $n_{2D} = \varepsilon_0 \varepsilon_r V_{\mathrm{g}}/te$, with $\varepsilon_r = 19$ (for 30 nm HfO_2) giving us a variation of carrier density oscillating between 10^{12} and 10^{13} cm^{-2}.

The field effect mobility is calculated by the following expression:

$$\mu_{\mathrm{FE}} = \frac{1}{C_{\mathrm{ox}}} \frac{\partial \sigma}{\partial V_{\mathrm{g}}} = \frac{L}{W C_{\mathrm{ox}} V_{\mathrm{ds}}} \times \frac{\partial I_{\mathrm{ds}}}{\partial V_{\mathrm{g}}}, \tag{2.1}$$

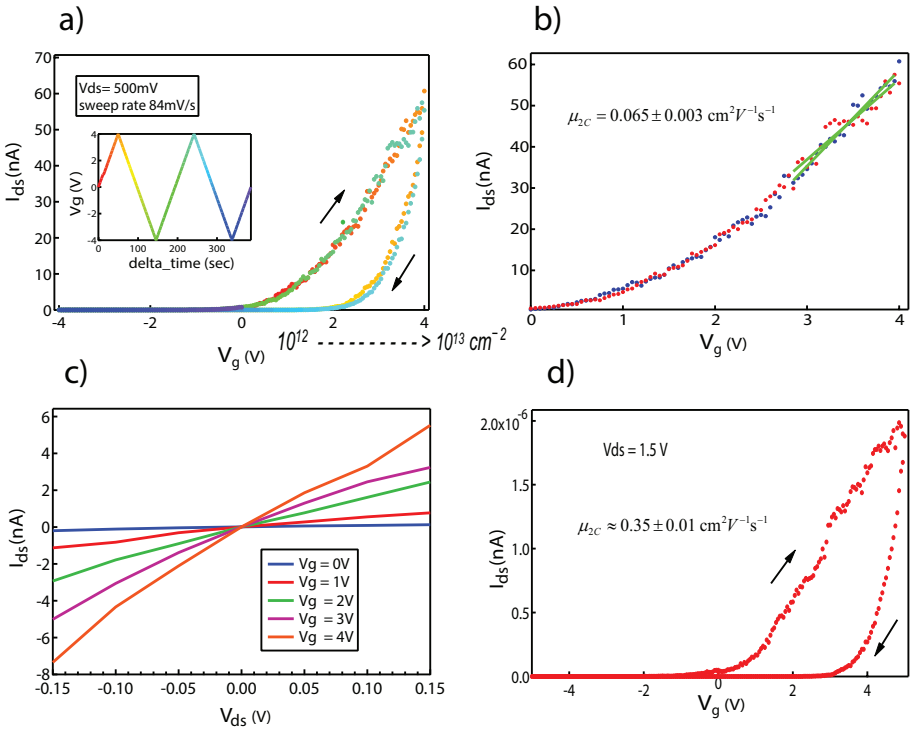


Figure 2.6: a) Transfer characteristic of a 1L-MoS_2 FET. The rainbow colours follow the gate voltage sweep cycles showed in the inset. b) Linear fit (green lines) for extracting mobility of the two almost reproducible arms of the transfer characteristic. c) Output characteristic at different gate voltages. d) Transfer characteristic of another device and best mobility achieved for this kind of devices in air is also reported.

where C_{ox} is the gate-to-channel insulator capacitance and V_{g} the gate voltage. σ is given by $G \cdot \frac{L}{W}$, where G is the conductance, W and L denote the width and the length, respectively, of the portion of the channel included between a pair of voltage probes. As shown in Figure 2.6b the linear fit of the transfer characteristic gives us the value $\frac{\partial I_{\mathrm{ds}}}{\partial V_{\mathrm{g}}}$. In our measurements we consider the two-contact effective field-effect mobility μ_{2C}. Hence, we neglect the contact resistance and assume that the bias voltage V_{ds} corresponds to the entire voltage drop over the semiconducting channel, thus underestimating the mobility [30]. It is instructive to note that μ_{FE} is related to the drift mobility $\mu = \frac{\sigma}{en}$ by the following expression:

$$\mu_{\mathrm{FE}} = \frac{e}{C_{\mathrm{ox}}} \frac{\partial n}{\partial V_{\mathrm{g}}} \cdot (\mu + \frac{\partial \mu}{\partial n} \cdot n), \tag{2.2}$$

so that the two mobilities are equivalent only, if the capacitor model applies ($\frac{\partial n}{\partial V_{\mathrm{g}}} \cdot e = C_{\mathrm{ox}}$) and if μ does not depend on n [116]. We estimate for our devices a mobility (in air) of the order 10^{-1} cm^2 V^{-1} s^{-1}. The output characteristic is usually linear in the range $\pm$150 mV, Figure 2.6c.

Annealing the device for 14 hours at 140 °C in high vacuum (10^{-5} mbar) we observe in the transfer characteristic a reduction of the hysteresis over the sweep cycles and an improved field effect mobility, Figure 2.7a,b,c,d. Moreover, it has been reported that the magnitude and direction of the charge transfer to the dopant molecules is modulated by an external electric field which explains the hysteresis commonly observed in the transfer characteristics of unencapsulated FETs exposed to ambient air [117]. However, in real

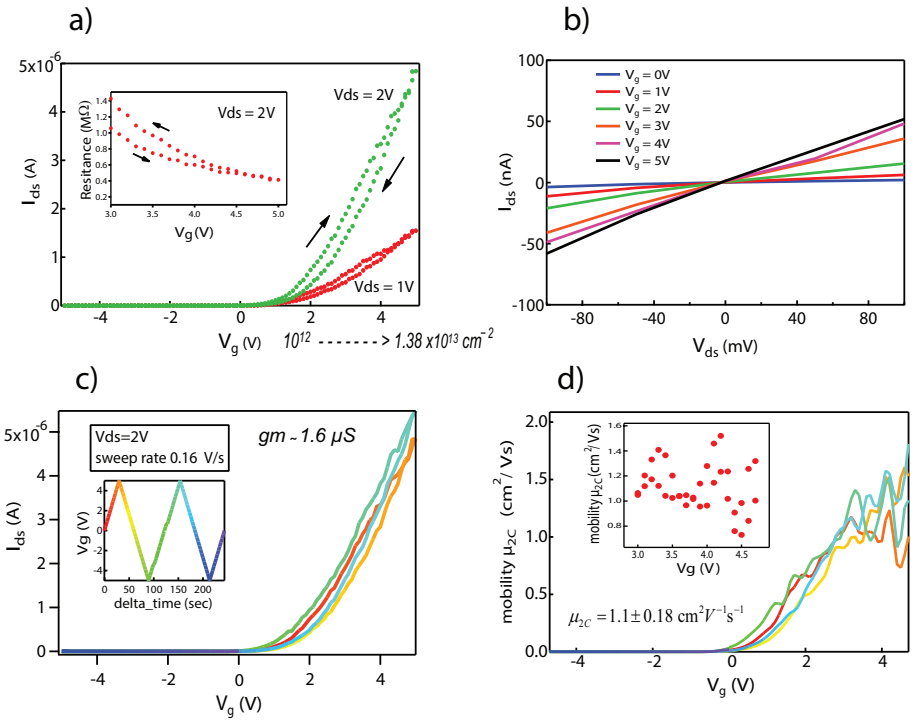


Figure 2.7: a) Transfer characteristics of a 1L-MoS_2 in vacuum at two different bias voltages. Inset shows the variation of the two probe resistance in the on-state region. b) Output characteristic at different gate voltages. c) Transfer characteristics of the same device in a) for two consecutive sweep cycles (shown in the inset). d) Display of the mobility for all the curves in c). The inset shows the mobility in the saturation region, where mobility does not depend on carrier density. The reported value of mobility is the average and standard deviation of these data.

samples, the presence of defects could significantly alter both the strength of the adsorption and the charge transfer. For instance, oxygen can be chemisorbed on sulphur vacancies and the resulting charge transfer (0.997 electrons) [70] is much larger than in the case of weak adsorption (0.041 electrons) [113]. This consideration can explain the hysteretic transfer curve in air, nevertheless its partial decreasing in vacuum still leads to some open questions.

2.2 Transient Transmission Spectroscopies

Transient transmission spectroscopy consists of the measurement of non-equilibrium populations that give rise to stimulated transitions [118]. This requires two-pulses experiment in order to be detected: a pulse acting as a pump and the other as a probe, hence the technique is called *pump-probe*. The first pulse (pump) perturbs the sample, leading to an excited state population. This photoexcitation will induce a change in transmission in our material:

$$T(t) \longrightarrow T_0 + \Delta T(t - t_0), \tag{2.3}$$

where T_0 and ΔT are respectively the initial value and the change induced by a pump pulse, impinging at time t_0. The transmission change is probed by a second pulse arriving to the sample with a certain delay τ with respect to the pump pulse. In order to see the relative variation in the probe transmission we need to detect the probe with and without

pump excitation. By varying the delay τ we can get the time dependence of the differential transient transmission $\Delta T(\tau)$. To understand the measured differential transmission signal, it is useful to consider a three-level system: one ground state and two excited states, as shown in Figure 2.8. When the pump interacts with the sample it induces a depletion of the ground state. If the probe pulse is resonant with a transition from the ground state to the populated state, the transmission is enhanced and a positive differential signal is generated. This is called photobleaching (PB). However, if the probe pulse is resonant with a transition from a populated excited state to a higher level, then the probe will be absorbed generating a negative signal, so-called photoinduced absorption (PA) [118]. Stimulated emission (SE) to the ground state can also arise, if the lowest excited state is dipole coupled with the ground state and the probe pulse is resonant with this transition, but in TMDCs it is hard to disentangle SE and PB. In this simple three-level system, the

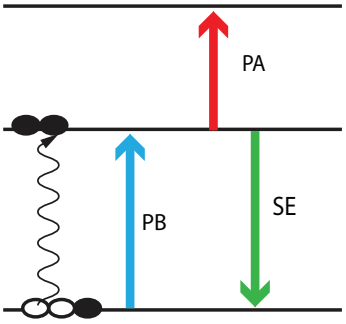


Figure 2.8: Three level system: one ground state and two excited states.

temporal evolution of all three possible signal contributions follows the time-dependent population of level 2. In real systems, more levels will be involved and their population dynamics can be disentangled with methods that will be described on a case-by-case basis in Chapters 3–5.

The pump-probe signal is customarily reported as the difference in transmitted probe intensity in the presence of the pump pulse and in the absence of it, normalized over the transmitted energy in the absence of the pump:

$$\frac{\Delta T}{T}(\lambda,\tau) = \frac{T_{\text{on}}(\lambda,\tau) - T_{\text{off}}(\lambda,\tau)}{T_{\text{off}}(\lambda,\tau)}. \tag{2.4}$$

In order to follow the dynamics of different populations, a broad band probe is required.

2.3 Ultrashort Laser Pulses

In this section I will discuss the working principles of the laser systems employed in our experiments. The Ti:sapphire crystal is a lasing medium which amplifies light in a broad range between 650–1100 nm. However, the laser operates most efficiently at wavelengths near 800 nm. The broad emission band is caused by an effective absorption transition from the ground state to the excited state of the Ti^{3+} ions (Figure 2.9).

To pump the medium and create inverted population one usually employs a continuous wave laser (CW) based on frequency-doubled solid-state Nd:YAG or Ar^{+} ion lasers. A common method for producing ultrashort pulses from lasers is the use of a mode-locking technique. The laser can oscillate simultaneously over all the resonance frequencies of the cavity. These frequencies make up the set of longitudinal modes of the laser which have a random phase Figure 2.10a. The mode-locking establishes a fixed-phase relationship

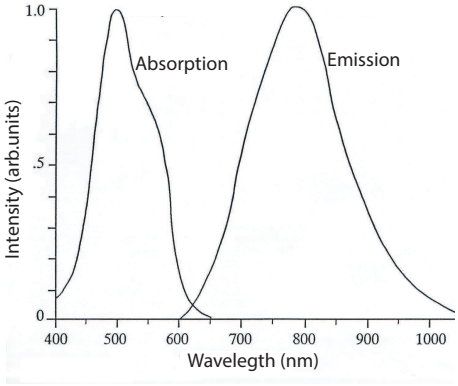


Figure 2.9: Absorption and emission spectra of the Ti:sapphire laser.

between these modes, aligning (in phase) different emitted laser modes with respect to each other. So that, locking their phase at a temporal position (*e. g.* at $t = 0$), the electric fields of all frequency components interact constructively up to a maximum of the total field strength and destructive interference will take place everywhere else Figure 2.10b. The

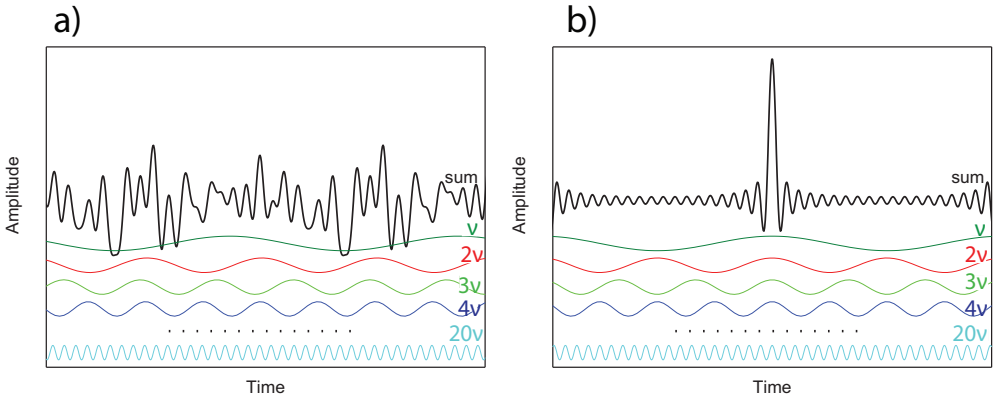


Figure 2.10: a) Illustration of interference between a few different modes of resonator without a) and with b) the phase-locking. Adapted from [119].

temporal duration of each pulse of light is determined by the number of in-phase modes in phase oscillating in the resonator. Therefore, Ti:sapphire is a good candidate for ultrashort pulse generation because of its broad laser gain. In the femtosecond laser, the peak power of mode-locked laser is orders of magnitude higher than the average power that remains the same in both CW and locked operating modes. To achieve a phase locking of the resonant modes we introduce a perturbation inside the cavity by *shaking* a mirror (inside the cavity) and then modulating the parameters of the resonator. The pulsed operation is then favored and it is said that the laser is mode-locked.

Since the electric field in the mode-locked operating mode is much higher than in the CW beam, Kerr-lens mode-locking can be used for producing short laser pulses. The Kerr effect is induced in the nonlinear medium (sapphire) by the beam itself, being the refractive index of the nonlinear material dependent on the intensity of propagating light (see also Section 2.4.1):

$$n = n_0 + \lambda K E^2, \tag{2.5}$$

where n_0 is the linear component of the refractive index, λ is the wavelength of the light,

K is the Kerr constant of the material, E is the electric field of the light. Therefore, the higher electric field causes an increase of the refractive index and the tighter focusing of the beam. The electric field intensity in the mode-locked operating mode (being much higher than in CW beam) will be focused more strongly, leading to a narrower beam in the real space. By cutting off the CW beam with an aperture, it is possible to suppress the CW component and then increase the losses of CW radiation leaving the mode-locked beam untouched.

Typically, Ti:sapphire oscillator can generate laser pulses from a few tens up to a few hundreds of femtoseconds. However, the maximum achievable peak power of the pulse is limited by the thermal damage threshold of the crystal. To overcome this problem, the output pulse from the oscillator is first stretched (pre-chirped), achieving lengths typically up to 1–100 ps. The resulting pulse is then seeded into the Ti:sapphire-based amplifiers, and it is amplified during a few round trips. After the amplification stage, the pulse is compressed back to its initial duration. While the oscillators can produce few-nJ pulses, it is possible to achieve up to 5 mJ/pulse energy with the repetition rate of 1 kHz. In this thesis two different laser sources are used. The pump-probe measurements are done by using a regeneratively amplified mode-locked Ti:sapphire laser, operating at 1 or 2 kHz repetition rate with 780 or 790 nm central wavelength, giving pulses with 100–150 fs duration. The measurements presented here were carried out at Polytechnic of Milano (Department of Physics); however, preliminary pump-probe experiments have been done in our department (Department of Complex Matter) by using a laser system Coherent Mira Seed oscillator with Coherent RegA 9000 regenerative amplifier. The repetition rate of this system is 250 kHz and it produces 50-fs pulses with the central wavelength at 800 nm.

2.4 Nonlinear Optics for Transient Spectroscopies

In this section I will describe two nonlinear optical processes: second harmonic and white light generation. The exploitation of these processes is relevant for the research work presented in this thesis. In our pump-probe experiments the pump excitation is generated by second harmonic generation through a suitable material. In this process two photons having the same angular frequency ω, when propagating through the material, can mix together, giving rise to a single photon with twice the original frequency. Hence, starting from a laser wavelength centered at 800 nm it is possible to generate a laser pulse at 400 nm wavelength to pump the samples. On the other hand, white light generation takes place when the laser pulse at the fundamental frequency (from a Ti:sapphire laser) is focused in a sapphire plate. We split the Ti:sapphire laser beam into arms so that the two processes occur independently to generate pump and probe.

The intensity dependence of the material response is what usually defines nonlinear optics. The description of nonlinear optical phenomena starts from the electromagnetic wave equation that derives from Maxwell's equations:

$$\nabla^2 E - \mu\varepsilon\frac{\partial^2 E}{\partial t^2} = 0, \tag{2.6}$$

with E electric field, μ permeability and ε permittivity. The oscillating electric field of the wave can induce a dipole moment, whose volume density is the electric polarization P, which depends on the susceptibility tensor. In a nonlinear medium and for high electric field values, the electric polarization becomes a nonlinear function of the field and can be written *via* a Taylor expansion:

$$P = \varepsilon_0\left[\chi^1 E + \chi^{(2)}E^2 + \chi^{(3)}E^3 + ...\right] = P^{\mathrm{L}} + P^{\mathrm{NL}}. \tag{2.7}$$

P is linear only in the presence of a weak field so $P \approx P^{\mathrm{L}} = \varepsilon_0 \chi^1 E$. The other terms of the sum are responsible for a series of nonlinear optical effects of higher order, such as second order effects generated by $\chi^{(2)} E^2$. In the nonlinear media, considering a nonlinear polarization interaction with the traveling wave, the propagation equation becomes:

$$\nabla^2 E - \mu\varepsilon \frac{\partial^2 E}{\partial t^2} = \mu \frac{\partial^2 P^{\mathrm{NL}}}{\partial t^2}, \tag{2.8}$$

which shows how the nonlinear polarization behaves as a source term, enabling interactions between traveling electric field and induced polarization. In many materials χ values decrease rapidly after third order, therefore second and third order nonlinear effects are the dominant ones [120]. Second harmonic generation (SHG) and white light generation (WLG) are second and third order effects that were exploited in the transient spectroscopy system and are briefly discussed below.

2.4.1 White light generation

The bandwidth of an ultrashort light pulse can be easily increased by an effect known as supercontinuum (white light) generation, a by-product of a combination of third-order effects that occurs when an intense light pulse is focused inside a transparent material, such as fused silica, sapphire or CaF_2. The white light generation can be understood as a result of self-focusing (SF) and self-phase modulation (SPM), both related to the Kerr effect. When an intense laser pulse passes through a material, the strong electric field causes the nonlinear dependence of refractive index on the laser intensity:

$$n = n_0 + n_2 I(t, z). \tag{2.9}$$

If now we consider a spatial dependence of a Gaussian wavefront, different parts of the field will be subject to a different refractive index, leading to a SF process at the center of the beam profile, which is more intense. Furthermore, the time-dependent variation of

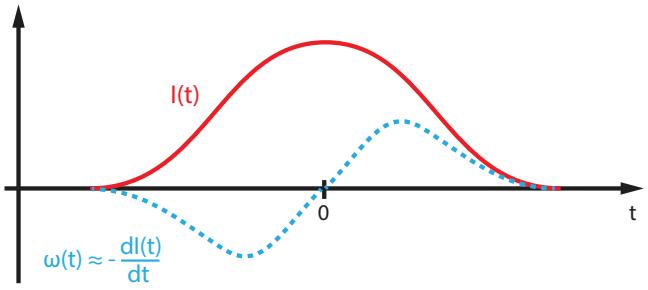


Figure 2.11: Intensity $I(t)$ and $\omega(t)$ time trend, which is proportional to $\frac{-dI}{dt}$. Adapted from [121].

the refractive index produces a phase shift in the different components of the pulse, and so broadening of its spectrum (SPM effect) [120]. In a medium of thickness L, the phase shift experienced by a quasi-monochromatic pulse of central frequency ω_0 is:

$$\phi(t) = \omega_0 t - \frac{\omega_0}{c_0} n(t) L = \omega_0 t - \frac{\omega_0}{c_0} n_0 L - \frac{\omega_0}{c_0} n_2 L I(t) \tag{2.10}$$

and the instantaneous frequency becomes:

$$\omega(t) = \frac{d\phi(t)}{dt} = \omega_0 - \frac{\omega_0 n_2 L}{c_0} \frac{dI}{dt} = \omega_0 \left(1 - \frac{n_2 L}{c_0} \frac{dI}{dt}\right). \tag{2.11}$$

Equation (2.11) shows that the instantaneous central frequency of the pulse changes in time; in particular (Figure 2.11), during the leading edge of the pulse ($dI/dt > 0$) it is shifted to red, while during the trailing edge ($dI/dt < 0$) it is shifted to blue, leading to a broadening of the spectrum. The new frequency components, obtained through this process, will be affected by strong chirp: all the frequencies will arrive at a different delay under the pulse envelope.

2.4.2 Second harmonic generation (SHG)

In this process, two photons having the same frequency ω, when propagating through a suitable material, can interact, giving rise to a single photon with twice the original frequency. For a plane wave of uniform intensity, we can write the following equation for the electric field $E_\omega(z,t)$ of the wave:

$$E_\omega(z,t) = \left(\frac{1}{2}\right)\{E(z,\omega)e^{i(\omega t - k_\omega z)} + c.c.\}, \tag{2.12}$$

where c.c. indicates a complex conjugate of the other term in brackets and:

$$k_\omega = \frac{\omega}{c_\omega} = \frac{n_\omega \omega}{c}, \tag{2.13}$$

where c_ω is the phase velocity in a nonlinear medium (crystal) of a wave with frequency ω, n_ω is the refractive index at this frequency, and c is the velocity of the light in vacuum. The induced linear P^{L} and nonlinear dielectric polarization P^{NL} that is related to the electric field E of the electromagnetic wave by the following scalar equations:

$$P^{\mathrm{L}} = \varepsilon_0 \chi E, \tag{2.14}$$

$$P^{\mathrm{NL}} = 2\varepsilon_0 d E^2, \tag{2.15}$$

where χ is the dielectric susceptibility and d is a coefficient whose dimension is the inverse of an electric field and it originates from the nonlinear deformation of the outer electrons of an atomic system, when subjected to a high electric field. Equations (2.14) and (2.15) show that the nonlinear polarization term becomes comparable to the linear one for an electric field $E \cong \chi/d$. Note that d must be zero for a centrosymmetric material. In fact, for reasons of symmetry a reversed sign of E leads to a reversed sign of the total polarization $P_t = P + P^{\mathrm{NL}}$. Nevertheless, being $P^{\mathrm{NL}} \propto E$, this can occur only if $d = 0$. Substituting Eq. (2.12) into Eq. (2.15) we can express P^{NL}:

$$P_\omega^{NL}(z,t) = \left(\frac{\varepsilon_0 d}{2}\right)\{EE^* + E^2(z,\omega)e^{i(2\omega t - 2k_\omega z)} + c.c.\}. \tag{2.16}$$

Equation (2.16) describes a polarization wave oscillating at frequency 2ω and with a phase constant $2k_\omega$, the term EE^* is the optical rectification (contribution at zero frequency). The polarization wave also contains the frequency $\omega = 0$ that induces the rise of a DC voltage across the crystal, on the other hand it is expected to radiate an electromagnetic wave at the second harmonic (SH) frequency. The radiated SH can be written:

$$E_{2\omega}(z,t) = \left(\frac{1}{2}\right)\{E(z,2\omega)e^{i(2\omega t - k_{2\omega} z)} + c.c.\}, \tag{2.17}$$

where

$$k_{2\omega} = \frac{2\omega}{c_{2\omega}} = \frac{2n_{2\omega}\omega}{c} \tag{2.18}$$

is the phase constant at frequency 2ω. Comparing Eq. (2.16) with Eq. (2.17), we can deduce that the SH process must satisfy an important condition: the phase velocity of the

polarization wave ($v_p = 2\omega/2k_\omega$) equals to the one of the generated wave ($v_E = 2\omega/k_{2\omega}$), that means:

$$k_{2\omega} = 2k_\omega. \tag{2.19}$$

This is the so-called *phase-matching* condition. If this condition is not satisfied, the difference in phase $\Delta k = (2k_\omega - k_{2\omega})l$ increases with the distance l (into the crystal), then the generated wave driven by a polarization that does not have the proper phase, does not grow with the distance l. The above consideration implies another condition to satisfy:

$$n_{2\omega} = n_\omega. \tag{2.20}$$

In a general anisotropic medium, the scalar relation (2.15) should be replaced by a tensor relation. This relation links $P^{2\omega}(r, 2\omega)$ and $E^\omega(r, \omega)$ for the $i-$ direction of the crystal:

$$P_i^{2\omega} = \sum_{j,k=1,2,3} \varepsilon_0 d_{i,j,k}^{2\omega} E_j^\omega E_k^\omega, \tag{2.21}$$

where d is a 3×6 matrix that operates on the column vector (EE). As mentioned in Section 2.4, the Eq. (2.21) can be written in term of susceptibility in the following mode:

$$P_i^{2\omega} = \sum_{j,k} \chi_{i,j,k}^{(2)} E_j^\omega E_k^\omega. \tag{2.22}$$

In a dipole approximation of the electron-photon interaction, the second-order susceptibility $\chi^{(2)}$ is a third-order tensor, with components corresponding to the various possible orientations of the crystal axis and of light polarization. In the ideal case of a plane wave the intensity of the generated SH is as follows:

$$I(2\omega) = \frac{2^7 \pi^3 \omega^2 \chi_{\text{eff}}^2 l^2}{n^3 c^3} I^2(\omega) \Big(\frac{\sin(\Delta k l/2)}{\Delta k l/2} \Big)^2. \tag{2.23}$$

The dependence on both the length of the material l and the incident intensity $I(\omega)$ is quadratic; n $(= n_\omega = n_{2\omega})$ is the index of refraction and c the velocity of light. The intensity of the doubled frequency is proportional to the square of an effective susceptibility χ_{eff}^2, which depends on the material. For the doubling yield to be maximum, the dephasing quantity Δk must be zero. As mentioned above, this dephasing term takes into account propagation effects during the doubling process. At any point along the propagation axis the electronic oscillators radiate at angular frequency ω and 2ω in the same direction k. After propagation over a distance l in the medium the fundamental frequency generates the second-harmonic frequency with a time delay $2k_\omega l$, while the previously generated second harmonic reaches the same point with a time delay $k_{2\omega} l$. If the distance l is such that the dephasing quantity is zero, then the two contributions add constructively; otherwise they interfere destructively [122].

2.5 Pump-Probe Setup

In this section I will describe the pump-probe setup that was used for the measurements reported in this thesis. The pump-probe experiment consists of a first pump pulse, which triggers a photoinduced process followed by a time-delayed probe pulse which monitors the system evolution, see Figure 2.12.

The laser source in different pump-probe setups is a regeneratively amplified mode-locked Ti:sapphire laser (Coherent Libra), operating at 1 kHz repetition rate with 780 nm central wavelength, giving pulses with 100 fs duration. The pump pulse is generated by

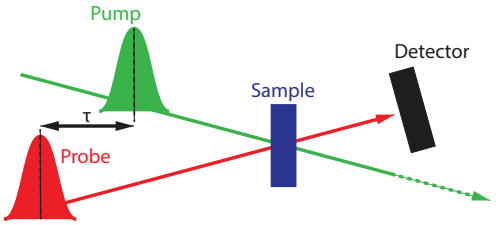


Figure 2.12: Schematic illustration of a pump-probe experiment.

frequency doubling the fundamental in a thin β barium borate crystal (BBO). The pump energy is set at 140 nJ / pulse. Broadband white-light continuum pulses generated in a sapphire plate, covering the 420 to 750 nm wavelength range, are used as probe pulses. Pump and probe pulses (both with the same polarization) are then focused on the sample and spatially overlapped. To avoid misalignment problems, the pump spot size is kept larger than the probe one (∼150 μm diameter). The delay between the two pulses is controlled through a delay line, mounted on a computer controlled translation stage, and usually the pump beam goes through this delay line, see Figure 2.13.

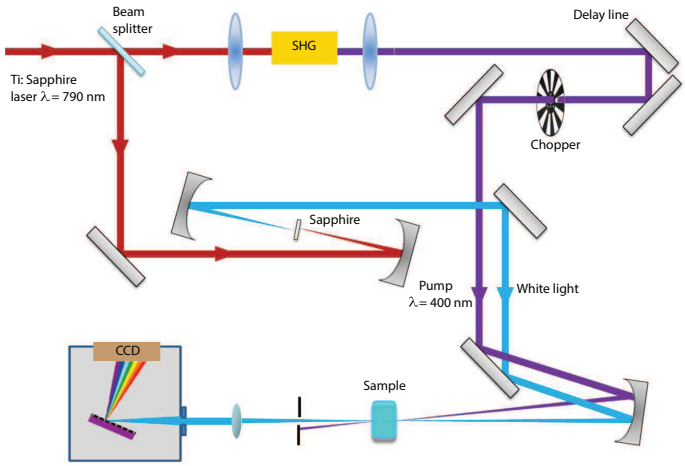


Figure 2.13: Pump-probe setup.

In order to acquire the probe spectrum with and without the pump excitation, a chopper modulates the pump pulses at half frequency of the laser repetition rate (500 Hz in our case), blocking the first pulse of two consecutive pulses. A software connected to a triggered spectrometer, will do the calculation $\Delta T/T$ using two consecutive pulses, the transient transmission spectrum will be the average of $\Delta T/T$ of hundreds of consecutive pulses for each delay. Therefore the detection is single shot: each single pulse is spectrally separated through a grating (or prism) and detected over the whole spectral range by using a 1024-pixel back-thinned CCD sensor S7030-1006 equipped with electronics specially designed for fast read-out times and low noise [123]. The 1 kHz system used for the experiments gives a SNR (signal-to-noise ratio) of around 10^{-4}. The measurement is repeated many times in order to increase SNR, averaging several consecutive sweeps.

2.5.1 Pump-probe microscope

If the sample we want to measure is very small, such as the single layer FET, it becomes necessary to combine temporal and spatial resolution [124]. The set up is not so different from the previous one, but to focus the pump and probe beams on the sample we cannot use the usual geometry based on lenses or mirror configuration. The laser system used in this configuration is a regeneratively amplified mode-locked Ti:sapphire laser, operating at 2 kHz repetition rate with 790 nm central wavelength and emitting 100 fs pulses. To have an imaging system the chip carrier is mounted on a translation stage made of two units, a motorized 2-axis translation stage for the micro-movement (resolution ∼625 nm) and a 3-axis computer controlled piezoelectric translation stage (with 1 nm resolution) that allows better accuracy and focus onto the sample too. With these two translation stages one can raster scan the sample in order to get an image. In order to have a high spatial resolution image by raster scanning the sample, we need to focus tightly both the pump and the probe beam on the sample (Figure 2.14a). To achieve this, without losing temporal resolution and avoiding chromatic aberrations, we use a reflective objective with a 15× magnification and a 0.30 numerical aperture (NA) to focus pump and probe pulses in collinear geometry (Figure 2.14a,b). Making the diameter of the probe beam bigger than the pump before the objective leads the probe pulse to have a sub-micrometer spot size on the sample and a pump pulse with a spot size ∼5 times bigger. The transmitted probe is collected with a 7.5 mm achromatic doublet, dispersed by a CaF_2 prism and detected by a Si CCD camera with 532 pixels, corresponding to a bandwidth per pixel of 1.1 nm. In this way we obtain a 3D transmission map $T(x, y, \lambda)$ and differential transmission $\Delta T/T$. In our experiment the pump pulse is modulated at 125 Hz by a mechanical chopper. This drastically reduces the intensity of the probe beam (white-light) so as not to re-excite the sample and keep rms fluctuations around 0.2%. On the other hand it has not been possible to do single shot acquisition but average the pump-probe signal over eight pulse T_{on} (and likewise T_{off}) for each scan point.

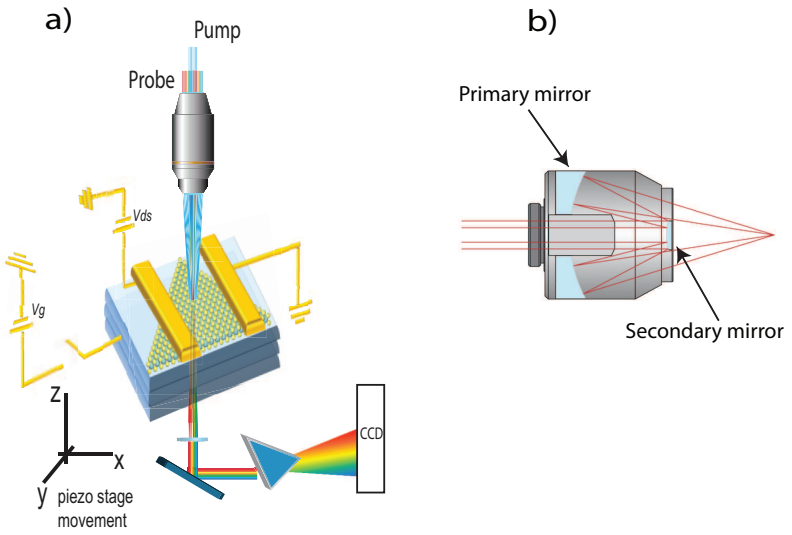


Figure 2.14: a) Pump-probe microscopy setup. b) Working principle of a reflective objective.

2.6 Modulation Spectroscopy

In this section I will describe the electro-modulation spectroscopy (EMS) that is a CW spectroscopic technique widely used to study the electroabsorption (EA) in organic and inorganic semiconductor materials. The obtained spectra from EMS are not time-resolved but the information that we can obtain makes it an important approach for describing the light-matter interaction such as the Stark shifts of the excited states in TMDCs, and moreover as a complementary technique to the ultrafast methodology. The EA data were collected with a homemade confocal microscope in transmission configuration, Figure 2.15. The light source consisted of a supercontinuum laser (NKT Photonics, SuperK Extreme) monochromated by an acousto-optic modulator (NKT Photonics, SuperK Select) in the 500–1000 nm region with line widths between 2 and 5 nm. The polarization of the laser is controlled with a half-wave plate and a linear polarizer. The light is focused on the device with a 0.7 NA objective (S Plan Fluor 60×, Nikon) and collected by a second 0.75 NA objective (CFI Plan Apochromat VC 20×, Nikon). The collected light is focused on the entrance of a multimodal glass fiber with a 50 μm core, acting as a confocal aperture and revealed by a silicon photodetector (FDS100, Thorlabs). The signal is then amplified by a transimpedance amplifier (DHPCA-100, Femto) and supplied both to a DAQ (to record the transmission signal T) and to a lock-in amplifier (SR830 DSP, Stanford Research Systems) to retrieve the differential transmission data ΔT. All data were collected by a custom Labview Software that also controlled the raster scan of the device via a 3D piezo stage (P-517, Physik Instrumente) and the laser system. The laser fluence is kept below 150 W cm^{-2} to avoid photodoping in the material. The complexity and the origin of the EA signal will be widely discussed in Chapter 4.

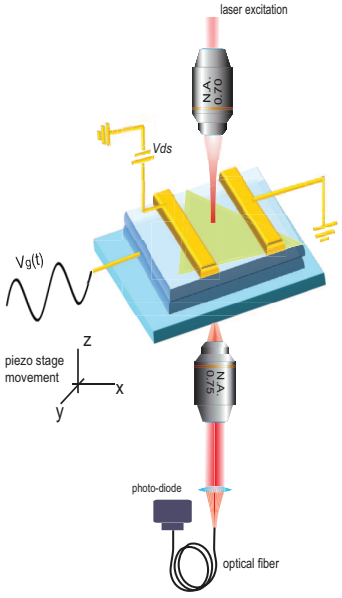


Figure 2.15: Schematic illustration of an Electroabsorption experiment in transmission geometry in a field effect transistor. The experiment is carried out by modulating the gate voltage V_g (with peak-to-peak voltage V_{pp}) in a transparent field effect transistor and simultaneously by scanning the sample with a light source, wavelength by wavelength, in the range 1.7 - 2.3 eV.

2.7 Equipment for Basic Optical Characterizations

Photoluminescence and resonant Raman scattering on MoS_2 FETs was performed with an NT-MDT NTEGRA Spectra confocal PL-Raman microscope in backscattering geometry with spectral resolution of $\sim$0.7 cm^{-1}. For our measurements we used the excitation line at 488 nm and a 100$\times$ objective (NA 0.9) to focus onto a spot size of $\sim$3 μm. The signals were detected with a CCD array at -80 °C. For the PL measurements we kept the laser fluence below 1 $kWcm^{-2}$. The Raman measurements on multilayer MoS_2 films, discussed in Chapter 5, were carried out by using a 20$\times$ objective (NA 0.4) to focus onto a spot size of 20 μm in order to evaluate the homogeneity of the obtained films. The optical absorption spectrum of the monolayer MoS_2 was recorded by using the electro-modulation confocal setup (see Section 2.6) that allows measuring of the transmission channel. For macroscopic samples like the multilayer MoS_2, the absorption spectra were recorded in transmission using a V-570 Jasco spectrometer with 0.5 nm spectral resolution, equipped with a single monochromator covering the spectral range from 190 to 2500 nm (6.52–0.49 eV).

Chapter 3

Field-Induced Charge Separation in Monolayer MoS_2

This Chapter is based on a submitted paper, D. Vella *et. al*: *Field induced charge separation in monolayer MoS_2* [125].

3.1 Introduction

In the past few years, layered two-dimensional semiconductors such as transition metal dichalcogenides (TMDCs) moved into the focus of nanoelectronics and -photonics research due to their exceptionally strong light-matter interaction combined with flexible processing and fabrication [6], [7], [13]. However, photoexcitation in TMDCs generates excitons with significant, thickness-dependent binding energy, reaching 400-700 meV in the monolayer case [81], [83], [87]. Hence, efficient photovoltaic and photodetector devices require measures to facilitate exciton dissociation into charge carriers, such as a vertical donor-acceptor heterostructure or an engineered p-n junction [9], [10], [109], [116], [126], [127].

Charge carrier photogeneration (CPG) is the enabling step for photovoltaics and photodetectors. In few-layer MoS_2 and WS_2 with exciton binding energies similar to the bulk values (50-150 meV), excitation well above the A and B resonances creates hot electron-hole pairs (C excitons at the band nesting region [128] and/or excitations in the continuum of valence and conduction band states). Upon relaxation towards the relative band maxima/minima they can either separate into free charge carriers or form A excitons, which give rise to excitonic fluorescence. In the few-layer case, separation into free carrier with a time constant of approximately 1 ps is the dominant process [96], [100], while in the monolayer case, due to the larger binding energy, a significant fraction of A excitons are formed. However, the observed photovoltaic effect and photocurrent suggest that, to a lesser extent, charge carriers form also in monolayers. The Photoluminescence (PL) quantum yield of monolayer MoS_2 decreases as excitation photon energy increases [84], [128], indicating that also in the case of monolayer hot electron-hole pairs can separate into charge carriers.

To gain further insight into the charge generation mechanism we propose to modulate its efficiency by applying an electric field [129]. We use monolayer MoS_2 as the channel of a field-effect transistor (FET, see Figure 3.1a,b) and apply an in-plane electric field via the source-drain voltage. The transistor is built in a bottom-gate configuration, using sapphire as the transparent substrate and 50 nm of ITO as the transparent back-gate electrode (Figure 3.1a,b). The gate dielectric consists of 30 nm of HfO_2 ($\varepsilon_r = 19$). The distance $\Delta\omega = 19.6$ cm^{-1} between the two Raman peaks in Figure 3.1c confirms the monolayer thickness [57]. In the first step, we show that the photoluminescence (PL) of the MoS_2 FET is progressively quenched upon the application of increasingly strong in-plane electric

fields. Subsequently, we perform femtosecond optical pump-probe microspectroscopy to directly monitor the fate of the hot electron-hole pairs and the carriers arising from their dissociation. For increasing field strengths, we observe an enhanced formation of carriers during the first few ps. Both findings suggest that the electric field facilitates the separation of photogenerated charge pairs. The time and field dependent dissociation probability provides insight into the separation mechanism.

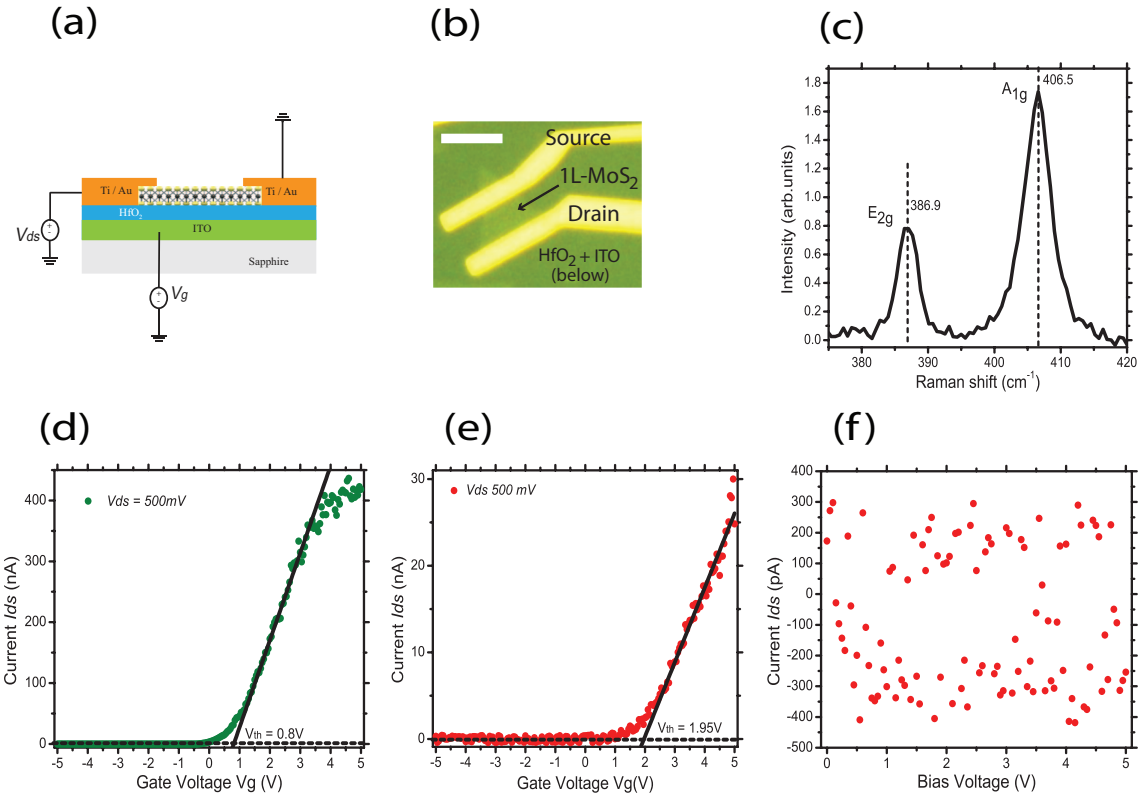


Figure 3.1: a) Schematic illustration of the transparent field effect transistor. b) Optical image of the device. Scale bar is 10 μm. c) Raman modes of the single layer MoS_2. d) Transfer characteristic (I_{ds}-V_g) of the device immediately after the microfabrication process. e) Transfer characteristic recorded before the optical measurements. f) Output characteristic shows negligible charge injection (for $V_g = 0$ V).

3.2 Photoluminescence and Electric Field

The transfer characteristic of the device (Figure 3.1e) presents a turn-on voltage (V_{on}) around 1.9V. We ascribe this to adsorption doping since the measurements are carried out in air [113]. Source-drain voltages up to 5V (at $V_g = 0$ V) are possible without appreciable charge injection, Figure 3.1d,e,f. This allows to observe the isolated effect of field-induced exciton dissociation without signal contributions from injected charges.

The PL spectrum of monolayer MoS_2 (Figure 3.2b) shows one main feature around 1.85 eV [21], [22]), slightly red-shifted compared to the A exciton resonance in absorption [85], [130] (Figure 3.2a). The shape of this feature suggests two overlapping peaks, one from neutral excitons A^0 and one from charged trions A^- due to the doping of the sample [85], [87], [113], [131], [132]. If we apply an in-plane electric field via the source-drain

voltage, the PL intensity progressively decreases as the field increases. For the highest bias used, $V_{ds} = 5$ V, which corresponds to an electric field of 7 kVcm^{-1}, the PL is quenched by about 35 % (Figure 3.2c). The field-induced PL quenching is weaker than observed in heterostructures such as MoS_2/WSe_2, where the integrated PL at the heterojunction decreases, respectively, by 81% and 98% compared to isolated MoS_2 and WSe_2 monolayers. In the heterojunction the band alignment promotes the charge separation and the charge transfer mechanism is faster than any other radiative or non-radiative decay channel [10], [133]. The field-induced PL quenching observed here can in principle have two different origins: either the A excitons and trions, which give rise to fluorescence, have a certain field-enhanced possibility to dissociate during their lifetime, or the field influences the branching ratio between bound states (A excitons and trions) and free carriers during the initial relaxation of hot charge pairs.

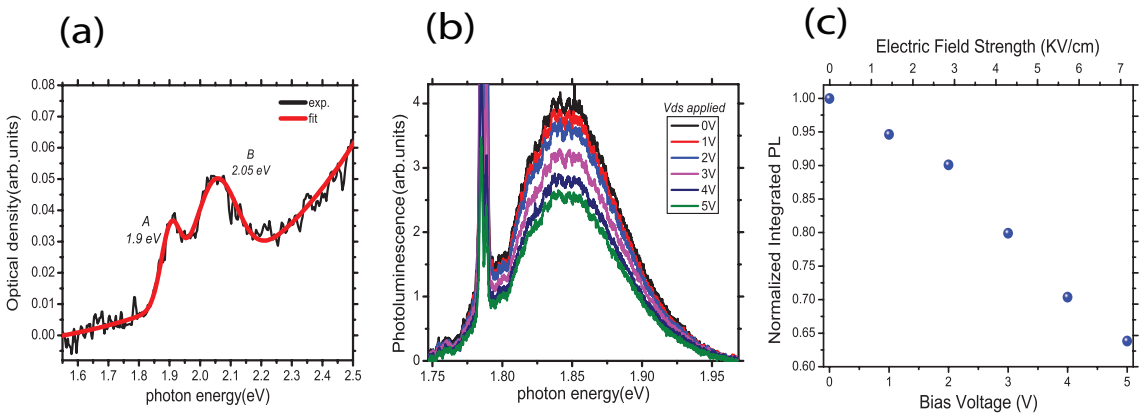


Figure 3.2: a) Extinction spectrum of the MoS_2 monolayer (black curve). Fit by using two Gaussian peaks and a generic exponential function to account for the background from various scattering mechanisms. b) PL spectra for different bias voltages applied. c) Normalized integrated PL as a function of the electric field strength.

3.3 Femtosecond Optical Spectroscopy and Electric Field

In order to resolve the temporal dynamics of the field-induced charge generation we employed an electric-field-assisted pump probe microspectroscopy. The microscope is built in collinear geometry (Figure 3.3a). A broadband white light is focused onto a spot of $\sim$ 800 nm diameter by a reflective microscope objective. By using a piezo–nanopositioner we scan the sample with the probe beam. Once the area of interest is selected, the probe is centered inside the FET channel and a pump pulse (3.1 eV) is successively focused onto the sample collinearly with the probe (spot size 5 times bigger than the probe).

The transient transmission $\Delta T/T$ is directly related to the photoinduced change in the absorbance:

$$\frac{\Delta T}{T} = -\Delta\alpha(\omega, t)d, \tag{3.1}$$

with $\alpha(\omega)$ the absorption coefficient and d the sample thickness. The absorption coefficient can be expressed as the product of the density of absorbers n and their absorption cross-section $\sigma(\omega)$:

$$\Delta\alpha(\omega, t) = \sum_i (n_i(t)\Delta\sigma(\omega, t) + \sigma_i(\omega, t)\Delta n(t)). \tag{3.2}$$

In most cases, the second term in Equation (3.2) dominates and the signal evolution follows the evolution of excited states' populations. However, Stark effect due to photogenerated charges [96], the Burstein-Moss effect [134], and, in particular, band-gap renormalization [90] may engender an appreciable change in the absorption cross-section, leading to a non-negligible first term. However, in all three mechanisms the effect is due to the presence of photoexcited states, hence, $\Delta\sigma$ should also follow their population. It is therefore justified to assume that the $\Delta T/T$ signal evolution follows the photoexcited states' population dynamics.

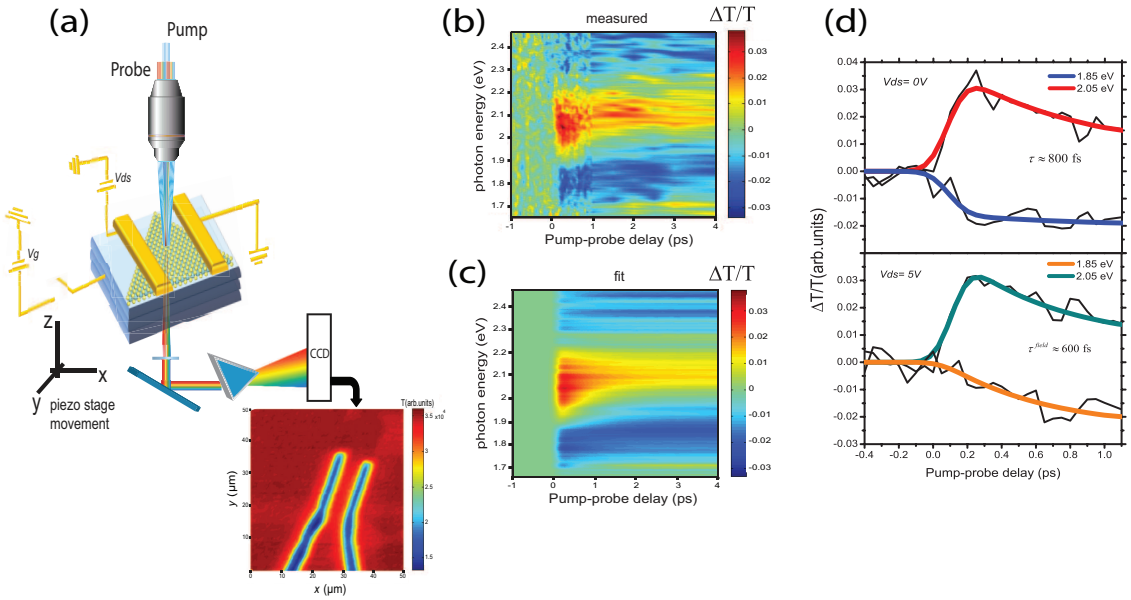


Figure 3.3: a) Schematic illustration of the pump-probe microscope setup. b) The transient transmission contour plot as a function of the probe photon energy and pump-probe delay (at 0 V). c) Contour plot of (b). d) Dynamics at 1.85 and 2.05 eV with (bottom-panel) and without field (top-panel).

The transient transmission contour plot as a function of the probe photon energy and pump-probe delay is shown in Figure 3.3b. The spectra show two photoinduced absorption features (negative signal at the spectral windows around 2.4eV and 1.8eV) and a bleaching peak (positive signal) in correspondence of the excitonic resonances A and B. The A and B peaks are merged into one due to the high excitation density resulting from the tight focusing (for the interpretation see Section 3.5). The PB is formed immediately during the time resolution of the instrument (pump-probe convolution) and decays and narrows with increasing delay. The two PA features also form immediately, but continue to grow and to broaden. Such behavior suggests that the signal originates from at least two distinct excited state populations, a primary one that is directly created by photoexcitation, and a secondary one that forms from the relaxation of the former. The primary population are the hot electron-hole pairs created by photoexcitation, while the secondary one is an ensemble of A excitons and trions and free carriers, in unquantified proportion.

Figure 3.3d shows the time evolution of the signal at two selected probe photon energies–the PB at 2.05 eV which forms within the time resolution of the instrument and decays rapidly, and the PA at 1.85eV which shows a delayed formation after the initial rise. Both the PB decay and the PA formation can be fitted as a single-exponential process with a time constant of 800 fs, which is very similar to the 700 fs reported for multilayers

[96] and is indicative of the time scale for the relevant relaxation processes of hot charge pairs into A excitons and free carriers. Upon application of an electric field (again 5 V, as in the PL quenching experiment above), the time constant becomes slightly faster and the PA contribution to the signal at 1.85 eV is significantly stronger.

To model the signal over the first few ps, we assume that photoexcitation creates a primary population $P(t)$ of hot electron-hole pairs. $P(t)$ evolves into a secondary population $S(t)$ of A excitons and free carriers with a time constant $\tau_1 = 1/\mathrm{k}_1$:

$$\begin{aligned} \frac{dP}{dt} &= G(t) - k_1 P \\ \frac{dS}{dt} &= +k_1 P, \end{aligned} \tag{3.3}$$

with G(t) the exciton generation term (pump-probe cross-correlation, approximated as a Gaussian). This simple model reproduces the data very well (Figure 3.3c) with a time constant $\tau_1 = 800$ fs.

The spectral contributions of the ensemble populations $P(t)$ and $S(t)$ are shown in Figure 3.4a. The main difference is that $S(t)$ has a weaker and narrower PB and a stronger and broader PA at the low-energy side. Figure 3.4b shows the population dynamics, the simple evolution of one ensemble into the other during the relaxation with a time constant τ_1. As has been shown recently [90], the excitation of hot electron-hole pairs does not change the occupation of the states relevant for the A and B absorption peak. The $\Delta T/T$ signal immediately after photoexcitation is dominated by the first term of Equation (3.2) due to a combination of band gap renormalization and screening of the exciton binding energy, which leads to a spectral shift of the absorption spectra. Subsequently, the relaxation towards A excitons and trions as well as free charges changes the relevant states' population and the second term of Equation (3.2) becomes more important for $\Delta T/T$ signal. Its most dominant features are the bleaching of the excitonic transitions and the PA feature below 1.9 eV due to free carriers [96], [100], [135].

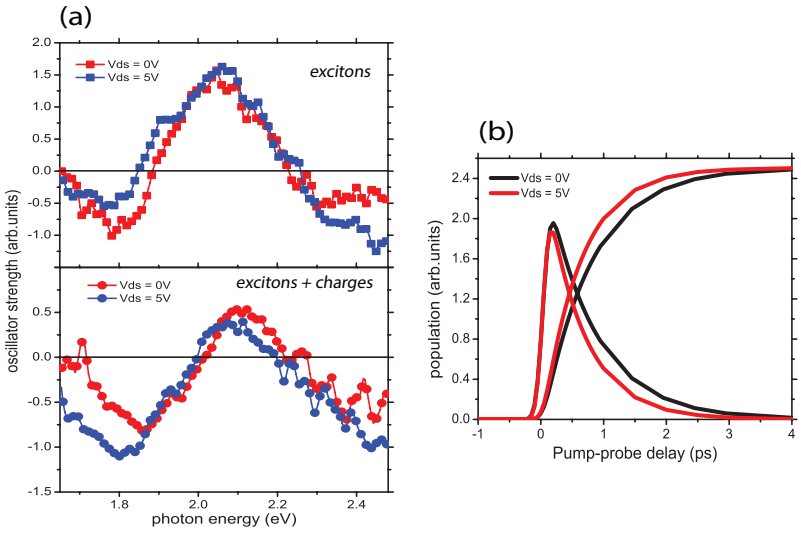


Figure 3.4: a) Spectral contributions of excitons (top-panel) with and without electric field. Spectral contribution of the ensemble excitons+charges (bottom-panel). b) Time-dependent (initial and final) ensemble populations.

Upon applying an in-plane electric field like in the PL quenching experiments, τ_1 reduces to 600 fs and the difference between the spectra of the ensembles $P(t)$ and $S(t)$ becomes

more pronounced: the PB of $S(t)$ is weaker and the low energy PA is stronger than in the case of electric field absence. This suggests that the applied field increases the concentration of charges in the ensemble $S(t)$ by increasing the exciton dissociation yield.

To further illustrate the differences in the evolution of the $\Delta T/T$ spectrum with and without the electric field we now consider the signal $\Delta(\Delta T/T)$ as a difference of the differential transmissions:

$$\frac{\Delta(\Delta T)}{T}(\omega,t) = \left(\frac{\Delta T}{T}(\omega,t)\right)_{Field} - \frac{\Delta T}{T}(\omega,t)$$

$$\frac{\Delta(\Delta T)}{T}(\omega,t) = -d\sum_i [\Delta_F n_i(t)]\sigma_i(\omega) - d\sum_i n_i(t)[\Delta_F \sigma_i(\omega)]. \tag{3.4}$$

The first term in Equations (3.4) describes field-induced changes (indicated with Δ_F in the equation) in the excited state populations while the second term indicates field-induced changes (Δ_F) in the oscillator strength (Stark shift of the excited state [136], [137]). For the used in-plane electric field strength a Stark shift less than 1 meV has been

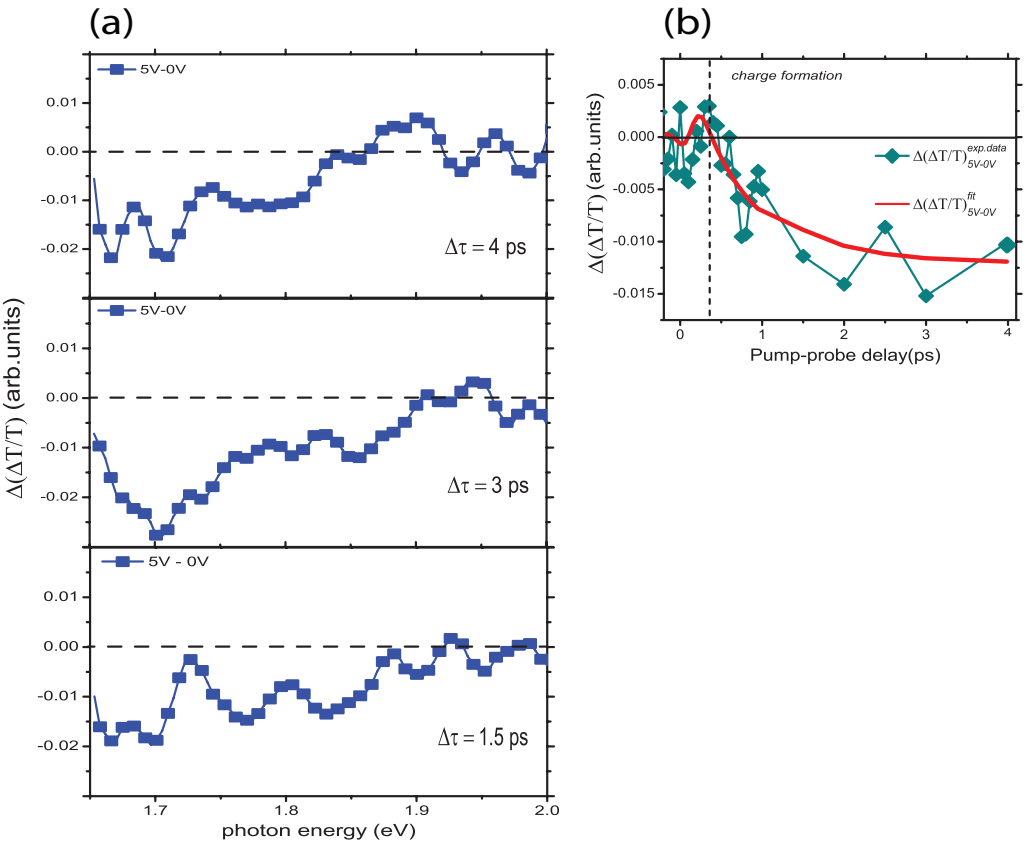


Figure 3.5: a) $\Delta(\Delta T/T)$ spectral feature for three different delays (1.5, 3, 4 ps). b) Temporal evolution of the absorption feature, observed in $\Delta(\Delta T/T)$ signal, averaged over the energy interval 1.65–1.85 eV.

predicted [138], which should give a $\Delta(\Delta T/T)$ contribution of $\sim 1\%$ of $\Delta T/T$. However, the potential difference between the source or drain and the gate electrode may be several Volts, resulting in a strong transverse electric field. Gate voltage of 0.5 V already results in a broadening and lowering of the A peak of approximately 15% [136]. Hence, we cannot exclude a Stark shift contribution to the $\Delta(\Delta T/T)$ signal. In fact, the spectrum of the

initial exciton population shown in Figure 3.4a changes slightly with field, in particular it develops a low-energy shoulder that, due to its strong overlap with the neighboring PA feature, also reduces the PA signal in the range 1.75-1.85 eV. Given the significant noise level of our signal, we cannot decide whether this difference in the $P(t)$ spectra is an actual Stark effect or a simple artefact originating from the noise. Therefore, the $\Delta(\Delta T/T)$ signal may have both a contribution from field-induced change in the populations (following the spectral shape of these populations and the temporal evolution of the change in population) and from the Stark effect (following the change in the spectrum and the temporal evolution of the population).

The most important $\Delta(\Delta T/T)$ spectral feature is an increase of the absorption over the energy interval 1.65-1.85 eV (Figure 3.5a). It is of similar magnitude as the $\Delta T/T$ signal. Hence the additional PA in this region due to the electric field is comparable to the PA of the $S(t)$ population, pointing towards a sizable increase in the charge density due to field-induced charge separation. The temporal evolution of this signal, integrated over the energy interval 1.65-1.85 eV is shown in Figure 3.5b. Initially, when the amount of extra charges is negligible, the signal is positive, since it is dominated by the increased PB of excitons, either by Stark effect or a noise artefact, seen in Figure 3.4a. Gradually, as the field-induced population of charges builds up over a few ps, their PA starts to dominate the whole spectral window.

Our results show that the moderate electric field of a few 10 kVcm^{-1} can significantly modulate the branching between different relaxation paths for photogenerated hot electron-hole pairs in monolayer MoS2: towards fluorescent A excitons and trions on the one hand, and free carriers on the other. The electric field skews the ratio towards free carriers, suggesting a field-induced charge separation during the hot charge pair relaxation. For a subsequent dissociation of the relaxed excitons due to the distortion of the excitonic Coulomb potential, the in-plane field is too weak [138], [139]. During the relaxation, the carriers undergo multiple scattering processes upon phonons and defects. During this diffusive process [140], [141], [142], a certain fraction of the charges remains within the capture radius r_c for the formation of excitons or trions, while the others diffuse beyond r_c and contribute to the photocurrent. The electric field increases the average separation and enhances the photocurrent on the expense of photoluminescence.

3.4 Photoluminescence Consideration

Although the neutral exciton transition is concealed by the emission from the trion state, we assign the position of A^0 and extract the splitting between exciton and trion of 48meV by using another device (from the same batch), Device 2. The peculiarity of this device is a weak current Ids (18 nA at $V_{ds} = 5$V and $V_g = 0$) and a leakage current through the dielectric layer in the gate channel. Figure 3.6a (left panel) shows the typical working principle of a FET in on-state. For a certain gate voltage (assuming for Vg > 0) the channel is " open " and current I_{ds} can flow if bias is applied (V_{ds}). Typically, under operating condition, the gate current I_g must be negligible. Indeed, to characterize the device we use a device parameter analyzer that allows to source voltage and measure current in both channels (gate-source and drain-source). Figure 3.6a (central panel) shows a leaky device where the gate current (I_{gs} is not negligible anymore and flows from the gate to the source (grounded). This current often increases with the gate-voltage during the measurement to record the transfer characteristic. In this kind of device the leakage is most probably due to a tunneling via the gate insulator (in the region below the metal contact). Our experimental condition is depicted in Figure 3.6a (right panel). Although this kind of device is not useful for any purpose, we exploit it with a trick that consists in having

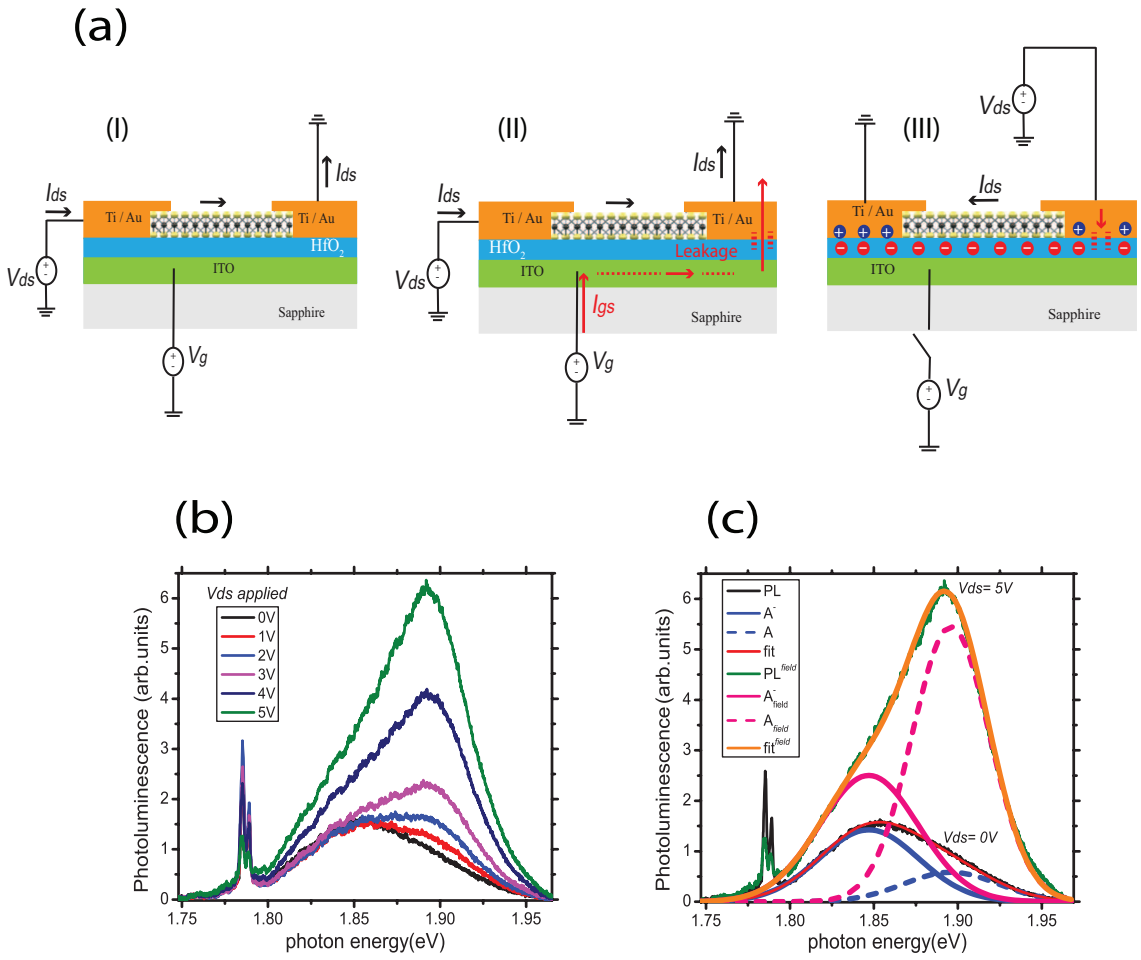


Figure 3.6: a) Schematic illustration of an operating FET (I), with a leakage current (II), with a leakage current and the floating gate (III). b) PL spectra for different bias voltages applied. c) PL spectrum fitted by using two Gaussian curves.

a free floating gate (gate disconnected) and a bias voltage applied (V_{ds}). This leads an accumulation of the electrons, which flow though the leak (via tunneling), in the gate oxide. Once we have created the electron trap, the accumulated charges generate an electrostatic potential similar to the condition of a plate capacitor. However, in this experiment a small fraction of current was detected in drain-source channel injected via tunneling through the electrodes (free carriers).

Figure 3.6b shows PL measurements for different bias voltage in this device. For the unbiased condition the PL is dominated by the overlapping trion/exciton emission, whereas under bias the A^0 becomes prominent and increases almost eight times. The tunability of the photoluminescence with the doping and similar spectra was already observed in MoS_2 FET [85]. In our particular case, the drain-source voltage acts as a gate regulator operating from 0 V towards the undoped region like in Ref. [85]. Indeed, the response of our device depicted in Figure 3.6b shows an increase of the exciton PL contribution already at 1 V that grows and becomes dominant at 5 V. This effect suggests an evolution from the initial condition where the two peaks overlap, one from neutral excitons A^0 and one from charged trions A^- (due to the initial doping of the sample), towards a final state where the photoluminescence from the neutral exciton is dominant. The similarity with data

depicted in Figure 1.8b (right panel) suggests that our experimental data are close to the ones reported by K.F. Mak *et.al* where the PL peak shifts from the trion to the exciton peak, for reverse gate voltage. Hence, the electron trap mechanism in a leakage device with the gate floating and a positive bias applied acts as a reverse gate voltage-induced change. Moreover, in the data reported by K.F. Mak *et.al* for negative voltage the device is in off-state and from the PL data the emission from the neutral exciton confirms that the material is less doped. Similarly, from our data we can assume the same condition by applying a bias voltage.

From the Gaussian fit (Figure 3.6c) we make a rough estimation of the A^0 - A^- splitting (48 meV). However, by using this method we give an indirect estimation of the peak positions of Device 1 (described in Section 3.2) without considering an eventual small shift of the PL contributions due to the electric field (used in our experiment). Following this approach, and using the previously calculated splitting, we can tentatively estimate the efficiency of the dissociation process in Device 1 (Figure 3.2b). By using the calculated area from the Gaussian fit, independently for A^0 and A^- at 5 V and 0 V (curves depicted in Figure 3.2b), it is possible from the obtained ratio to estimate a reduction of the involved populations of 40% for A^- and 30% for A^0. This could be ascribed to different dynamics during the relaxation process of excitons and trions. To verify this hypothesis more investigations such as low temperature PL and Transient transmission measurements are needed. The selenide based compounds (*e. g.* WSe_2 or $MoSe_2$), which have a better separation between the A and B peaks/features, could be exploited for the purpose.

3.5 Pump-Probe Fluence Consideration

It is known that a density of photoinduced carriers in the order of 10^{12} cm^{-2} leads to a renormalization of both bandgap and binding energy [90]. As a result, the shift of the optical transitions has been reported as not uniform leading to a red shift of the B exciton of 50 meV, almost two times bigger than the A exciton shift [143]. Different phenomena emerge instead in high carrier regime, where the authors observed a dynamics dominated by the presence of e-h plasma for carrier density of 10^{14} cm^{-2} at the pump pulse in the linear regime [97]. For the above considerations we can consider our case an intermediate regime in between, where a possible stronger red shift of the B exciton could lead to an overlap of both excitonic transitions and the photoinduced absorption located at lower energies. In this regime the A and B peaks merge into one broad peak where A is seen as a shoulder, probably lowered by the strong overlap with the PA at lower energies. (Figure 3.7). Moreover, it has been shown that MoS_2 exhibits a broadband ultrafast saturable absorption (SA) that can be expected to be much larger at its resonant band [144], [145]. At 3.1 eV, where the absorption is around 10% (linear regime), SA has not been reported so far but we could expect to see a nonlinear behavior in correspondence of the C exciton with a decrease of the absorption coefficient. Hence, to give a right estimation of the fluence, we would need the fluence dependent absorption at the pump photon energy which is beyond the scope of this study, since we are interested in the detection of field-induced dissociation.

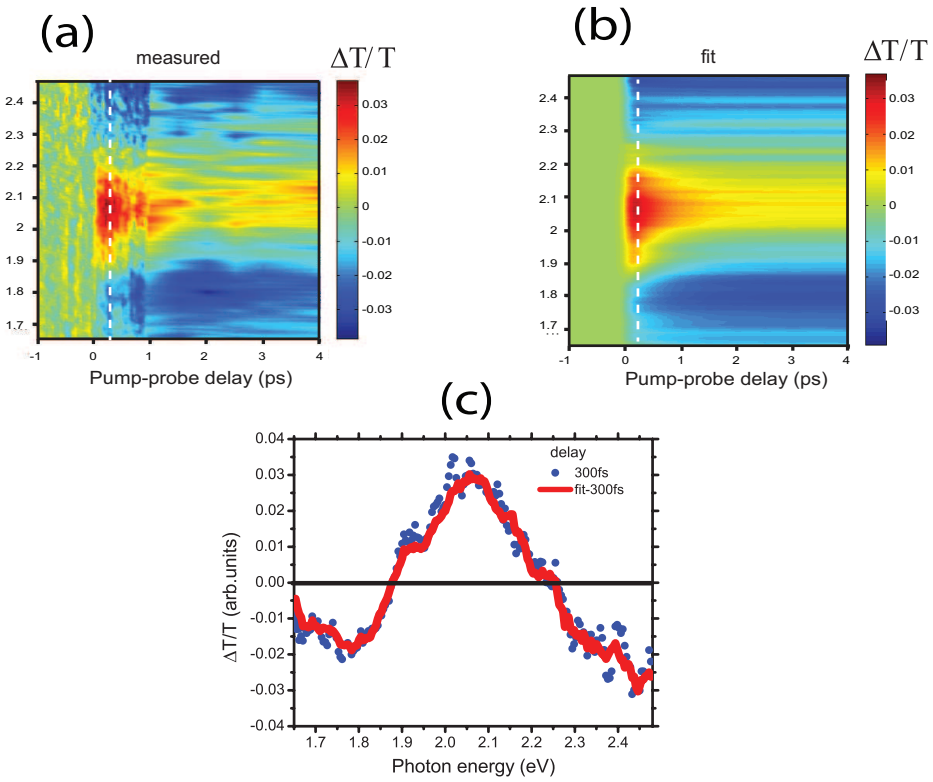


Figure 3.7: a) The transient transmission contour plot as a function of the probe photon energy and pump-probe delay (at 5 V). b) Fit map of (a). c) Pump-probe spectrum at 300 fs delay: real data (blue dots) and fit (red curve).

Chapter 4

Electroabsorption in Monolayer MoS_2

This Chapter is based on a submitted paper, D. Vella *et. al*: *Unconventional Electroabsorption in Monolayer MoS_2*. A preprint version is also available in Ref. [136].

4.1 Unconventional Electroabsorption in Monolayer MoS_2

To translate electrical into optical signals one uses the modulation of either the real or imaginary part of the refractive index of a material by an electric field. Contemporary electroabsorption modulators (EAMs) employ the quantum confined Stark effect (QCSE) [79], [146], [147], the field-induced red-shift and broadening of the strong excitonic absorption resonances characteristic of low-dimensional semiconductor structures. However, compared to the miniaturization currently happening in photonic components, EAMs remain relatively bulky and are becoming an obstacle for further photonic integration.

Two-dimensional materials offer vast opportunities for photonics since they combine easy fabrication and mechanical flexibility with particularly strong light-matter interaction [7], [13]. Semiconducting two-dimensional transition metal dichalcogenides [6], [148] such as MoS_2 support tightly bound excitons [81] with particularly strong absorption cross sections, with a monolayer absorbing about 10% of the incident light (Figure 4.1a). This exceptional light-matter interaction is corroborated by cavity polaritons at room temperature [149], strong optical Stark effect [150], and ultrasensitive phototransistors [20].

Here we measure the transverse EA of monolayer MoS_2 by modulating the gate voltage V_g (with peak-to-peak voltage V_{pp}) in a transparent field effect transistor. We superimpose this modulation on a DC offset voltage, which we can choose so that the transistor is either ON or OFF. In the ON state, we measure electroabsorption together with a spectral contribution due to the modulation of the charge density (charge induced absorption). Charge induced absorption changes the population of electronic levels and thus the strength of different spectral features, such as an enhanced absorption from charges to trions [85], [87], or a decrease of the excitonic absorption features due to phase-space filling (Pauli blocking) [151]. In the OFF state the charge density in the channel remains constant over the modulation period and we measure pure electroabsorption. Most experiments in the present study have been performed with the transistor in the OFF state. Since no charges are moved inside the device in this configuration, the EA response is not limited by the electrical response time of the transistor.

The absorption spectrum of MoS_2 in Figure 4.1a shows the characteristic A and B exciton resonances [6], [7], [13], [20], [81], [148], [149], [150]. The distance between the two main Raman peaks in Figure 4.1b, $\Delta\omega = 19.6$ cm^{-1} confirms the monolayer thickness [10].

The transistor is built in a bottom-gate configuration according to the structure in Ref. [18] (and following the process flow described in Chapter 2), using 30 nm of HfO_2 as gate dielectric and a sapphire slice as the transparent substrate (Figure 4.1c,d). The influence of the transfer process on the monolayer MoS_2 is discussed in Appendix A.1 through a detailed surface analysis. Here we present data from two geometrically identical devices with different turn-on voltages (Figure 4.1d, Figure 4.2b), which we ascribe to adsorption doping [113] since the measurements are carried out in air. We apply a modulated gate voltage (with peak-to-peak voltage V_{pp}) superimposed on a DC offset to the transistor and detect the change ΔT in the transmitted light intensity via a lock-in amplifier locked to the modulation frequency ω. The laser fluence is kept below 150 Wcm^{-2} to avoid photodoping [152]. Transmission is measured using a tuneable laser focussed on a $<$500 nm spot in a confocal microscope, (Figure 4.1e) [153], [154]. We normalise the modulated signal ΔT by the transmitted light intensity T, which directly yields the change ΔA in absorbance:

$$\Delta A = -\frac{\Delta T}{T}. \tag{4.1}$$

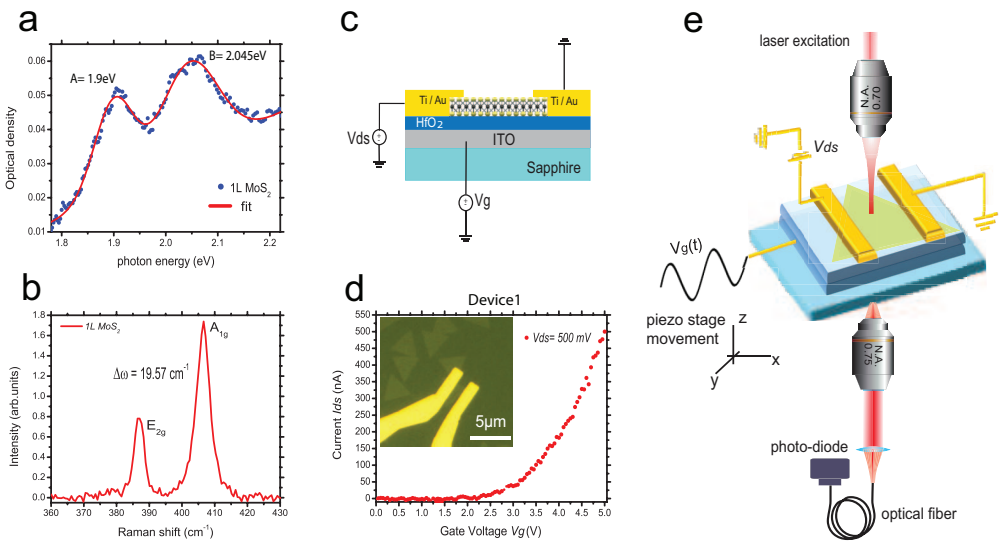


Figure 4.1: a) Extinction spectrum of the MoS_2 monolayer. b) Raman spectrum of the MoS_2 monolayer. c) Schematic of the transistor geometry. d) Dependence of the current I_{ds} of the gate voltage V_{g} for Device 1. Inset shows an optical micrograph of the device. e) Schematics of the extinction and electroabsorption measurements using a tuneable laser in a confocal microscope.

4.2 Experimental Resuls

The EA spectrum of monolayer MoS_2 for transverse field modulation consists of alternating positive and negative absorption changes (See Figure 4.2a,b,c), three peaks of increased absorption and two of decreased absorption. The two peaks of decreased absorption are stronger than the other three and peak at the same wavelengths as the A and B features in the absorption spectrum. The shape and magnitude of the EA signal is independent of the DC component of the gate voltage when the transistor is in the OFF state ($V_{\mathrm{g}} < 2$ V

for device 1, $V_g < 0.5$ V for device 2). When the transistor is ON and charges are injected, the signal is weaker and slightly changes shape. The injected charges may partly screen the field and weaken the EA signal (see the Section 4.4 for an estimate of the screening). Moreover, in this case the modulated field also modulates the charge concentration in the channel, which adds to ΔA (charge induced absorption) [85], [87], [151].

The most common features of EA are (i) field-induced changes in the peak positions of the A spectrum (red- or blue-shifts), (ii) field-induced changes in the peak width of A (usually broadening), and (iii) in some cases also changes in the area under the A curve in a certain spectral window (transfer of oscillator strength between different electronic transitions) [79], [146]. In the ΔA spectra these features appear as distinctive shapes related to the respective absorbance peaks: (i) as a first derivative of the absorbance for shifts of A: $\Delta A \propto dA/dE$, (ii) as a second derivative for changes in the width of an A peak: $\Delta A \propto d^2A/dE^2$, and (iii) as the same lineshape as the absorbance for transfer of oscillator strength: $\Delta A \propto A$. We fitted the absorption spectrum in Figure 4.1a using two Gaussian peaks and a generic exponential function to account for the background from various scattering mechanisms. To identify the main contributions to the EA spectra, we used first and second derivatives of these Gaussians independently to fit the EA spectra, as shown in Figure 4.2d,e. Second derivatives dominate the ΔA spectrum, together with a first derivative contribution. Hence the main effect of the electric field on the absorbance A is broadening (about 6% for the A peak of device 1, 15% for device 2), accompanied by a slight red shift. Transfer of oscillator strength is not needed to fit the EA spectra. The joint action of broadening and red shift slightly slants the two negative peaks of the EA spectrum towards higher energies compared to the absorption resonances and diminishes the middle peak due to the overlap of positive and negative signal components.

For different modulation voltages V_{pp}, the EA signal retains its shape and increases linearly in magnitude (Figure 4.2c,f). This means that in particular the broadening of the absorbance increases linearly with the modulated field, an unconventional behaviour that has not been reported in other materials so far. On the other hand, shifts of the absorbance with linear field dependence are common and indicate built-in fields or permanent dipole moments [155]. In engineered two-dimensional semiconductor structures (quantum wells or multiple quantum wells), the QCSE yields a red shift proportional to the square of the applied electric field, accompanied by a broadening of the excitonic resonances. The broadening is ascribed to an increased homogeneous linewidth due to field-induced exciton dissociation (charge transfer into the " walls " of the quantum well), and has a highly non-linear field dependence. Hence our results disagree with the conventional QCSE. Other possible origins of the signal, such as heating or strain-induced shifts from piezoelectricity are also ruled out from their field dependence in a detailed discussion in Section 4.3.1.

4.3 Origin of the Electroabsorption Signal

To explain the unconventional linear field dependence of the broadening, we take a closer look at the linewidth of the absorption resonances. Since MoS_2 from any synthesis method is doped [18], [30], the absorption peak A consists of at least two overlapping electronic resonances, A^0 from the neutral ground state to a neutral exciton state, and A^- from a charged ground state to a charged exciton state (trion) [85]. Similarly, the broader B peak should also be composed of two peaks B^0 and B^-. Although B trions have not been studied in detail yet, they play a role in the transient absorption spectra observed in femtosecond pump-probe experiments [96]. Since positive and negative trions appear at almost the same spectral position [156], the following considerations can also be made for p-doping. The distance between A^0 and A^- changes almost linearly with V_g over a wide range of gate

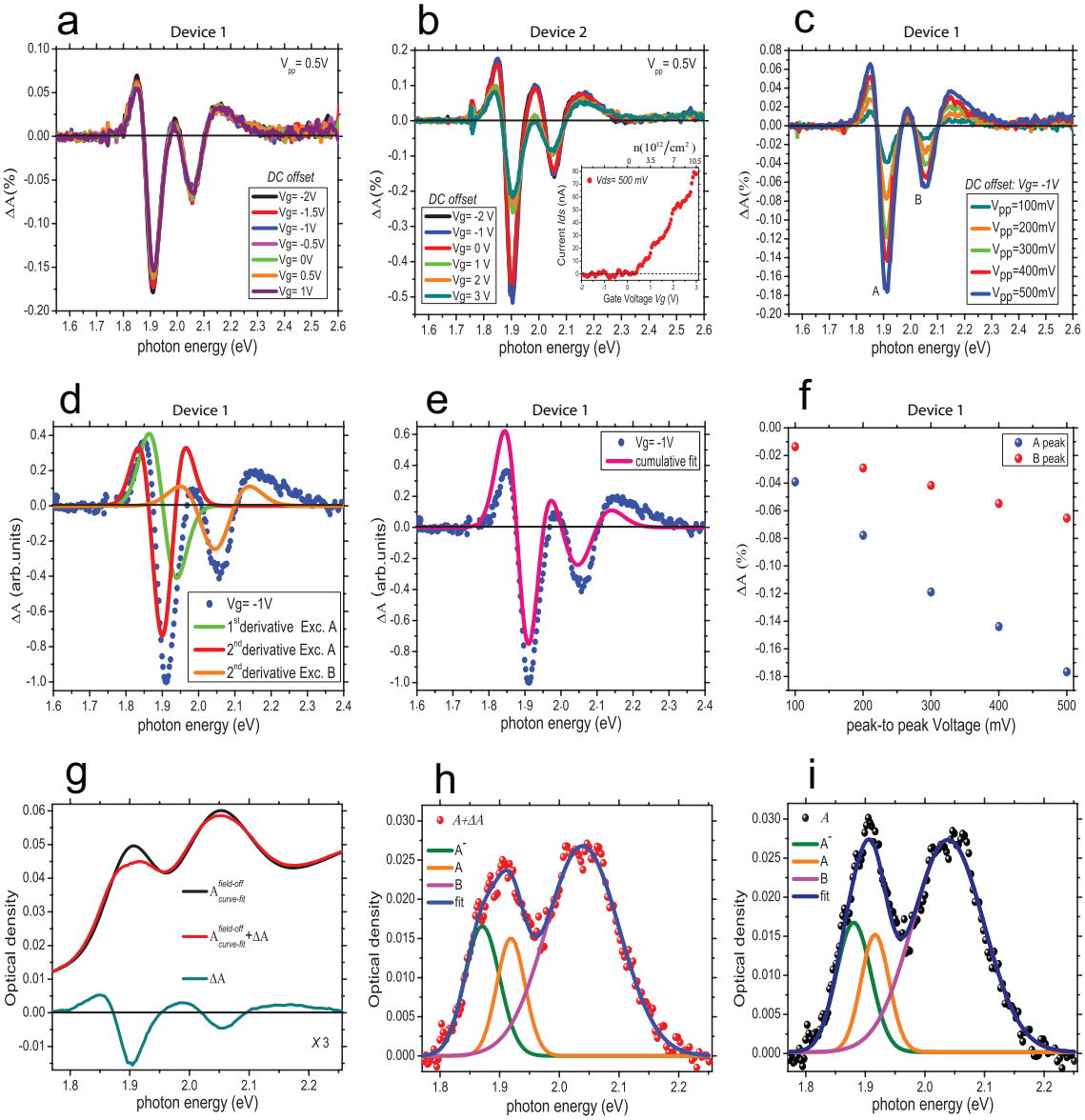


Figure 4.2: a,b) Electroabsorption spectra of devices 1 and 2 for different gate voltage DC offsets. Inset in b) shows the gate voltage dependence of the current in device 2. c) Electroabsorption spectra of device 1 for different peak-to-peak voltage modulation amplitude V_{pp}. d,e) normalised electroabsorption spectrum (dotted) of device 1 and first and second derivatives of the absorption peaks used to fit the spectra (individual contributions in d), cumulative fit in e). f) A and B peak amplitudes from c) as a function of V_{pp}. g) Fit of the extinction spectrum (black), electroabsorption spectrum (dark cyan) and sum of the two (red) give the extinction spectrum at a gate voltage $V_{\mathrm{g}} = V_{\mathrm{pp}}$. h,i) Extinction spectra with and without field fitted to three Gaussian curves.

voltages comprising both the ON and OFF states[87], [156]. This shift of both features has been tentatively ascribed to Stark effect [156] or to a renormalization of both the band gap and the exciton (or trion) binding energy [87]. The latter explanation is applicable only for the ON state of the transistor, where the gate voltage actually modulates the charge density. Here, in the OFF state the charge density in the MoS_2 channel stays

constant; hence we continue to discuss our results without assuming charge-density related renormalizations.

By adding the field-induced absorbance change ΔA to the absorbance A without field in Figure 4.2g (to reduce noise, we used the fit for A rather than the original data) we obtain the shape of the absorbance spectrum in the presence of an electric field corresponding to a $V_g = V_{pp} = 0.5$ V. Clearly, the A peak is lowered and broadened and its composition by two peaks is now more clearly visible. A similar but smaller effect is also seen for peak B, which should also be composed of two resonances B^0 and B^-. However, peak B is too wide to yield accurate parameters for two component peaks; hence we do not explore its composition further. In Figure 4.2h,i we show fits of A and $A + \Delta A$ using two Gaussians for peak A, with height and width unchanged between both cases, only different positions. This fit embodies a model where the A^0 and A^- resonances maintain their width and oscillator strength, but change their positions as a consequence of the applied electric field. The constant height of both peaks means that no oscillator strength is transferred and, more importantly, no charge is injected into or extracted from the channel. A gate voltage of $V_g = 0.5$ V increases the distance between the A^0 and A^- peaks from 36 to 48 meV, resulting in both a broadening and lowering of the A peak as a whole. Additionally, the peak shifts slightly to the red since the red shift of the A^- peak is stronger (-9 meV) than the blue shift of the A^0 peak (+3 meV). While the composite A peak with 36 meV between the A^0 and A^- peaks (Figure 4.2i) still looks very similar to a Gaussian, at 48 meV it does not (Figure 4.2h), which explains why the fit with first and second derivatives of a Gaussian deviates from the real data (Figure 4.2e). Note also that, to merge into what appears as one B peak, its constituent peaks B^- and B^0 must be broader than A^0 and A^-. Hence, if B^- and B^0 shift by a similar amount as A^0 and A^-, their effect on the shape of B is weaker, which explains the lower EA signal of the B peak. In conclusion, in the regime where we do not modulate the charge density, the overall unconventional change of shape of the absorbance spectrum with a linear dependence on the transverse electric field strength originates from linear shifts of the strongly overlapping exciton and trion peaks. A detailed description of the accuracy of the used fits is given in Appendix A.2.

4.3.1 Discussion of Possible Origins of the Electroabsorption Signal

In monolayer MoS_2 we observed an electroabsorption (EA) signal that is dominated by a broadening of the main absorption features, accompanied by a slight red shift. Spectral shifts of excitonic absorption resonances can be caused directly by the electric field via (quantum confined) Stark shifts of the levels involved [79], [146], [155] in the electronic transition, or indirectly via mechanical strain [157] caused by piezoelectricity [158], sample heating [159], or via changes in population (via renormalization of the bandgap [97] and the exciton binding energy [87] or via the Burstein-Moss effect [134]). Since our region of interest is the OFF state of the transistor, we can exclude contributions that depend on charge density (*i. e.* bandgap renormalization and Burstein-Moss), or the dissipation of energy (*i. e.* heating).

Linewidth broadening can arise either from an increase of the homogeneous or the inhomogeneous linewidth. The homogeneous linewidth is given by the excited state lifetime and its dephasing time. An electric field can reduce the lifetime via exciton dissociation, and the dephasing time via induced strain that through the deformation potential leads to changes in the energy and the scattering [160] of the exciton quasiparticle. The inhomogeneous linewidth is given by the distribution of resonance energies due to any of the above mentioned reasons, *e. g.* a nonhomogeneous distribution of the electric field or the mechanical strain or the charge density over the sample. Importantly, even if the local energy shift is linear in the local electric field, the broadening will be quadratic [161]. In modulation

spectroscopy, the signal is detected via a lock-in amplifier, which can be locked either to the modulation frequency ω or one of its harmonics (most commonly 2ω). Here, we do not find any signal at 2ω. This readily excludes all possible signal origins that are quadratic in the electric field (or at least have a sizable quadratic component when expanded into a polynomial), most notably the quadratic Stark effect, quantum confined Stark effect, and all possible contributions to the inhomogeneous broadening.

A strong signal component at 2ω is also expected for effects that increase with the magnitude of the applied field, *i. e.* that arise with the same sign both for the positive and negative half-wave of the modulated field. Hence the absence of a 2ω signal excludes exciton dissociation, which should happen for both field polarities. MoS_2 does not show any transverse piezoelectricity; any field-induced shortening of the distance c_1 between the lower S plane and the Mo plane is offset by a lengthening of the distance c_2 between the upper S plane and the Mo plane, and *vice versa*. Hence also the effect of the field on the dephasing via the deformation potential should be the same for both field polarities. Hence we have excluded both homogeneous and inhomogenous broadening and confirmed that the observed broadening of the composite peaks is actually a shift in opposite directions of two constituent peaks. As discussed in the previous paragraphs, field-induced strain should result in opposite changes of the lattice constants c_1 and c_2, and hence in a splitting or broadening of the exciton and trion peaks rather than a shift. By exclusion, we have linear Stark effect as the only remaining assignment.

4.4 Electrostatic Consideration

The gate voltage V_g causes a transverse electric field in the MoS_2 monolayer

$$F = \frac{V_\mathrm{g}}{d_M + \frac{\varepsilon_M}{\varepsilon_H} \cdot d_H}, \tag{4.2}$$

with the indices M and H indicating the thickness d and dielectric constant ε of MoS_2 (ε_M = 7) [162] and HfO_2, (ε_H = 19) [115], respectively. A gate voltage V_g = 0.5 V yields a field F = 400 kVcm^{-1}. Our field modulation corresponds to a voltage difference of 20 V in the device of Ref. [87], giving a comparable shift of several meV for both the A^0 and the A^- peak. A Stark shift has been recently reported for the low-temperature photoluminescence of a MoS_2 monolayer sandwiched between two dielectrics [163]. The A peak position follows a hysteretic curve, which the authors ascribe to a joint effect of Stark effect and charge transfer with the top dielectric (Al_2O_3). Along most of their curve, our field modulation of 400 kVcm^{-1} would give a shift of a few meV in their device, consistent with our results. Please note that also in their data the linewidth changes, although they discuss only the peak shift.

The transverse field strength inside the MoS_2 layer may be inhomogeneous and deviate from Equations (4.2) due to screening by charges from doping (during the synthesis or due to adsorption) and, for the orange, green, and cyan curves of Figure 4.2b, also from injection into the device. In the following, we make three assessments of the possible screening of the applied electric field by the charges present from doping: (i) estimating the electric field of a plane of the same surface charge density, (ii) estimating the Debye screening length, and (iii) discussing the effect of additional charges injected by switching the transistor to the ON state. The similar peak heights for the exciton and trion peaks in Figure 4.2h,i suggest a doping level [87] of a few 10^{12} electrons cm^{-2}. A plane of surface charge density $\sigma = 10^{12}$ electrons cm^{-2} generates an electric field of

$$F = \frac{\sigma e}{2\varepsilon_r \varepsilon_0}, \tag{4.3}$$

F = 130 kVcm^{-1}. Hence, to completely screen 400 kVcm^{-1}, all the electrons in the conduction band would have to form a surface charge at or even below the lower Sulphur plane of MoS_2. Such localization of electrons contradicts the more delocalized nature of the conduction band. Therefore, we conclude that the electrons present from doping may partially, but not completely, screen the applied electric field. A further assessment of the effectiveness of screening is provided by an estimate of the Debye screening length λ_D:

$$\lambda_D = \sqrt{\frac{\varepsilon_r \varepsilon_0 \kappa_b T}{\rho e^2}}. \tag{4.4}$$

where κ_b is the Boltzmann constant, T is the temperature of the system (room temperature), and ρ is the electron density. For $\rho = 10^{12}$ cm^{-2} we obtain $\lambda_D = 0.3$ nm, about half the thickness of the MoS2 layer. If some of these charges are trapped, which is likely, they cannot contribute to the screening and λ_D is even longer [164]. Again, this estimate suggests that partial screening is possible, while complete screening is not. This assessment is further corroborated by the fact that injection of additional charges, with a density of the same order of magnitude as those from doping, results in a reduction but not in complete disappearance of the EA signal (Figure 4.2b), again consistent with partial screening of the applied electric field. Please note that all production methods of MoS_2 (in particular also geological processes yielding the mineral molybdenite) customarily result in doped samples. Hence, published values for ε_r of MoS_2 already account for partial screening from a certain level of doping. A linear shift in the applied field F is consistent with Stark effect originating from a permanent dipole moment or an induced dipole from a built-in electric field:

$$\Delta E = \overrightarrow{\Delta p} \cdot \vec{F}, \tag{4.5}$$

with Δp being the difference in the dipole moment of the exciton (trion) and the neutral (charged) ground state. The shifts of a few meV correspond to differences in dipole moments between excited and ground states of a few Debye. Note that this is only a rough estimate obtained from the fits in Figure 4.2h,i. The MoS_2 monolayer itself should have no out-of-plane dipole moment for symmetry reasons, as has been confirmed by momentum-resolved photoluminescence spectroscopy [165]. Resolving the contradiction between the purely in-plane exciton dipole and the recently observed transverse Stark effect is beyond the scope of the present thesis [163]. We can, however, briefly discuss possible origins of either an out-of-plane dipole moment or a different mechanism for the field-induced spectral shift. As discussed above, charges present in the doped MoS_2 monolayer, can partially screen the transverse external field. The centre of the charge density is displaced from the Mo mirror plane as a function of the external field. This may affect both the bandgap and the exciton and trion binding energies. In particular, if the latter two change by different amounts, this results in a field-induced change in the distance between the exciton and trion peaks.

On the other hand, the spectral properties of MoS_2 are sensitive to the dielectric environment [62], [166]. In the momentum-resolved photoluminescence study MoS_2 was sandwiched between microscope oil and quartz, both dielectrics with relatively low ε_r. In our device the asymmetry is much larger (HfO_2 on one side of the monolayer, metal electrodes and air on the other), which may induce more significant transverse dipoles. In fact, EA spectroscopy is routinely used to characterize interface dipoles in heterostructure devices such as organic solar cells [167].

The dipole moment induced by the device structure can be manipulated by adsorbed molecules, since our experiments have been carried out in air. EA spectroscopy has been

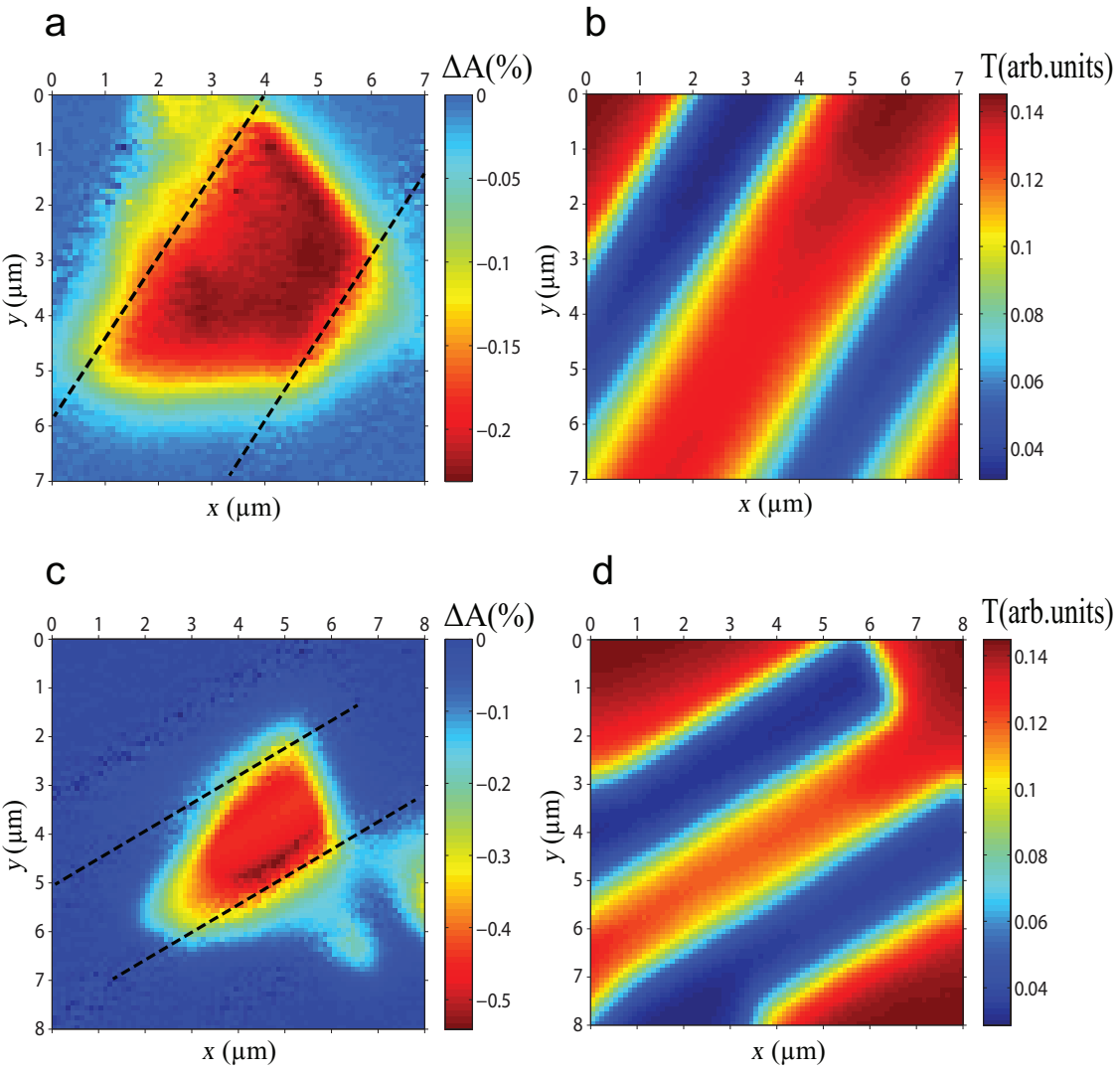


Figure 4.3: a,b) Electroabsorption and transmission maps of device 1. c,d) Electroabsorption and transmission maps of device 2. All measurements were performed at 650 nm, electroabsorption with a DC offset of -1 V and a modulated voltage $V_{\mathrm{pp}} = 0.5$ V.

used to characterize the interface dipole between semiconductor nanocrystals and adsorbed dye molecules [168]. We expect that the present thesis will inspire similar work to study the effect of adsorbed molecules on MoS_2, whose effect on the electronic structure is hardly explored. Adsorbed molecules can also dope the channel [113] and thus change the ratio between the A^0 and A^- peaks. Simulations in Section 4.6 show that for identical peak shifts the EA signal is strongest if A^- dominates the absorption spectrum, since it shifts more strongly. Device 1 (Figure 4.1d) is p doped, as confirmed by the higher turn-on voltage. This lowers the A^- peak or even replaces it by an A^+ peak. From the above considerations, a lower A^- peak means a lower EA signal. An A^+ peak has never been reported in MoS_2, however, in WSe_2, compared to A^- it shows a smaller shift with field [132], in the opposite direction, which again lowers the EA. In Figure 4.3 we show transmission and EA maps of both devices at the strongest EA peak (1.9 eV). Although we average over a spot size

of <500 nm, we find that the signal between the two electrodes (a lower signal is also seen below the electrodes, probably due to multiple reflections in the substrate) varies between 0.15 % and 0.22 % for Device 1 and 0.40 % and 0.52 % for Device 2. The signal variation across the maps in Figure 4.3 does not follow the device geometry; hence, it must originate from some other heterogeneity, such as adsorbed molecules of varying density or charge puddles from doping. Hence EA microscopy, possibly pushed towards even higher resolution via near field scanning microscopy or stimulated emission depletion, may evolve into a tool for characterizing molecular adsorption and the micro-and nanostructure of doping in 2D materials.

4.5 Assessing the Use in an Electroabsorption Modulator

Important performance figures for EAMs/EOMs are the insertion loss IL, the modulation depth MD, the device footprint A_d, and the switching energy per bit E_b. For typical applications an MD = 7 dB is required, while IL is typically around 1-2 dB. The device footprint of commercial devices typically exceeds 10^4 μm^2, but experimental devices with footprints ranging from 8 to 25 μm^2 have been realized [169], [170]. The switching energy per bit in state-of-the-art data centers is currently a few pJbit^{-1}. However, to replace the existing electrical interconnect technology, $E_b < 1$ fJ/bit is considered as the requirement for disruptive technology.

In the transmission geometry, as used for the experiments shown here, the IL is equal to the absorbance in the presence of the electric field and MD and IL relate straightforwardly to the absorbance A without field:

$$IL + MD = A. \tag{4.6}$$

Hence, increasing the transmission in the presence of the electric field improves both performance figures together: it decreases IL and increases MD. We have shown switching from approximately 89% transmission to 89.5% transmission, corresponding to an insertion loss of 0.48 dB and a modulation depth of 0.02 dB. For comparison, a single layer of graphene, with the change in absorption caused by changes in the occupation of electronic levels rather than Stark effect, has negligible IL and an intrinsic upper limit of 0.10 dB for MD (2.3% transmission modulation [171]). To improve the performance of the 2d semiconductor device, the transmission in the presence of the electric field could be increased either if the A^0 and A^- peaks shifted more strongly (*e. g.* by using a material with larger intrinsic shift or a stronger modulated field), or if they were narrower with all other parameters equal or similar (see Section 4.6). Narrower peaks can be achieved either by cooling the device [159], [172] or by using other 2D compounds with narrower resonances, such as $MoSe_2$ [173]. The intrinsic performance limit would be a situation where in the presence of the electric field the A^0 and A^- peaks are completely separated, with a dip of almost zero absorbance in between them. In this limit, IL is negligible and MD of the monolayer is almost 0.5 dB, clearly exceeding the performance of graphene.

We assess attainable performance figures of the present device in two geometries: directly in transmission, as in the experiments shown above, and cladding a silicon waveguide to modulate the evanescent wave, as has been realized with graphene [169], [174]. The graphene devices in the cladding configuration have IL = 3 dB, MD = 0.1 dBμm^{-1}, and A_d = 25 μm^2, which are among the best realized to date. As outlined above, MoS_2 performs similarly to graphene 4-5 times worse in the case of our non-optimised devices, 4-5 times better than graphene might be attainable. Hence, in this configuration, we can expect similar performance figures to the graphene devices.

An even more compact EAM can be envisaged by using directly the transmission geometry in which we performed our experiments. The device could be built to an overall thickness of 100 nm, reducing the device footprint to $< 1\ \mu m^2$. Assuming we can realistically attain MD > 0.2 dB for a monolayer, to achieve a viable MD of 7 dB, we would need a device with either 20-50 layers of MoS_2, or a multipass geometry (*e. g.* a monolayer inside a Fabry-Perot interferometer), or an even further increase of the light-matter interaction via the Purcell effect [175] or metallic nanostructures [176]. None of these strategies would increase the device footprint by more than a factor of 2. However, for a device consisting of 50 layers of MoS_2 in order to work at the same modulated electric field, V_{pp} would have to be increased to 1.8 V. The switching energy would then be $E_b = 1/2\ C\ V_{pp}^2 = 15$ fJ, for a device of C = 14 fF (assuming 30 nm HfO_2, 30 nm of MoS_2, and a device cross section of 3×3 μm, as used here), while for the monolayer device $V_{pp} = 0.5$ V and C = 50 fF, yielding $E_b = 6$ fJ. Reducing the device cross section by one order of magnitude to the size of the focussed light spot (sub-μm) could proportionally reduce the device capacity and hence bring the switching energy to the sub-fJbit^{-1} regime. In conclusion, we have shown an unconventional electroabsorption effect in monolayer MoS_2 and ascribed it to linear field-induced shifts of the exciton and trion resonance peaks in opposite directions. The strength of the effect suggests that 2d semiconductors are excellent materials for EAMs. Monolayer MoS_2 shows its strongest EA signal at 1.9 eV (650 nm). However, there is a vast choice of 2D materials [177], [178] with bandgaps covering the whole range from 0 to beyond 5 eV, including the main telecom wavelengths (850-1550 nm). Compared to graphene, we envisage a possibly even shorter device with much lower power consumption due to the low off current [18]. Additionally, since the working principle is not based on changes in the population of levels, there is no excited state lifetime limit to the response time [169], [174]. Such a device could be extremely compact and enable on-chip optical communication.

4.6 Possible Strategies to Increase the EA Signal

In the following, we simulate EA spectra for different relative strengths of the A^- and A^0 peaks, as well as for A^- and A^0 peaks with reduced width. For simplicity, we disregard the B peak and assume that A^- and A^0 have the same FWHM of 63 meV (in Figure 4.2g,h,i A^- has 69 meV and A^0 has 56 meV). In all cases, A^- shifts by -9 meV and A^0 by +3 meV upon application of an electric field. In Figure 4.4a,b,c we simulate the EA spectra assuming that the A^- peak bears 25, 50, and 75 % of the total oscillator strength. This results in ΔA signals with maximum negative value of -14 %, -19 %, and -28 % of the absorbance at the same wavelength, respectively. Hence one strategy to increase the EA is to increase the n doping of MoS_2, since the A^- peak shifts three times as much as A^0. Figure 4.4d shows the EA signal for 50% oscillator strength on each of the two peaks, but with both peaks having their FWHM reduced by 20%. This gives a maximum negative ΔA of -31 % of the absorption at the same wavelength. Hence using a material with narrower A^- and A^0 peaks compared to their distance, or reducing their width by cooling the sample are two additional strategies to increase the EA signal. Ideally, the absorbance could be modulated between its peak value and almost 0.

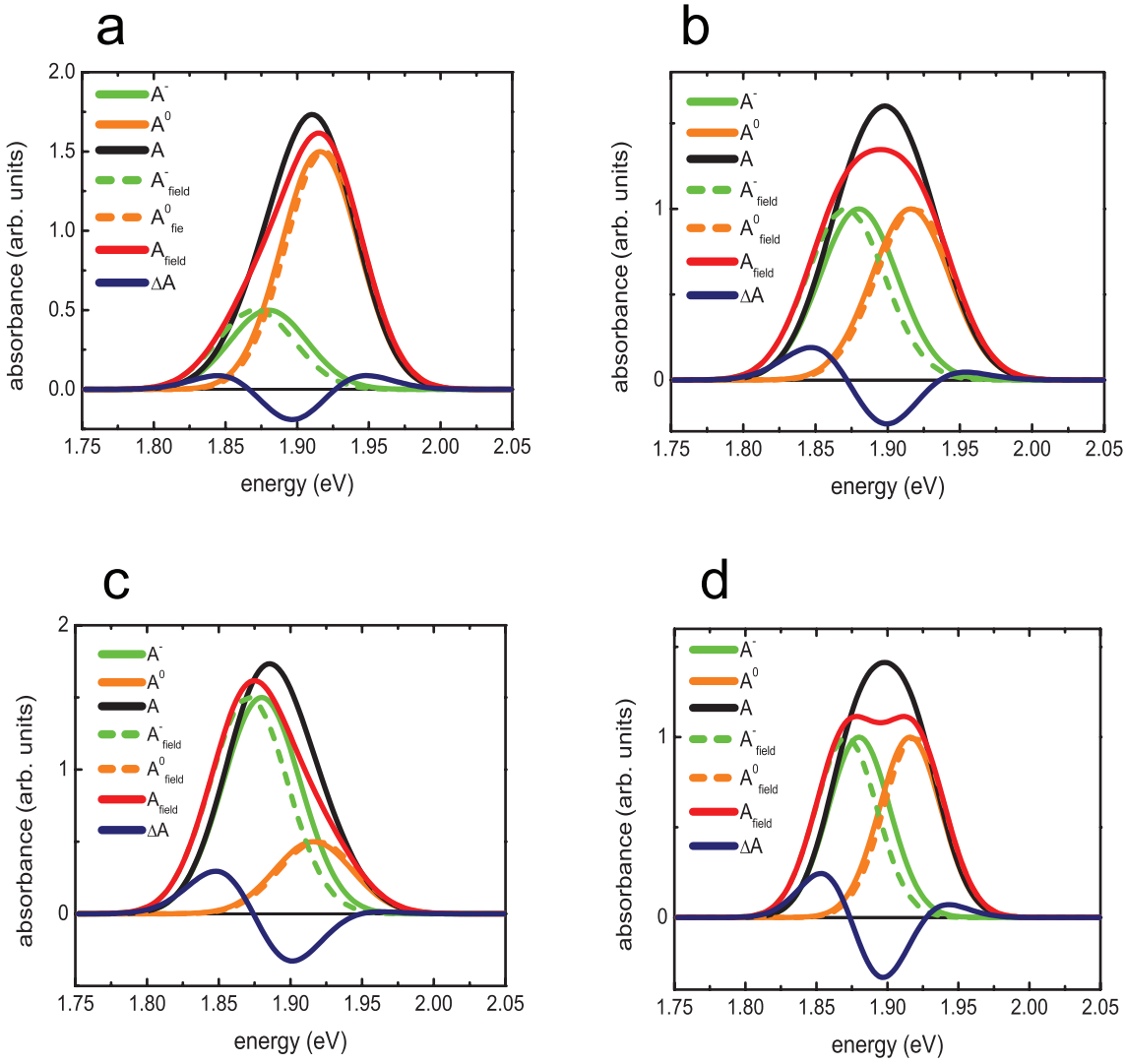


Figure 4.4: Absorption spectra with and without electric field and EA spectrum for A^- and A^0 peaks of different heights and widths (see text).

Chapter 5

Femtosecond Spectroscopy on MoS_2 Flakes from Liquid Exfoliation: Surfactant Independent Exciton Dynamics

This Chapter is based on a published paper, D. Vella *et. al* [99]: *Femtosecond spectroscopy on MoS_2 flakes from liquid exfoliation: surfactant independent exciton dynamics.*

5.1 Introduction to the Topic

In the last five years, most of the know-how acquired by the carbon community and culminating in the discovery and exploitation of graphene [3] has been transferred to isolate and engineer transition metal dichalcogenide (TMDC) layered materials. Semiconducting TMDCs, such as MoS_2, WS_2, $MoSe_2$, and WSe_2, can also be exfoliated into two-dimensional (2-D) layers of single unit cell thickness, suitable for logic devices and optoelectronics applications [6], [18], [32]. A peculiarity of the semiconducting TMDCs is the crossover from indirect to direct gap semiconductor when going from bulk or few-layer material to monolayers [21]. This is a result of the gradual change of the band structure as a function of the number of layers due to quantum confinement [22].

Liquid exfoliation has been proven to produce stable dispersions of flakes of 2-D TMDCs via a procedure that involves ultrasonication and centrifugation. However, processing nanomaterials in liquid dispersion can crucially alter their optical response and their electronic properties [179]. For example, during continuous wave excitation of single wall carbon nanotubes (SWNTs) covered with sodium cholate, chemisorption of oxygen leads to hole doping and photoluminescence quenching. In low pH solution, protonation of the oxygen absorbed on an SWNT with a sodium dodecyl sulfate shell bleaches the optical absorption and consequently quenches the luminescence by Auger recombination [180], [181], [182]. Moreover, it localizes electrons on the SWNT and increases the number of holes in the valence band (VB) [183]. The surfactant surrounding SWNT can induce photoluminescence blinking via trapping photoexcited charges followed by a slow recombination. This process also changes the emission spectrum via Stark effect [184], [185]. Femtosecond pump-probe spectroscopy represents a versatile technique to study the electron dynamics in semiconducting nanomaterials. It has elucidated, for instance, the dynamics of charge carriers, excitons, and phonons [91], [186] or the Stark effect induced by photogenerated and trapped charge carriers [187]. Here, we use femtosecond pump-probe spectroscopy to

study few layer MoS_2 from liquid exfoliation in water and sodium cholate [33] with different amounts of adsorbed surfactant controlled by a multistep washing protocol. We exploit the sensitivity of the pump-probe signal to the change of the electronic excited state population [118] in order to investigate the effect of the surfactant on the carrier and exciton dynamics of MoS_2. For different amounts of surfactant, we obtain the same shape and relaxation behavior of the pump-probe spectra. This work demonstrates the optical stability of MoS_2 against surfactant adsorption, which sets it apart from other semiconducting nanomaterials.

5.2 Sample Preparation

An initial solution of 4.5 g sodium cholate and 15 g of MoS_2 in powder form (Sigma Aldrich) dissolved in 1 l of deionized (DI) water was ultrasonicated for 100 h, using an Elmasonic P ultrasonic bath at 37 kHz and maximum power. This solution, which contains the flakes of MoS_2, was used as a starting point for producing all the samples [32].

In order to obtain films of few-layer MoS_2 flakes with high surfactant content (SC), 10 ml of ethanol was added to 10 ml of the main solution, which was then spray-deposited on a quartz substrate (kept at 150 °C). In parallel, different washing steps have been done to produce samples with medium and low SC.

MoS_2 with medium SC was obtained by centrifugation of a part of the initial solution in a Cole Parmer Power Spin BX centrifuge for 60 min at 11 Krpm, followed by the addition of clean DI water and ultrasonication in a bath. This procedure was repeated three times to remove a part of the surfactant from the solution and from the MoS_2 surface. At a later stage, ethanol was added as described above, and the mixture was sprayed on quartz. Figure 5.1a shows a transmission electron microscope image of a typical few-layer MoS_2 flake obtained by this process. To further reduce the concentration of sodium cholate on the surface of MoS_2, we introduced an additional step in the procedure for the medium SC samples: after each centrifugation, the solution was washed with DI water and HCl (0.1 ml of 1M HCl per 50 ml of MoS_2 dispersion). HCl reacts with sodium cholate and forms sodium chloride and cholic acid, which is soluble in ethanol. This step is expected to remove most of the sodium cholate from the flake surface. Such obtained low SC dispersion is again deposited on a quartz substrate.

As a reference sample, we used MoS_2 obtained in crystalline form (Wolfram Camp Mining Ltd.), expanded in hydrazine [188] and exfoliated, without surfactant, in the organic solvent N-methyl-2-pyrrolidone by ultrasonication. The films were deposited on quartz substrates by a Langmuir-Blodgett process [189].

5.3 Results and Discussion

The normalized absorption spectra in Figure 5.1b show the characteristic exciton resonances A to D at 1.8, 2.0, 2.8, and 3.0 eV. The resonances A and B are ascribed to excitons associated with the direct gap transition at the K point [63], [190]. The splitting originates primarily from the splitting of the VB due to spin-orbit coupling. The C exciton is ascribed either to a transition from a band below the VB toward the conduction band (CB) or to a transition from the VB into a nested region [128] of the CB. The D exciton is commonly ascribed to impurities [63].

Recently, it has been shown that for surfactant dispersions of MoS_2, the characteristics of the absorption spectrum provide a metric for the average flake size and thickness [35]. Since it has been formally proven only for aqueous dispersion, we do not extract any quantitative characterization from our absorption spectra; however, the general trends

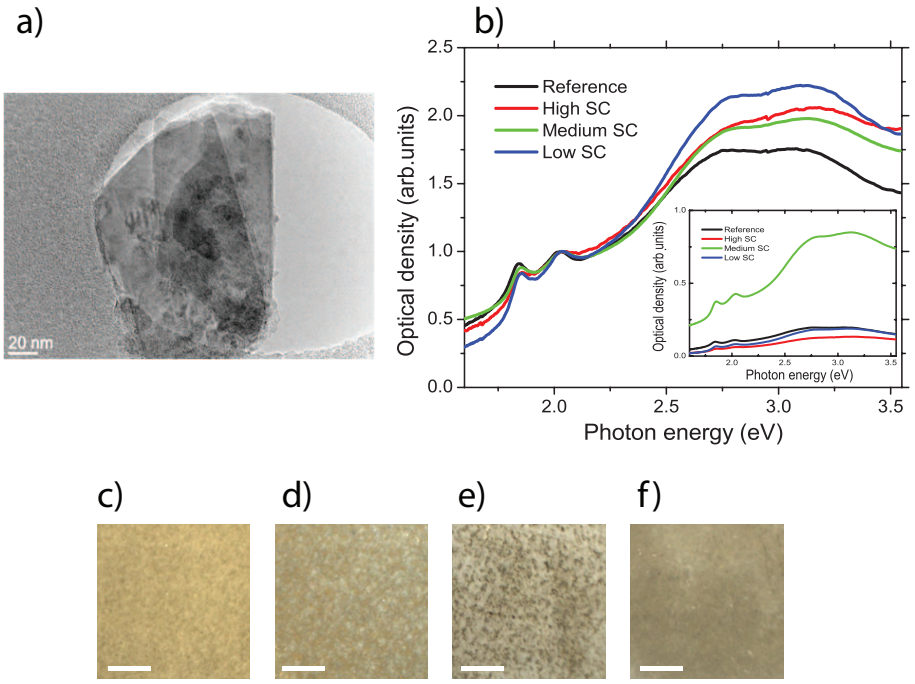


Figure 5.1: a) Transmission electron microscope image of a few layers of MoS_2 from liquid exfoliation in deionized water and sodium cholate. b) Absorption spectra of few-layer MoS_2 ensembles from liquid exfoliation with different surfactant content (SC) and a reference sample exfoliated via a surfactant-free process normalized to the B-exciton resonance. Inset shows actual optical density. Bright-field images from an optical microscope of MoS_2 deposited on a quartz substrate: c) low SC, d) medium SC, e) high SC, and f) reference. Scale bar: 1 mm.

should be valid also for dried films. Specifically, the ratio between the B exciton peak and the absorption at 3.6 eV is a measure of the typical flake size, and the position of the A exciton peak is a measure of the typical flake thickness (number of layers). The samples differ very little in both respects, the most significant difference being that the reference sample, probably due to the different exfoliation protocol, seems to consist of somewhat smaller flakes. Repeated washing, on the other hand, does not appreciably affect the flake size and thickness distribution.

To evaluate the homogeneity of the films on the relevant scale of 150 microns (the spot size used for the pump-probe experiment), we show optical images of the deposited MoS_2 (Figure 5.1c,d,e,f). The darker hue of green seen for the medium SC film, matched by a higher optical density and stronger Raman and pump-probe signals (see below), is due to a higher film thickness. For the used high concentration, our simple spraying technique gives little control over the spraying speed and hence the film thickness. A significant inhomogeneity is seen only for the high SC sample. The high surfactant concentration may favor lateral aggregation of flakes or have an influence on the drying dynamics of the film. However, the apparent islands and voids are small enough to mostly average out over the spot size of the pump-probe experiment.

To find out whether the inhomogeneity in the film thickness is also related to an inhomogeneity in the flake characteristics, we measured Raman spectra (depicted in Figure 5.2) on each sample on four randomly selected spots with a distance of several millimeters and a spot size of 20 microns, much smaller than the characteristic length scale of the inhomogeneity. The distance between the peaks E^1_{2g} (in-plane mode) and A_{1g} (out-of-plane mode)

is a robust measure of the flake thickness [191]. We obtain $\Delta\omega = 24.5$ cm^{-1}, corresponding to an average flake thickness of four layers for the high SC sample, and $\Delta\omega = 25$ cm^{-1}, corresponding to five or more layers for all the others.

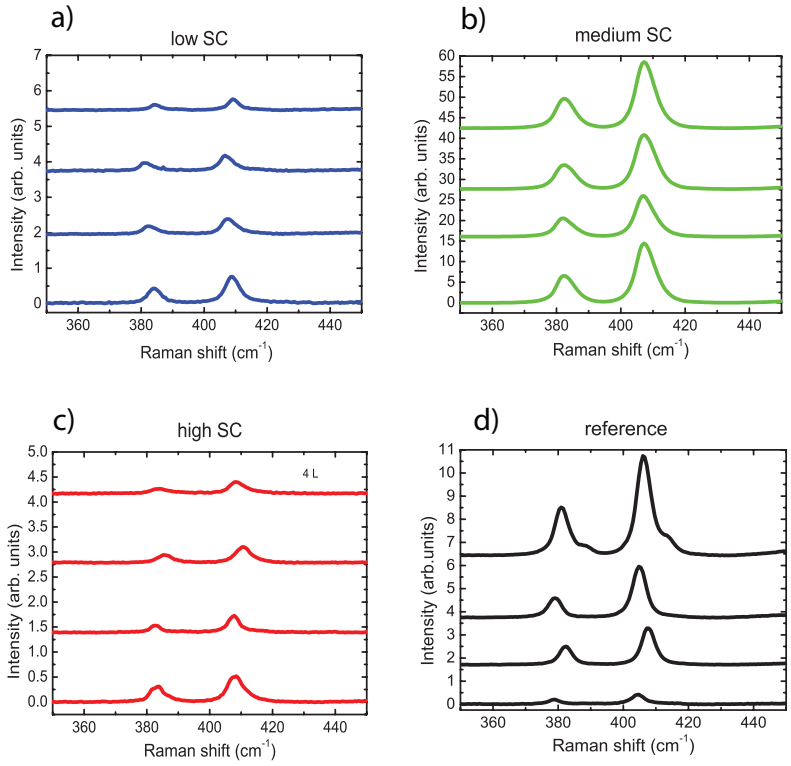


Figure 5.2: Raman spectra for excitation at 488 nm in four different points on the sample: a) low SC, b) medium SC, c) high SC, and d) reference.

Given the similar electronic structure of the flakes within the same film, we can use the Raman intensity as an indication of the amount of material present [57]. The thicker sample (medium SC) shows a similar Raman intensity at all spots, while for the others, the intensity varies strongly. This confirms the observation in the optical micrographs that on a length scale of 20 microns, the thicker sample is quite homogeneous, while the others are not. However, the flake thickness and hence the electronic structure is more homogeneous, and over the spot size of the pump-probe experiment (150 microns), the inhomogeneity averages out.

The $\Delta T/T$ spectra of the reference sample are shown in Figure 5.3a for different pump-probe delays. As previously observed on MoS_2, there are six salient features in the visible spectral range [96]: three photobleaching peaks of the exciton absorption resonances A^0, B^0, and C^0, and three photoinduced absorption peaks A^-, B^-, and C^- ascribed to photogenerated charges, one for each of the excitons. The exciton bleaching features show a fast decay during the first few picoseconds, followed by a slower decay on the few-100 ps scale. The photoinduced absorption peaks grow during the first few picoseconds and then decay with a characteristic time similar to the slow exciton decay. Charge photogeneration occurs via a combination of a direct excitation mechanism (*i. e.* , within our instrumental resolution of $\sim$ 100 fs), and via dissociation of hot excitons, on a time scale of a few hundred femtoseconds to few picoseconds [96]. This process can be seen in Figure 5.3a as a fast decrease of the bleaching features A^0, B^0, and C^0 and a corresponding growth of

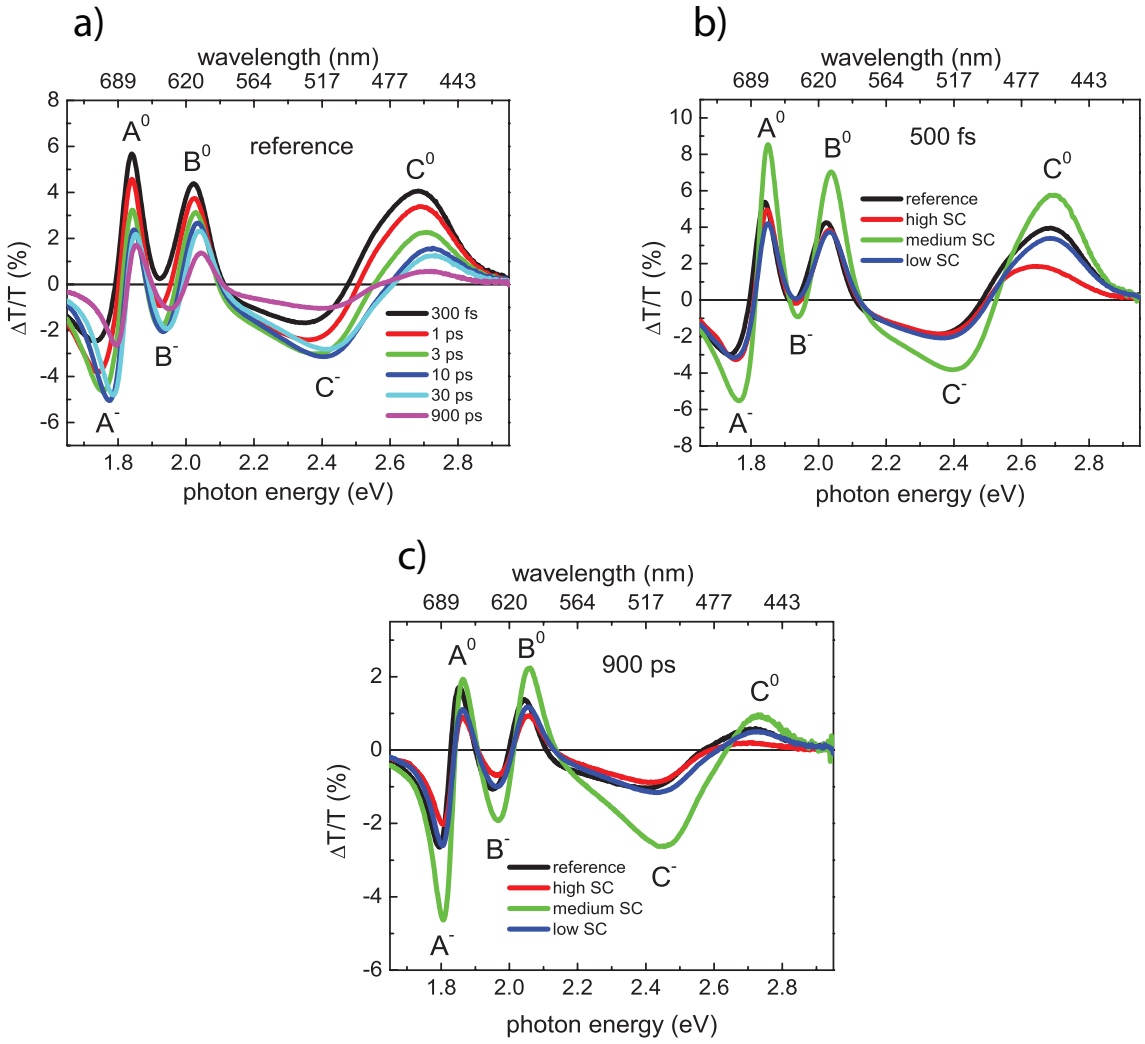


Figure 5.3: a) $\Delta T/T$ spectra of the reference sample at selected pump-probe delays. b,c) Comparison of $\Delta T/T$ spectra at 500 fs and 900 ps (bottom panel) pump-probe delays for different samples.

the charge features A^-, B^-, and C^- during the first few picoseconds. Together with the spectral change of shape, relative increase of the absorption and decrease of the bleaching features, the peaks also undergo a blueshift with increasing delay. In a more comprehensive study with different excitation fluences, it was found that the more the excited states the more the spectra are shifted to the red [96]. This has been explained as Stark effect due to photoexcited charges [187], [192], inter-excitonic interaction [88], or band gap renormalization [193]. Additionally, at short delays, the A^- and C^- photoinduced absorption peaks appear artificially red shifted due to the strong overlap with the A^0 and C^0 bleaching peaks, respectively. The fast decay of the bleaching peaks diminishes this effect with increasing pump-probe delay, resulting in an additional apparent temporal blueshift of these two photoinduced absorption features. After $\sim$ 10 ps, there is no significant shift of the spectra anymore and all features decay with a time constant of several hundred picoseconds, as has already been observed on individual flakes of MoS_2 [91]. Comparing the reference sample with those of different SC (Figure 5.3b,c), one finds a trend toward

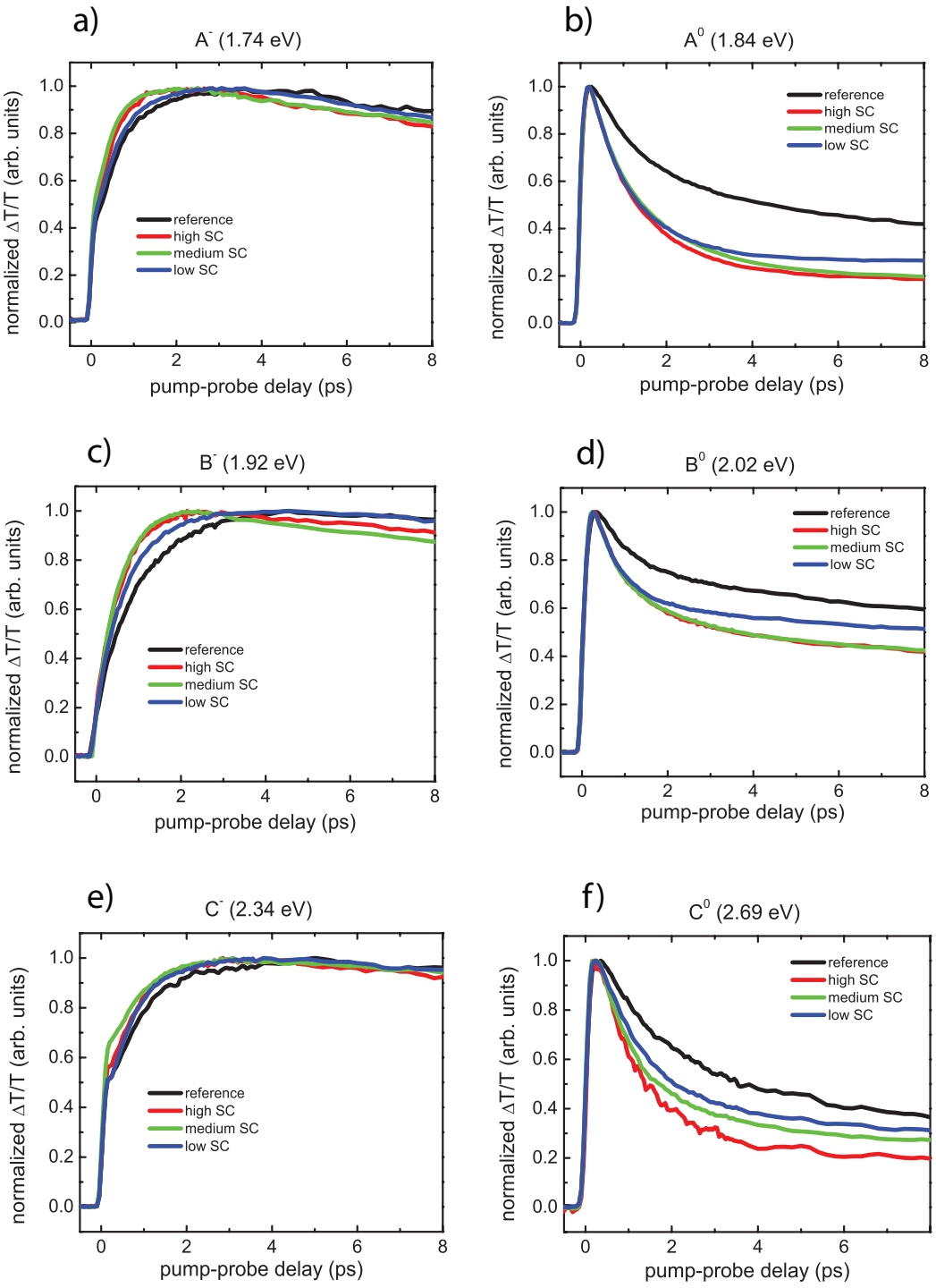


Figure 5.4: a) $\Delta T/T$ dynamics for different samples at selected probe energies: a) 1.74, b) 1.84, c) 1.92, d) 2.02, e) 2.34, and f) 2.69 eV.

slightly faster decay for higher SC. Additionally, for higher SC, the C exciton bleaching is weaker.

The trend toward faster initial exciton decay for higher SC observed in the $\Delta T/T$ spec-

tra is confirmed by the dynamics at representative probe energies, close to the respective spectral peaks depicted in Figure 5.4a,b,c,d,e,f. The timescale of the delayed charge formation (Figure 5.4a,c,e) corresponds to that of the initial exciton decay (Figure 5.4b,d,f), confirming the origin of these charges from the dissociation of excitons. Both the slow (few hundred picoseconds) decay component as well as the direct and delayed charge photogeneration yields do not vary appreciably between the different samples.

In conclusion, we have shown that the exciton and charge dynamics in few-layer MoS_2 flakes is robust against adsorption of the anionic surfactant sodium cholate. This is in stark contrast to other nanomaterials such as carbon nanotubes [194] or C_{60} fullerenes [195], where anionic surfactants generally lead to strong exciton quenching. This robustness highlights the viability of surfactant-assisted liquid processing (exfoliation, deposition, printing, etc) of MoS_2 and other semiconducting TMDCs.

Chapter 6

Conclusions

In this thesis I have presented the recently discovered electro-optical properties of the two-dimensional MoS_2 crystal. In particular, the flexible processing of the atomic single layer MoS_2 and its relatively easy employment in a FET architecture, allowed us to access its extraordinary electro-optical features.

Firstly, I have shown that a moderate in-plane electric field can efficiently modulate the charge carrier yield. In particular, by applying an electric field of 7 kV/cm^{-1} the PL is quenched by about 35%. In order to understand if field-induced dissociation is either a slow process competing with the radiative recombination and other non-radiative recombination channels, or a fast process, we performed femtosecond optical pump-probe microspectroscopy. I have shown that, upon photoexcitation, the dissociation of hot electron-hole pairs into charges proceeds with a time constant of 800 fs during the cooling. Upon application of an electric field, the time constant becomes slightly faster and the growing of the photoinduced absorption contribution is significantly stronger. The results from the two-level fit have shown a stronger and broader PA at the low-energy side as the main difference among the two spectral contributions of the primary and secondary ensemble populations ($P(t)$ and $S(t)$). Subsequently, I corroborated the results by considering the signal $\Delta(\Delta T/T)$ as a difference of the differential transmissions. This approach allows separating the charge generated by field-induced dissociation. The important $\Delta(\Delta T/T)$ absorption feature (at the energy interval 1.65–1.85 eV) and its time evolution were ascribed mostly to charge contribution generated by the electric field.

Secondly, for the first time we measured the transverse EA of monolayer MoS_2 by modulating the gate voltage V_g (with peak-to-peak voltage V_{pp}) in a transparent field effect transistor. I have shown, following a classical approach, that the electroabsorption spectrum is dominated by a linewidth broadening of around 15% at a modulated voltage of only $V_{pp} = 0.5$ V. Subsequently, I demonstrated that the linear variation of the broadening with the applied field strength, contrary to the QCSE, arises from a linear shift of the distance between the strongly overlapping exciton and trion resonances. We observed a red shift of the A^- peak (-9 meV) to be stronger than the blue shift of the A^0 peak ($+3$ meV). While the composite A peak with 36 meV between the A^0 and A^- peaks still looks very similar to a Gaussian, at 48 meV it does not, which explains why the fit by using the classical approach (with the derivative of the absorption resonances) deviates from the real data.

Comparing with a single layer of graphene, which has a negligible IL and an intrinsic upper limit of 0.10 dB for MD (2.3% transmission modulation), 2D transition metal dichalcogenides monolayer could be engineered in order to reach a similar negligible IL and MD of almost 0.5 dB, clearly exceeding the performance of graphene. In particular, I have shown a possible assessment for using TMDC in an electroabsorption modulator in

terms of fundamental parameters (for real application) and prospective technical solutions including other TMDC materials.

Our findings could enable a different approach to build up EAM with different TMDCs from any source (*e. g.* liquid exfoliated). As a starting point to demonstrate the feasibility of using such a material I have shown that femtosecond dynamics is remarkably stable against the surfactant adsorption in MoS_2 flakes from exfoliation in water. This could enable the development of simple structures, such as an ITO transparent electrode (one or two), to contact TMDC flakes embedded in polymer, then the realization of scalable EAMs with a control of thickness and size of the active medium.

Appendix A

Electroabsorption: Supplementary Materials

A.1 Surface Analysis of the Transfer Method

In order to understand how the transfer process and the chemical and annealing treatments (used to remove the remaining polymer) described in the methods section of the main text can influence the monolayer surface, we carried out a surface analysis on gate dielectric and on the transferred flakes. We first test the effect of the chemical treatment and annealing for an empty substrate of sapphire/ITO/HfO_2. Figure A.1a,b shows topography maps of the gate dielectric before and after the treatment described in the method taken by an Atomic Force Microscope (AFM). The maps do not reveal any morphological changes after the treatment and also the calculated root - mean - square surface roughness Rq of around 1nm in both cases suggests no topographic change in the HfO_2 layer. In Figure A.2a

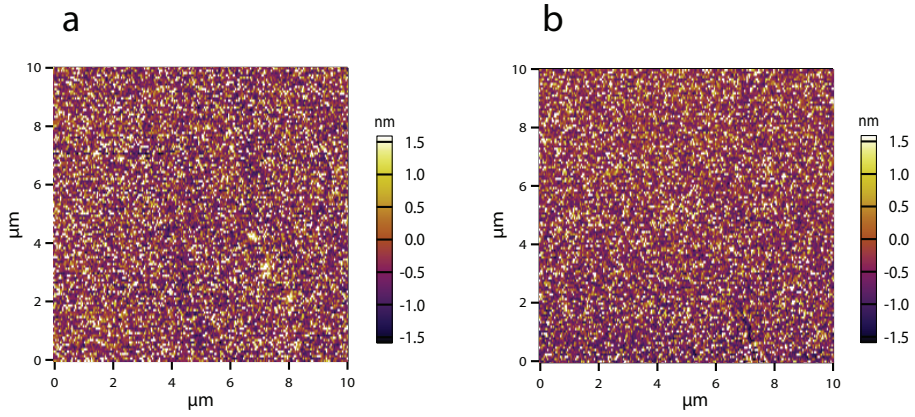


Figure A.1: AFM topographical image of the HfO_2 surface before a) and after b) treatment.

we show an AFM map of a transferred flake. AFM analysis becomes crucial in order to identify possible cracks in the material and to select the regions with high quality film where to subsequently fabricate the devices. The presence of cracks due to transfer is quite common when the material is approached and slightly forced to be in contact with the target substrate. We estimate the surface roughness outside the flake to be around 900 pm, which is comparable with the calculated roughness inside the flake (Rq = 960 pm). This suggests that the monolayer somehow follows the nanostructured surface of the dielectric layer. An AFM zoom inside the flake (Figure A.2b) shows the randomly

structured surface that comes from the substrate below the MoS_2 layer. The AFM images show the absence of polymer residues and wrinkles on the monolayer surface. In fact during the approaching procedure of the complex PDMS/PLLA/MoS_2 toward the chip target (Sapphire/ITO/HfO_2), the flakes are kept close to the surface of the target chip but not in contact. The temperature close to 100 °C allows the PLLA to stretch before contacting the target. This guarantees a good adhesion of the polymer and prevents the formation of wrinkles.

Since the positions of the E_{2g} and A_{1g} Raman modes are respectively sensible to the mechanical strain and to the doping level in the material, we measure Raman scattering before and after transferring the monolayer. Figure A.2c shows the two Raman spectra where the E_{2g} is insensitive to the changing of substrate and the A_{1g} mode red shifts by ~ 0.8 cm^{-1}. A phonon red shift of the A_{1g} by up to 2 cm^{-1} for different substrates has already been reported, indicating an increase of the doping in the MoS_2 monolayer [62]. It is known that substrates such as SiO_2 have a high density of charge impurities and lead to an increased doping at the dielectric - 2D material interface [164]. The redshift observed for the HfO_2 substrate only slightly less than reported for mica and SiO_2 substrates [62] suggests a possible small substrate doping. Alternatively, since the flakes on HfO_2 and sapphire have been processed differently, the amount of doping from adsorbed molecules may be different.

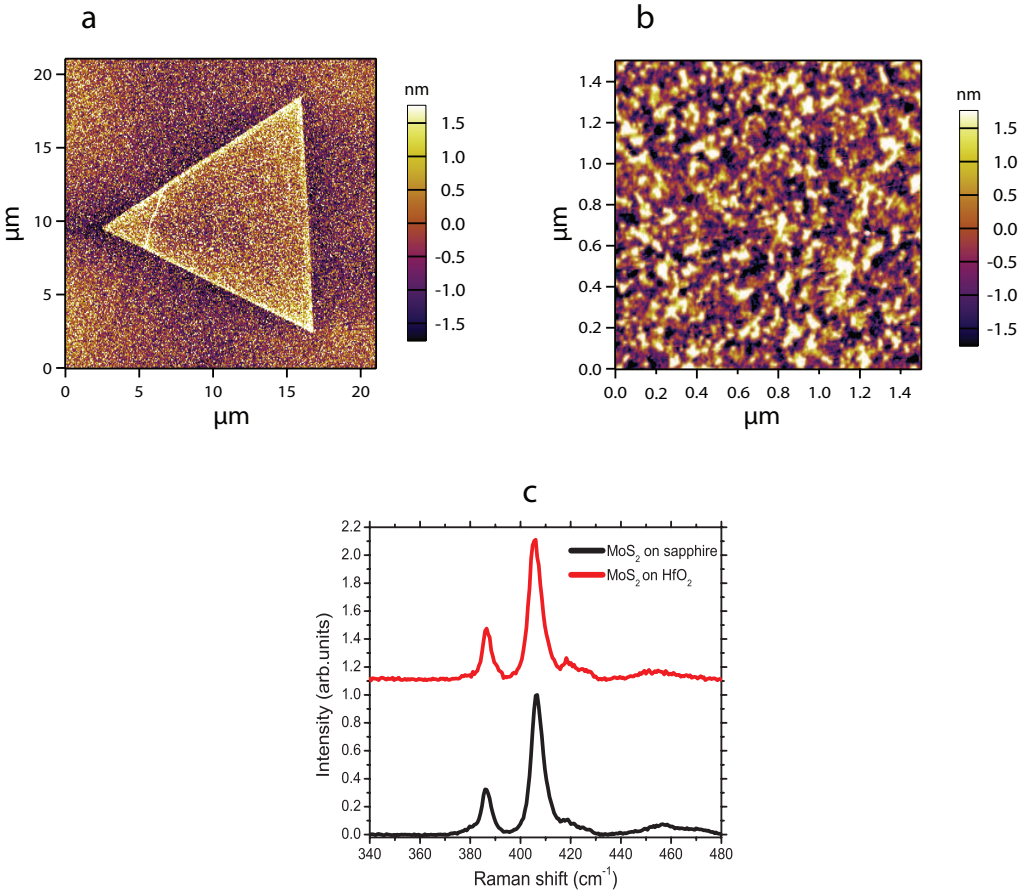


Figure A.2: a) AFM topography image of a single layer of MoS_2 transferred with PLLA. b) AFM image: zoom inside the flake. c) Normalized Raman spectra of 1L MoS_2 on sapphire and on HfO_2.

A.2 Details and Accuracy of the Used Fits

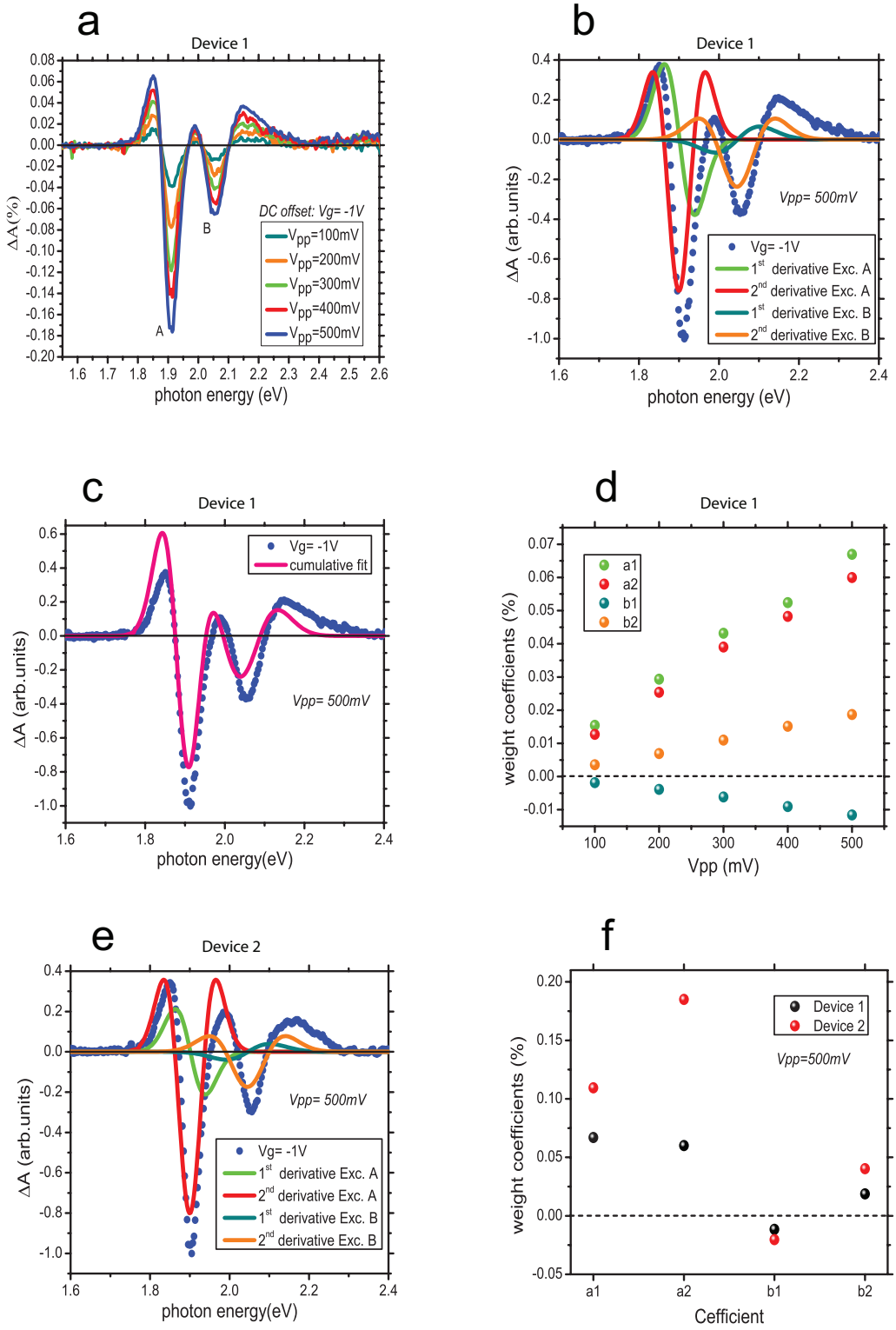


Figure A.3: a) Electroabsorption spectra of device 1 for different peak-to-peak voltage modulation amplitude V_{pp}. b,c,d) First and second derivative fits of the EA signal for device 1 as described in the text. e) Fit of the EA signal for device 2 at $V_{\mathrm{pp}} = 0.5$ V. f) Device 1 *vs.* device 2: comparison of the coefficients resulting from the fit.

First, we fitted the absorbance as a sum of two Gaussians plus a generic exponential background, and then the EA spectra, as is customary for EA, as a linear combination of first and second derivatives of these Gaussians. The EA spectrum of device 1 for different modulated voltages V_{pp} is shown in Figure A.3a, the fit of the normalized EA spectrum for $V_{\mathrm{pp}} = 500$ meV in Figure A.3c, the individual first and second derivatives in Figure A.3b. Figure A.3d shows the fit coefficients that reproduce the non-normalized signal as a linear combination of the normalized derivatives:

$$\Delta A = a_1\Big(\frac{\partial G^A}{\partial E}\Big)_n + a_2\Big(\frac{\partial^2 G^A}{\partial E^2}\Big)_n + b_1\Big(\frac{\partial G^B}{\partial E}\Big)_n + b_2\Big(\frac{\partial^2 G^B}{\partial E^2}\Big)_n. \tag{A.1}$$

The analogous fit is shown for device 2 (only $V_{\mathrm{pp}} = 500$ meV) in Figure A.3e. Figure A.3f compares the coefficients of both devices at the same $V_{\mathrm{pp}} = 500$ meV. For device 2, which has the stronger signal, all coefficients are larger by a similar factor 2-3.

Table A.1: Fit coefficients for device 1 according to Equation (A.1) for different V_{pp}.

Vpp (mV)	a1 (%)	a2(%)	b1(%)	b2(%)	*SSR*
100	0.01542	0.01267	-0.00183	0.00354	3.29985
200	0.02929	0.02536	-0.00383	0.00691	3.00274
300	0.04317	0.03898	-0.00613	0.01096	2.75541
400	0.05241	0.04825	-0.00901	0.01513	2.90385
500	0.06695	0.05993	-0.01153	0.01868	2.93135

For device 2, which gives the strongest signal, we show the cumulative fit in Figure A.4a and the fit of the absorption spectrum in Figure A.4b. From there we reconstruct the absorption spectrum (without the exponential background) with and without electric field in Figure A.4c. The following panels show the hypothetical absorption spectra if the field caused only a shift (Figure A.4d) or only a broadening of the A and B peak. While the shift alone can hardly reproduce the fit, the broadening alone already comes quite close, showing the dominant role of the broadening. It is strongest for the A peak, which is broadened by 16%, reducing its height by 14%. For device 1, where we measured at different V_{pp}, the broadening is linear in V_{pp} (Figure A.4f).

We now proceed to fitting the A peak as a superposition of the exciton peak A^0 and the trion peak A^-. Figure A.5a,b shows the absorption spectrum of device 2 without background without (a) and with (b) electric field. The fit has been repeated for three different gate voltages (Figure A.5d,e), confirming a field-induced increase in the distance between the peaks from 36 to 48 meV (Figure A.5c). Device 1 gives a weaker signal by itself, and it has also been measured at lower modulated voltages V_{pp} down to 100 mV. Consequently, the shifts are weaker (Figure A.6), but still noticeable, especially those of the A^- peak as well as the distance between the two peaks are clearly linear in the applied electric field strength.

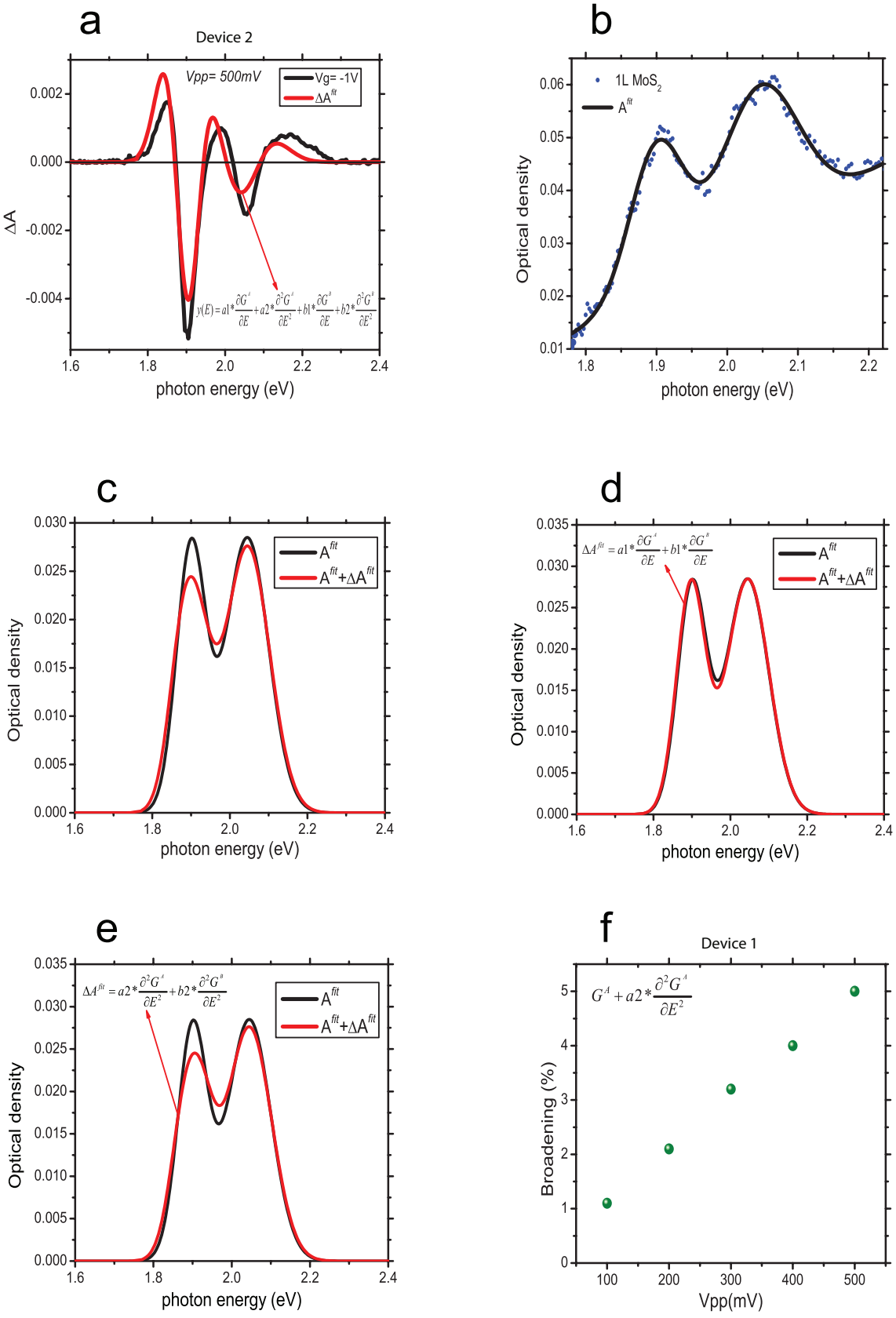
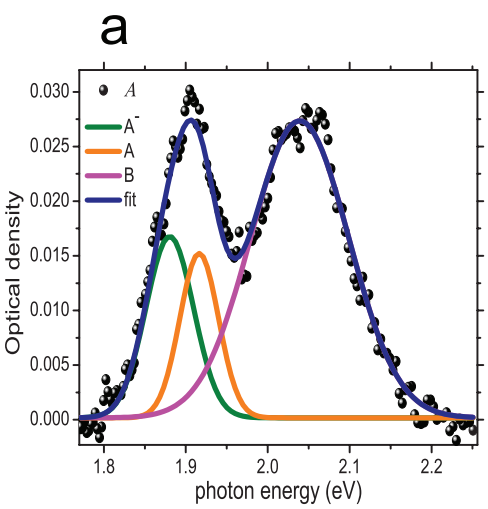
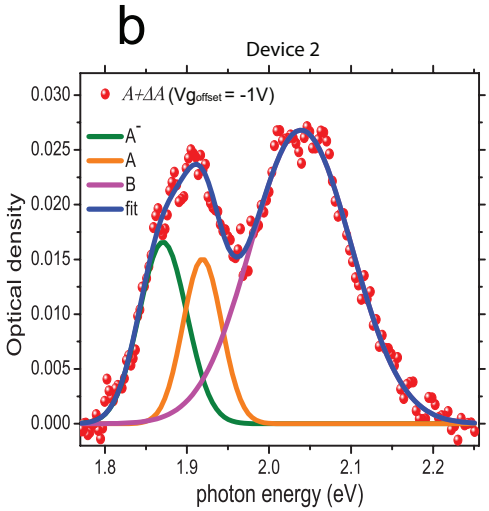


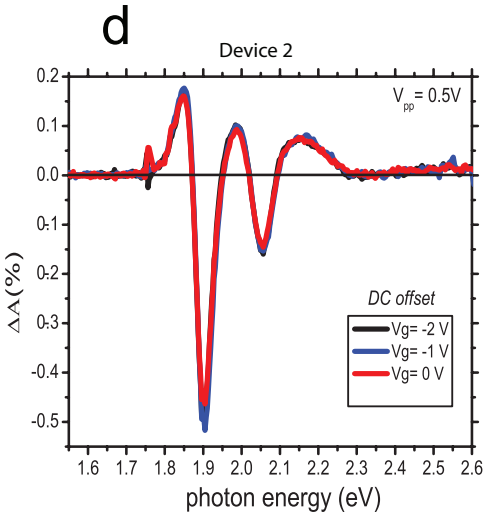
Figure A.4: a) EA signal ΔA (red curve) and the linear combination fit (black curve). b) Absorbance A and related fit. c) Fit of the absorption spectrum with and without electric field. d) Hypothetical absorption spectra if the field caused only a shift or e) broadening. f) Broadening as a function of V_{pp} for device 1.





c

Absorbance							*Absorbance + ΔA*		
A⁻			**A⁰**			**relative distance**	**A⁻**	**A⁰**	**relative distance**
x_c (meV)	σ (meV)	*Ampl.*	x_c (meV)	σ (meV)	*Ampl.*	Δx_c (meV)	x_c (meV)	x_c (meV)	Δx_c (meV)
1880.5 ± 0.8	29.1 ± 0.6	0.01659 ± 3.1*10^{-4}	1916.5 ± 0.8	23.6 ± 0.7	0.01505 ± 3.5*10^{-4}	**36** ± 1.6	1871.4 ± 0.7	1919.3 ± 0.7	**47.9** ± 1.4



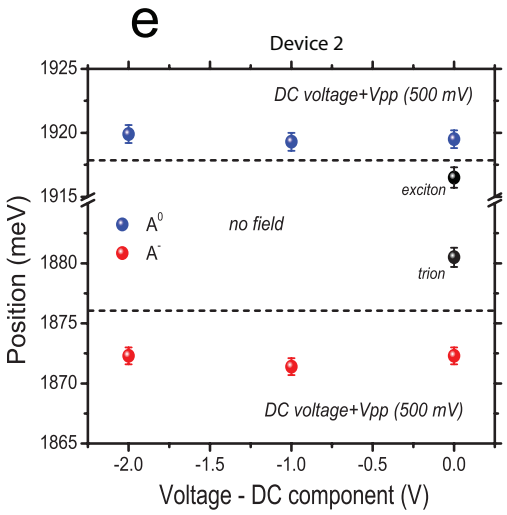
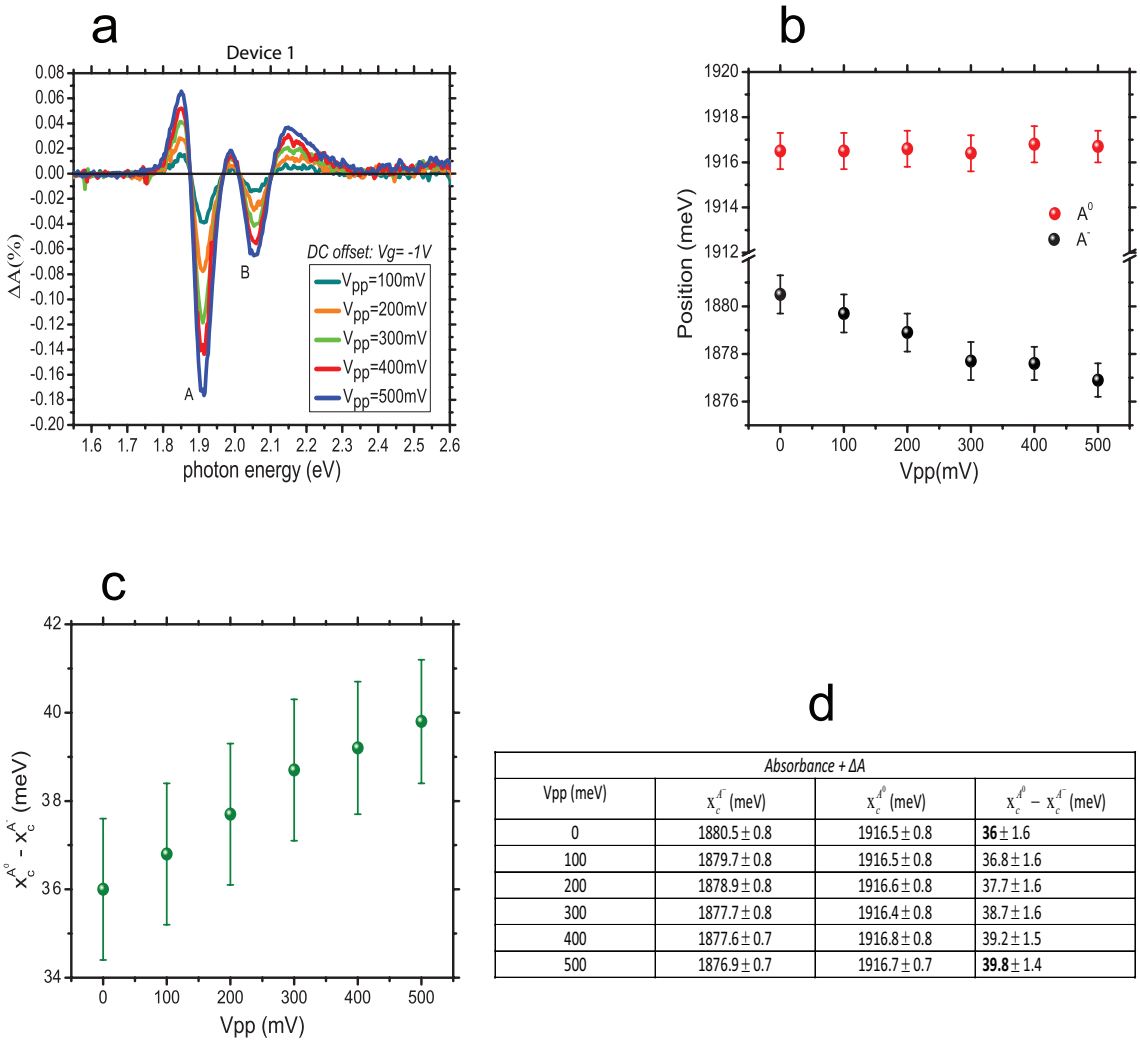


Figure A.5: Fits for device 2 with separate A^0 exciton and A^- trion peaks as described in the text.



d

Absorbance + ΔA			
Vpp (meV)	$x_c^{A^-}$ (meV)	$x_c^{A^0}$ (meV)	$x_c^{A^0} - x_c^{A^-}$ (meV)
0	1880.5 ± 0.8	1916.5 ± 0.8	**36** ± 1.6
100	1879.7 ± 0.8	1916.5 ± 0.8	36.8 ± 1.6
200	1878.9 ± 0.8	1916.6 ± 0.8	37.7 ± 1.6
300	1877.7 ± 0.8	1916.4 ± 0.8	38.7 ± 1.6
400	1877.6 ± 0.7	1916.8 ± 0.8	39.2 ± 1.5
500	1876.9 ± 0.7	1916.7 ± 0.7	**39.8** ± 1.4

Figure A.6: Fits EA signal–Device 1– with separate A^0 exciton and A^- trion. a) EA signal. b) Modulation voltage dependent A^0 and A^- positions. c) Modulation voltage-dependent distance between A^0 and A^-. d) Data of b) and c) as a table.

References

[1] F. Schwierz, "Graphene transistors," *Nature Nanotechnology*, vol. 5, no. 7, pp. 487–496, 2010.

[2] K. S. Novoselov, A. K. Geim, S. V.Morozov, D. Jiang, Y. Zhang, S. V. Dubonos, I. V. Grigorieva, and A. A. Firsov, "Electric field effect in atomically thin carbon films," *Science*, vol. 306, no. 5696, pp. 666–669, 2004.

[3] K. S. Novoselov, D. Jiang, F. Schedin, T. J. Booth, V. V. Khotkevich, S. V. Morozov, and A. K. Geim, "Two-dimensional atomic crystals," *PNAS*, vol. 102, no. 30, pp. 10 451–10 453, 2005.

[4] A. Kuc, N. Zibouche, and T. Heine, "Influence of quantum confinement on the electronic structure of the transition metal sulfide TS_2," *Phys. Rew. B*, vol. 83, no. 24, p. 245 213, 2011.

[5] D. Lembke and A. Kis, "Breakdown of high-performance monolayer MoS_2 transistors," *ACS Nano*, vol. 6, no. 11, pp. 10 070–10 075, 2012.

[6] Q. H. Wang, K. Kalantar-Zadeh, A. Kis, J. N. Coleman, and M. S. Strano, "Electronics and optoelectronics of two-dimensional transition metal dichalcogenides," *Nature Nanotechnology*, vol. 7, pp. 699–712, 2012.

[7] K. F. Mak and J. Shan, "Photonics and optoelectronics of 2D semiconductor transition metal dichalcogenides," *Nature Photonics*, vol. 10, pp. 216–226, 2016.

[8] Z. Sun, A. Martinez, and F. Wang, "Optical modulators with 2D layered materials," *Nature Photonics*, vol. 10, pp. 227–238, 2016.

[9] M. Fontana, T. Deppe, A. K. Boyd, M. Rinzan, M. P. Amy Y. Liu, and P. Barbara, "Electron-hole transport and photovoltaic effect in gated MoS_2 Schottky junctions," *Scientific Reports*, vol. 3, no. 1634, 2013.

[10] C.-H. Lee, G.-H. Lee, A. M. van der Zande, W. Chen, Y. Li, M. Han, X. Cui, G. Arefe, C. Nuckolls, T. F. Heinz, J. Guo, J. Hone, and P. Kim, "Atomically thin p-n junctions with van der Waals heterointerfaces," *Nature Nanotechnology*, vol. 9, pp. 676–681, 2014.

[11] B. W. H. Baugher, H. O. H. Churchill, Y. Yang, and P. Jarillo-Herrero, "Optoelectronic devices based on electrically tunable p-n diodes in a monolayer dichalcogenide," *Nature Nanotechnology*, vol. 9, no. 4, pp. 262–267, 2014.

[12] M.-L. Tsai, S.-H. Su, J.-K. Chang, D.-S. Tsai, C.-H. Chen, C.-I. Wu, L.-J. Li, L.-J. Chen, and J.-H. He, "Monolayer MoS_2 heterojunction solar cells," *ACS Nano*, vol. 8, no. 8, pp. 8317–8322, 2014.

[13] Z. Sun, A. Martinez, and F. Wang, "Optical modulators with 2D layered materials," *Nature Photonics*, vol. 10, pp. 227–238, 2016.

[14] N. Youngblood, Y. Anugrah, R. Ma, S. J. Koester, and M. Li, "Multifunctional graphene optical modulator and photodetector integrated on silicon waveguides," *Nano Letters*, vol. 14, no. 5, pp. 2741–2746, 2014.

[15] B. Sensale-Rodriguez, S. Rafique, R. Yan, M. Zhu, V. Protasenko, D. Jena, L. Liu, and H. G. Xing, "Terahertz imaging employing graphene modulator arrays," *Optics Express*, vol. 21, no. 2, pp. 2324–2330, 2013.

[16] D. Jariwala, V. K. Sangwan, L. J. Lauhon, T. J. Marks, and M. C. Hersam, "Emerging device applications for semiconducting two-dimensional transition metal dichalcogenides," *ACS Nano*, vol. 8, no. 2, pp. 1102–1120, 2014.

[17] M. Chhowalla, H. S. Shin, G. Eda, L.-J. Li, K. P. Loh, and H. Zhang, "The chemistry of twodimensional layered transitionmetal dichalcogenide nanosheets," *Nature Chemistry*, vol. 5, no. 4, pp. 263–275, 2013.

[18] B. Radisavljevic, A. Radenovic, J. Brivio, V. Giacometti, and A. Kis, "Single-layer MoS_2 transistors," *Nature Nanotechnology*, vol. 9, pp. 147–150, 2011.

[19] B. Radisavljevic, M. B. Whitwick, and A. Kis, "Integrated circuits and logic operations based on single-layer MoS_2," *ACS Nano*, vol. 5, no. 12, pp. 9934–9938, 2011.

[20] O. Lopez-Sanchez, D. Lembke, M. Kayci, A. Radenovic, and A. Kis, "Ultrasensitive photodetectors based on monolayer MoS_2," *Nature Nanotechnology*, vol. 8, no. 7, pp. 497–501, 2013.

[21] K. F. Mak, C. Lee, J. Hone, J. Shan, and T. F. Heinz, "Atomically thin MoS_2: A new direct-gap semiconductor," *Phys. Rew. Lett.*, vol. 105, no. 13, p. 136 805, 2010.

[22] A. Splendiani, L. Sun, Y. Zhang, T. Li, J. Kim, C.-Y. Chim, G. Galli, and F. Wang, "Emerging photoluminescence in monolayer MoS_2," *Nano Letters*, vol. 10, no. 4, pp. 1271–1275, 2010.

[23] A. H. C. Neto, "Charge density wave, superconductivity, and anomalous metallic behavior in 2D transition metal dichalcogenides," *Phys. Rev. Lett.*, vol. 86, no. 19, p. 4382, 2001.

[24] S. Bertolazzi, J. Brivio, and A. Kis, "Stretching and breaking of ultrathin MoS_2," *ACS Nano*, vol. 5, no. 12, pp. 9703–9709, 2011.

[25] M. M. Benameur, B. Radisavljevic, J. S. Héron, S. Sahoo, H. Berger, and A. Kis, "Visibility of dichalcogenide nanolayers," *Nanotechnology*, vol. 22, no. 12, 2011.

[26] H. Li, G. Lu, Z. Yin, Q. He, H. Li, Q. Zhang, and H. Zhang, "Optical identification of single- and few-layer MoS_2 sheets," *Nanotechnology*, vol. 8, no. 5, pp. 682–686, 2012.

[27] Y.-C. Lin, W. Zhang, J.-K. Huang, K.-K. Liu, Y.-H. Lee, C.-T. Liang, C.-W. Chu, and L.-J. Li, "Wafer-scale MoS_2 thin layers prepared by MoO_3 sulfurization," *Nanoscale*, vol. 4, no. 20, pp. 6637–6641, 2012.

[28] Y. Zhan, Z. Liu, S. Najmaei, P. M. Ajayan, and J. Lou, "Large-area vapor-phase growth and characterization of MoS_2 atomic layers on a SiO_2 substrate," *Small*, vol. 8, no. 7, pp. 966–971, 2012.

[29] Y.-H. Lee, X.-Q. Zhang, W. Zhang, M.-T. Chang, C.-T. Lin, K.-D. Chang, Y.-C. Yu, J. T.-W.Wang, C.-S. Chang, L.-J. Li, and T.-W. Lin, "Synthesis of large-area MoS_2 atomic layers with chemical vapor deposition," *Adv. Funct. Mater.*, vol. 24, no. 17, pp. 2320–2325, 2012.

[30] D. Dumcenco, D. Ovchinnikov, K. Marinov, P. Lazić, M. Gibertini, N. Marzari, O. L. Sanchez, Y.-C. Kung, D. Krasnozhon, M.-W. Chen, S. Bertolazzi, P. Gillet, A. F. i Morral, A. Radenovic, and A. Kis, "Large-area epitaxial monolayer MoS_2," *ACS Nano*, vol. 9, no. 4, pp. 4611–4620, 2015.

[31] C. Backes, B. M. Szydlowska, A. Harvey, S. Yuan, V. Vega-Mayoral, B. R. Davies, P.-l. Zhao, D. Hanlon, E. J. G. Santos, M. I. Katsnelson, W. J. Blau, C. Gadermaier, and J. N. Coleman, "Production of highly monolayer enriched dispersions of liquid-exfoliated nanosheets by liquid cascade centrifugation," *ACS Nano*, vol. 10, no. 1, pp. 1589–1601, 2016.

[32] J. N. Coleman, M. Lotya, A. O'Neill, S. D. Bergin, P. J. King, U. Khan, K. Young, A. Gaucher, S. De, R. J. Smith, I. V. Shvets, S. K. Arora, G. Stanton, H.-Y. Kim, K. Lee, G. T. Kim, G. S. Duesberg, T. Hallam, J. J. Boland, J. J.Wang, J. F. Donegan, J. C. Grunlan, G.Moriarty, A. Shmeliov, R. J. Nicholls, J. M. Perkins, E. M. Grieveson, K. Theuwissen, D. W. McComb, P. D. Nellist, and V. Nicolosi, "Two-dimensional nanosheets produced by liquid exfoliation of layered materials," *Science*, vol. 331, no. 6017, pp. 568–571, 2011.

[33] R. J. Smith, P. J. King, M. Lotya, C. Wirtz, U. Khan, S. De, A. O'Neill, G. S. Duesberg, J. C. Grunlan, G. Moriarty, J. Chen, J. Wang, A. I. Minett, V. Nicolosi, and J. N. Coleman, "Large-scale exfoliation of inorganic layered compounds in aqueous surfactant solutions," *Adv. Funct. Mater.*, vol. 23, no. 34, pp. 3944–3948, 2012.

[34] P. May, U. Khan, J. M. Hughes, and J. N. Coleman, "Role of solubility parameters in understanding the steric stabilization of exfoliated two-dimensional nanosheets by adsorbed polymers," *J. Phys. Chem. C*, vol. 116, no. 20, pp. 11 393–11 400, 2012.

[35] C. Backes, R. J. Smith, N. McEvoy, N. C. Berner, D. McCloskey, H. C. Nerl, A. O'Neill, P. J. King, T. Higgins, D. Hanlon, N. Scheuschner, J. Maultzsch, L. Houben, G. S. Duesberg, J. F. Donegan, V. Nicolosi, and J. N. Coleman, "Edge and confinement effects allow in situ measurement of size and thickness of liquid-exfoliated nanosheets," *Nature Communications*, vol. 5, no. 4576, 2014.

[36] V. Vega-Mayoral, C. Backes, D. Hanlon, U. Khan, Z. Gholamvand, M. O'Brien, G. S. Duesberg, C. Gadermaier, and J. N. Coleman, "Photoluminescence from liquid-exfoliated WS_2 monomers in poly(vinyl alcohol) polymer composites," *Adv. Funct. Mater.*, vol. 26, pp. 1028–1039, 2016.

[37] R. G. Dickinson and L. Pauling, "The crystal structure of molybdenite," *Journal of the American Chemical Society*, vol. 45, no. 6, pp. 1466–1471, 1923.

[38] L. F.Mattheiss, "Energy bands for 2H-$NbSe_2$ and 2H-MoS_2," *Phys. Rev. Lett.*, vol. 30, no. 17, pp. 784–787, 1973.

[39] A. N. Enyashin, L. Yadgarov, L. Houben, I. Popov, M.Weidenbach, R. Tenne, M. Bar-Sadan, and G. Seifert, "New route for stabilization of 1T-WS_2 and MoS_2 phases," *The Journal of Physical Chemistry C*, vol. 115, no. 50, pp. 24 586–24 591, 2011.

[40] D. Yang, S. J. Sandoval, W. M. R. Divigalpitiya, J. C. Irwin, and R. D. Frindt, "Structure of single-molecular-layer MoS_2 phases," *Phys. Rew. B*, vol. 43, no. 14, pp. 12 053–12 056, 1991.

[41] M. A. Py and R. R. Haering, "Structural destabilization induced by lithium intercalation in MoS_2 and related compounds," *Can. J. Phys*, vol. 61, no. 1, pp. 76–84, 1983.

[42] G. Eda, H. Yamaguchi, D. Voiry, T. Fujita, M. Chen, and M. Chhowalla, "Photoluminescence from chemically exfoliated MoS_2," *Nano Lett.*, vol. 11, no. 12, pp. 5111–5116, 2011.

[43] H.-L. Tsai, J. Heising, J. L. Schindler, C. R. Kannewurf, and M. G. Kanatzidis, "Exfoliated-Restacked Phase of WS_2," *Chem. Mater.*, vol. 9, no. 4, pp. 879–882, 1997.

[44] R. A. Gordon, D. Yang, E. D. Crozier, D. T. Jiang, and R. F. Frindt, "Structures of exfoliated single layers of WS_2, MoS_2, and $MoSe_2$ in aqueous suspension," *Phys. Rev. B*, vol. 65, p. 125 407, 2002.

[45] G. Eda, T. Fujita, H. Yamaguchi, D. Voiry, and M. C. nd M. Chhowalla, "Coherent atomic and electronic heterostructures of single-layer MoS_2," *ACS Nano*, vol. 6, no. 8, pp. 7311–7317, 2012.

[46] R. Kappera, D. Voiry, S. E. Yalcin, B. Branch, G. Gupta, A. D. Mohite, and M. Chhowalla, "Phase-engineered low-resistance contacts for ultrathin MoS_2 transistors," *Nature Materials*, vol. 13, no. 12, pp. 1128–1134, 2014.

[47] Y.-C. Lin, D. O. Dumcenco, Y.-S. Huang, and K. Suenaga, "Atomic mechanism of the semiconducting-to-metallic phase transition in single-layered MoS_2," *Nature Nanotechnology*, vol. 9, no. 5, pp. 391–396, 2014.

[48] S. Lebègue and O. Eriksson, "Electronic structure of two-dimensional crystals from ab initio theory," *Phys. Rew. B*, vol. 79, no. 11, p. 115 409, 2009.

[49] T. Cheiwchanchamnangij and W. R. L. Lambrecht, "Quasiparticle band structure calculation of monolayer, bilayer, and bulk MoS_2," *Phys. Rew. B*, vol. 85, no. 20, p. 205 302, 2012.

[50] T. Li and G. Galli, "Electronic properties of MoS_2 nanoparticles semiconductor," *J. Phys. Chem. C*, vol. 111, no. 44, pp. 16 192–16 196, 2007.

[51] T. J. Wieting and J. L. Verble, "Infrared and raman studies of long-wavelength optical phonons in hexagonal MoS_2," *Phys. Rew. B*, vol. 3, no. 12, pp. 4286–4292, 1971.

[52] A. Molina-Sànchez and L. Wirtz, "Phonons in single-layer and few-layer MoS_2 and WS_2," *Phys. Rew. B*, vol. 84, no. 15, p. 155 413, 2011.

[53] N. Wakabayashi, H. G. Smith, and R. M. Nicklow, "Lattice dynamics of hexagonal MoS_2 studied by neutron scattering," *Phys. Rew. B*, vol. 12, no. 2, pp. 659–663, 1975.

[54] S. J. Sandoval, D. Yang, R. D. Frindt, and J. C. Irwin, "Raman study and lattice dynamics of single molecular layers of MoS_2," *Phys. Rew. B*, vol. 44, no. 8, pp. 3955–3962, 1991.

[55] Y. Cai, J. Lan, G. Zhang, and Y.-W. Zhang, "Lattice vibrational modes and phonon thermal conductivity of monolayer MoS_2," *Phys. Rew. B*, vol. 89, no. 3, p. 035 438, 2011.

[56] J.-W. Jiang, H. S. Park, and T. Rabczuk, "Molecular dynamics simulations of single-layer molybdenumdisulphide (MoS_2): Stillinger-Weber parametrization, mechanical properties, and thermal conductivity," *Journal of Applied Physics*, vol. 114, no. 6, p. 064 307, 2013.

[57] C. Lee, H. Yan, L. E. Brus, T. F. Heinz, J. Hone, and S. Ryu, "Anomalous lattice vibrations of single- and few-layer MoS_2," *ACS Nano*, vol. 4, no. 5, pp. 2695–2700, 2010.

[58] A. Berkdemir, H. R. Gutiérrez, A. R. Botello-Méndez, N. Perea-López, A. L. Elías, C.-I. Chia, B. Wang, V. H. Crespi, F. López-Urías, J.-C. Charlier, H. Terrones, and M. Terrones, "Identification of individual and few layers of WS_2 using raman spectroscopy," *Scientific Reports*, vol. 3, no. 1755, 2013.

[59] S. Najmaei, Z. Liu, P. M. Ajayan, and J. Lou, "Thermal effects on the characteristic raman spectrumof molybdenum disulfide MoS_2 of varying thicknesses," *Appl. Phys. Lett.*, vol. 100, no. 1, p. 013 106, 2012.

[60] B. Chakraborty, A. Bera, D. V. S. Muthu, S. Bhowmick, U. V. Waghmare, and A. K. Sood, "Symmetry-dependent phonon renormalization in monolayer MoS_2 transistor," *Phys. Rew. B*, vol. 85, no. 16, p. 161 403, 2012.

[61] Y. Wang, C. Cong, C. Qiu, and T. Yu, "Raman spectroscopy study of lattice vibration and crystallographic orientation of monolayerMoS_2 under uniaxial strain," *Small*, vol. 9, no. 17, pp. 2857–2861, 2013.

[62] M. Buscema, G. A. Steele, H. S. J. van der Zant, and A. Castellanos-Gomez, "The effect of the substrate on the raman and photoluminescence emission of single-layer MoS_2," *Nano Research*, vol. 7, no. 4, pp. 561–571, 2013.

[63] R. F. Frindt and A. D. Yoffe, "Physical properties of layer structures: Optical properties and photoconductivity of thin crystals of molybdenum disulphide," *Proceedings of the Royal Society of London A:Mathematical, Physical and Engineering Sciences*, vol. 273, no. 1352, pp. 69–83, 1963.

[64] J. Wilson and A. Yoffe, "The transition metal dichalcogenides discussion and interpretation of the observed optical, electrical and structural properties," *Advances in Physics*, vol. 18, no. 73, pp. 193–335, 1969.

[65] R. F. Frindt, "Optical absorption of a few unit-cell layers of MoS_2," *Physical Review*, vol. 140, no. 2A, A536–A539, 1965.

[66] R. Coehoorn, C. Haas, J. Dijkstra, C. J. F. Flipse, R. A. de Groot, and A. Wold, "Electronic structure of $MoSe_2$, MoS_2, and WSe_2. i. band-structure calculations and photoelectron spectroscopy," *Phys. Rev. B*, vol. 35, no. 12, pp. 6195–6202, 1987.

[67] R. Coehoorn, C. Haas, and R. A. de Groot, "Electronic structure of $MoSe_2$, MoS_2, and WSe_2. ii. the nature of the optical band gaps," *Phys. Rev. B*, vol. 35, no. 12, pp. 6203–6206, 1987.

[68] K. F.Mak, K. He, J. Shan, and T. F. Heinz, "Control of valley polarization in monolayer MoS_2 by optical helicity," *Nature Nanotechnology*, vol. 7, no. 8, pp. 494–498, 2012.

[69] S. Tongay, J. Zhou, C. Ataca, J. Liu, J. S. Kang, T. S.Matthews, L. You, J. Li, J. C. Grossman, and J. Wu, "Broad-range modulation of light emission in two-dimensional semiconductors by molecular physisorption gating," *Nano Letters*, vol. 13, no. 6, pp. 2831–2836, 2013.

[70] H. Nan, Z.Wang, W.Wang, Z. Liang, Y. Lu, Q. Chen, D. He, P. Tan, F.Miao, X.Wang, J.Wang, and Z. Ni, "Strong photoluminescence enhancement of MoS_2through defect engineering and oxygen bonding," *ACS Nano*, vol. 8, no. 6, pp. 5738–5745, 2014.

[71] S. Mouri, Y.Miyauchi, and K.Matsuda, "Tunable photoluminescence of monolayer MoS_2 via chemical doping," *Nano Letters*, vol. 13, no. 12, pp. 5944–5948, 2013.

[72] D. Xiao, W. Yao, and Q. Niu, "Valley-contrasting physics in graphene: Magnetic moment and topological transport," *Phys. Rev. Lett.*, vol. 99, no. 23, p. 236 809, 2007.

[73] W. Yao, D. Xiao, and Q. Niu, "Valley-dependent optoelectronics from inversion symmetry breaking," *Phys. Rev. B*, vol. 77, no. 23, p. 235 406, 2008.

[74] Y. P. Shkolnikov, E. P. D. Poortere, E. Tutuc, and M. Shayegan, "Valley splitting of AlAs two-dimensional electrons in a perpendicular magnetic field," *Phys. Rev. Lett.*, vol. 89, no. 22, p. 226 805, 2002.

[75] H. Zeng, J. Dai, W. Yao, D. Xiao, and X. Cui, "Valley polarization in MoS_2 monolayers by optical pumping," *Nature Nanotechnology*, vol. 7, no. 8, pp. 490–493, 2012.

[76] T. Cao, G.Wang, W. Han, H. Ye, C. Zhu, J. Shi, Q. Niu, P. Tan, E.Wang, B. Liu, and J. Feng, "Valley-selective circular dichroism of monolayer molybdenum disulphide," *Nature Communications*, vol. 3, no. 887, 2012.

[77] Y. J. Zhang, T. Oka, R. Suzuki, J. T. Ye, and Y. Iwasa, "Electrically switchable chiral light-emitting transistor," *Science*, vol. 334, no. 6185, pp. 725–728, 2014.

[78] S. B. Nam, D. C. Reynolds, C. W. Litton, R. J. Almassy, T. C. Collins, and C. M. Wolfe, "Free-exciton energy spectrum in GaAs," *Phys. Rev. B*, vol. 13, no. 2, pp. 761–767, 1976.

[79] D. A. B. Miller, D. S. Chemla, T. C. Damen, A. C. Gossard, W. Wiegmann, T. H. Wood, and C. A. Burrus, "Electric field dependence of optical absorption near the band gap of quantum-well structures," *Phys. Rev. B*, vol. 32, no. 2, pp. 1043–1060, 1985.

[80] A. Ramasubramaniam, "Large excitonic effects in monolayers of molybdenum and tungsten dichalcogenides," *Phys. Rev. B*, vol. 86, no. 11, p. 115 409, 2012.

[81] Z. Ye, T. Cao, K. O'Brien, H. Zhu, X. Yin, Y. Wang, S. G. Louie, and X. Zhang, "Probing excitonic dark states in single-layer tungsten disulphide," *Nature*, vol. 513, pp. 214–218, 2014.

[82] B. L. Evans and P. A. Young, "Exciton spectra in thin crystals," *Proceedings of the Royal Society of London A:Mathematical, Physical and Engineering Sciences*, vol. 298, no. 1452, pp. 74–96, 1967.

[83] A. Chernikov, T. C. Berkelbach, H. M. Hill, A. Rigosi, Y. Li, O. B. Aslan, D. R. Reichman, M. S. Hybertsen, and T. F. Heinz, "Exciton binding energy and nonhydrogenic rydberg series in monolayer WS_2," *Phys. Rev. Lett.*, vol. 113, no. 7, p. 076 802, 2014.

[84] H. M. Hill, A. F. Rigosi, C. Roquelet, A. Chernikov, T. C. Berkelbach, D. R. Reichman, M. S. Hybertsen, L. E. Brus, and T. F. Heinz, "Observation of excitonic rydberg states in monolayer MoS_2 and WS_2 by photoluminescence excitation spectroscopy," *Nano Letters*, vol. 15, no. 5, pp. 2992–2997, 2015.

[85] K. F. Mak, K. He, C. Lee, G. H. Lee, J. Hone, T. F. Heinz, and J. Shan, "Tightly bound trions in monolayer MoS_2," *Nature Materials*, vol. 12, pp. 207–211, 2013.

[86] Y. You, X.-X. Zhang, Timothy, C. Berkelbach, M. S. Hybertsen, D. R. Reichman, and T. F. Heinz, "Observation of biexcitons in monolayer WSe_2," *Nature Physics*, vol. 11, pp. 477–481, 2015.

[87] A. Chernikov, A. M. van der Zande, H. M. Hill, A. F. Rigosi, A. Velauthapillai, J. Hone, and T. F. Heinz, "Electrical tuning of exciton binding energies in monolayer WS_2," *Phys. Rev. Lett.*, vol. 115, no. 12, p. 126 802, 2015.

[88] S. Sim, J. Park, J.-G. Song, C. In, Y.-S. Lee, H. Kim, and H. Choi, "Exciton dynamics in atomically thin MoS_2: Interexcitonic interaction and broadening kinetics," *Phys. Rev. B*, vol. 88, no. 7, p. 075 434, 2013.

[89] C. Mai, A. Barrette, Y. Yu, Y. G. Semenov, K. W. Kim, L. Cao, and K. Gundogdu, "Many-body effects in valleytronics: Direct measurement of valley lifetimes in single-layer MoS_2," *Nano Letters*, vol. 14, no. 1, pp. 202–206, 2014.

[90] E. A. A. Pogna, M. Marsili, D. D. Fazio, S. D. Conte, C. Manzoni, D. Sangalli, D. Yoon, A. Lombardo, A. C. Ferrari, A. Marini, G. Cerullo, and D. Prezzi, "Photo-induced bandgap renormalization governs the ultrafast response of single-layer MoS_2," *ACS Nano*, vol. 10, no. 1, pp. 1182–1188, 2016.

[91] H. Shi, R. Yan, S. Bertolazzi, J. Brivio, B. Gao, A. Kis, D. Jena, H. G. Xing, and L. Huang, "Exciton dynamics in suspended monolayer and few-layer MoS_2 2D crystals," *ACS Nano*, vol. 7, no. 2, pp. 1072–1080, 2013.

[92] Q. Cui, F. Ceballos, N. Kumar, and H. Zhao, "Transient absorption microscopy of monolayer and bulk WSe_2," *ACS Nano*, vol. 78, no. 3, pp. 2970–2976, 2014.

[93] Z. Nie, R. Long, L. Sun, C.-C. Huang, J. Zhang, Q. Xiong, D. W. Hewak, Z. Shen, O. V. Prezhdo, and Z.-H. Loh, "Ultrafast carrier thermalization and cooling dynamics in few-layer MoS_2," *ACS Nano*, vol. 8, no. 10, pp. 10 931–10 940, 2014.

[94] D. Sun, Y. Rao, G. A. Reider, G. Chen, Y. You, L. Brézin, A. R. Harutyunyan, and T. F. Heinz, "Observation of rapid exciton-exciton annihilation in monolayer molybdenum disulfide," *Nano Letters*, vol. 14, no. 10, pp. 5625–5629, 2014.

[95] N. Kumar, Q. Cui, F. Ceballos, D. He, Y. Wang, and H. Zhao, "Exciton-exciton annihilation in $MoSe_2$ monolayers," *Phys. Rev. B*, vol. 89, no. 12, p. 125 427, 2014.

[96] T. Borzda, C. Gadermaier, N. Vujicic, P. Topolovsek, M. Borovsak, T. Mertelj, D. Viola, C. Manzoni, E. A. A. Pogna, D. Brida, M. R. Antognazza, F. Scotognella, G. Lanzani, G. Cerullo, and D. Mihailovic, "Charge photogeneration in few-layer MoS_2," *Adv. Funct. Mater.*, vol. 25, pp. 3351–3358, 2015.

[97] A. Chernikov, C. Ruppert, H. M. Hill, A. F. Rigosi, and T. F. Heinz, "Population inversion and giant bandgap renormalization in atomically thin WS_2 layers," *Nature Photonics*, vol. 9, pp. 466–470, 2015.

[98] A. Steinhoff, M. Rosner, F. Jahnke, T. O. Wehling, and C. Gies, "Influence of excited carriers on the optical and electronic properties of MoS_2," *Nano Letters*, vol. 14, no. 7, pp. 3743–3748, 2014.

[99] D. Vella, V. Vega-Mayoral, C. Gadermaier, N. Vujičić, T. Borzda, P. Topolovšek, M. Prijatelj, I. Tempra, E. A. A. Pogna, and G. Cerullo, "Femtosecond spectroscopy on MoS_2 flakes from liquid exfoliation: Surfactant independent exciton dynamics," *J. Nanophoton.*, vol. 10, no. 1, p. 012 508, 2015.

[100] V. Vega-Mayoral, D. Vella, T. Borzda, M. Prijatelj, I. Tempra, E. A. A. Pogna, S. D. Conte, P. Topolovšek, N. Vujičić, G. Cerullo, D. Mihailović, and C. Gadermaier, "Exciton and charge carrier dynamics in few-layer WS_2," *Nanoscale*, vol. 8, pp. 5428–5434, 2016.

[101] F. Schwierz, J. Pezoldta, and R. Granznera, "Two-dimensional materials and their prospects in transistor electronics," *Nanoscale*, vol. 7, pp. 8261–8283, 2015.

[102] W. Cao, J. Kang, S. Bertolazzi, A. Kis, and K. Banerjee, "Can 2d-nanocrystals extend the lifetime of floating-gate transistor based nonvolatile memory?" *IEEE Transactions on Electron Devices*, vol. 61, no. 10, pp. 3456–3464, 2014.

[103] J.-P. Colinge, "Multiple-gate SOIMOSFETs," *Solid-State Electronics*, vol. 48, no. 6, pp. 897–905, 2004.

[104] V. Podzorov, M. E. Gershenson, C. Kloc, R. Zeis, and E. Bucher, "High-mobility field-effect transistors based on transition metal dichalco- genides," *Appl. Phys. Lett.*, vol. 84, no. 17, pp. 3301–3303, 2004.

[105] A. V. Kretinin, Y. Cao, J. S. Tu, G. L. Yu, R. Jalil, K. S. Novoselov, S. J. Haigh, A. Gholinia, A. Mishchenko, M. Lozada, T. Georgiou, C. R. Woods, F. Withers, P. Blake, G. Eda, A. Wirsig, C. Hucho, K. Watanabe, T. Taniguchi, A. K. Geim, and R. V. Gorbachev, "Electronic properties of graphene encapsulated with different two-dimensional atomic crystals," *Nano Letters*, vol. 14, no. 6, pp. 3270–3276, 2014.

[106] D. Krasnozhon, D. Lembke, C. Nyffeler, Y. Leblebici, and A. Kis, "MoS_2 transistors operating at gigahertz frequencies," *Nano Letters*, vol. 14, no. 10, pp. 5905–5911, 2014.

[107] B. Radisavljevic, M. B. Whitwick, and A. Kis, "Small-signal amplifier based on single-layer MoS_2," *Appl. Phys. Lett.*, vol. 101, no. 4, p. 043 103, 2012.

[108] Z. Yin, H. Li, H. Li, L. Jiang, Y. Shi, Y. Sun, G. Lu, Q. Zhang, X. Chen, and H. Zhang, "Single-layer MoS_2 phototransistors," *ACS Nano*, vol. 6, no. 1, pp. 74–80, 2011.

[109] O. Lopez-Sanchez, E. A. Llado, V. Koman, A. F. I. Morral, A. Radenovic, and A. Kis, "Light generation and harvesting in a van der waals heterostructure," *Acs Nano*, vol. 8, no. 3, pp. 3042–3048, 2014.

[110] R. S. Sundaram, M. Engel, A. Lombardo, R. Krupke, A. C. Ferrari, P. Avouris, and M. Steiner, "Electroluminescence in single layer MoS_2," *Nano Letters*, vol. 13, no. 4, pp. 1416–1421, 2013.

[111] A. Allain and A. Kis, "Electron and hole mobilities in single-layer WSe_2," *ACS Nano*, vol. 8, no. 7, pp. 7180–7185, 2014.

[112] A. Castellanos-Gomez, M. Buscema, R. Molenaar, V. Singh, L. Janssen, H. S. J. van der Zant, and G. A. Steele, "Deterministic transfer of two-dimensional materials by all-dry viscoelastic stamping," *2D Materials*, vol. 1, no. 1, p. 011 002, 2014.

[113] Q. Yue, Z. Shao, S. Chang, and J. Li, "Adsorption of gas molecules on monolayer MoS_2 and effect of applied electric field," *Nanoscale Research Letters*, vol. 8, no. 425, 2013.

[114] C. Sire, S. Blonkowski, M. J. Gordon, and T. Baron, "Statistics of electrical breakdown field in HfO_2 and SiO_2 films from millimeter to nanometer length scales," *Appl. Phys. Lett*, vol. 91, no. 1, p. 242 905, 2007.

[115] B. Radisavljevic and A. Kis, "Mobility engineering and a metal–insulator transition in monolayer MoS_2," *Nature Materials*, vol. 12, pp. 815–820, 2013.

[116] B. W. H. Baugher, H. O. H. Churchill, Y. Yang, and P. Jarillo-Herrero, "Intrinsic electronic transport properties of high-quality monolayer and bilayer MoS_2," *Nano Letters*, vol. 13, no. 9, pp. 4212–4216, 2013.

[117] D. J. Late, B. Liu, H. S. Matte, V. P. Dravid, and C. N. Rao, "Hysteresis in single-layer MoS_2 field effect transistors," *ACS Nano*, vol. 6, no. 6, pp. 5635–5641, 2012.

[118] J. Cabanillas-González, G. Grancini, and G. Lanzani, "Pump-probe spectroscopy in organic semiconductors: Monitoring fundamental processes of relevance in opto-electronics," *Advanced materials*, vol. 23, pp. 5468–5485, 2011.

[119] I. Vaskivskyi, "Light induced phase transitions to hidden states in strongly correlated systems," PhD thesis, University of Ljubjana, Faculty of Mathematics and Physics, Ljubljana, Slovenia, 2015.

[120] C. Rulliere, *Femtosecond laser pulses principles and experiments*. New York: Springer, 2010.

[121] D. Viola, "Light harvesting and photoprotection of natural and artificial systems," PhD thesis, Molytechnique of Milan, Department of Physics, Milano, Italy, 2016.

[122] O. Svelto, *Principles of laser*. New York: Springer, 2010.

[123] D. Polli, L. Lüer, and G. Cerullo, "High-time-resolution pump-probe system with broadband detection for the study of time-domain vibrational dynamics," *Rev. Sci. Instrum*, vol. 78, no. 10, p. 103 108, 2007.

[124] T. Virgili, G. Grancini, E. Molotokaite, I. Suarez-Lopez, S. K. Rajendran, A. Liscio, V. Palermo, G. Lanzani, D. Polliac, and G. Cerullo, "Confocal ultrafast pump–probe spectroscopy: A new technique to explore nanoscale composites," *Nanoscale*, vol. 4, pp. 2219–2226, 2012.

[125] D. Vella, D. Ovchinnikov, D. Viola, D. Dumcenco, Y.-C. Kung, A. Kis, G. Cerullo, D. Mihailović, and C. Gadermaier, "Field induced charge separation in monolayer MoS_2," 2016, Submitted.

[126] A. Pospischil, M. M. Furchi, and T. Mueller, "Solar-energy conversion and light emission in an atomic monolayer p-n diode," *Nature Nanotechnology*, vol. 9, pp. 257–261, 2014.

[127] L. Britnell, R. M. Ribeiro, A. Eckmann, R. Jalil, B. D. Belle, A. Mishchenko, Y.-J. Kim, R. V. Gorbachev, T. Georgiou, S. V. Morozov, A. N. Grigorenko, A. K. Geim, C. Casiraghi, A. H. C. Neto, and K. S. Novoselov, "Strong light-matter interactions in heterostructures of atomically thin films," *Science*, vol. 340, no. 6138, pp. 1311–1314, 2013.

[128] D. Kozawa, R. Kumar, A. Carvalho, K. K. Amara, W. Zhao, S. Wang, M. Toh, R. M. Ribeiro, A. H. C. Neto, K. Matsuda, and G. Eda, "Photocarrier relaxation pathway in two-dimensional semiconducting transition metal dichalcogenides," *Nature Communications*, vol. 5, no. 4543, 2014.

[129] W. Graupner, G. Cerullo, G. Lanzani, M. Nisoli, E. J. W. List, G. Leising, and S. D. Silvestri, "Direct observation of ultrafast field-induced charge generation in ladder-type poly(para-phenylene)," *Phys. Rew. Lett.*, vol. 81, no. 15, p. 3259, 1998.

[130] W. Zhao, Z. Ghorannevis, L. Chu, M. Toh, C. K. P.-H. Tan, and G. Eda, "Evolution of electronic structure in atomically thin sheets of WS_2 and WSe_2," *ACS Nano*, vol. 7, no. 1, pp. 791–797, 2013.

[131] D. Sercombe, S. Schwarz, O. D. Pozo-Zamudio, F. Liu, B. J. Robinson, E. A. Chekhovich, I. I. Tartakovskii, O. Kolosov, and A. I. Tartakovskii, "Broadband ultrafast nonlinear absorption and nonlinear refraction of layered molybdenum dichalcogenide semiconductors," *Scientific Reports*, vol. 3, no. 3489, 2014.

[132] A. M. Jones, H. Yu, N. J. Ghimire, S. Wu, G. Aivazian, J. S. Ross, B. Zhao, J. Yan, D. G. Mandrus, D. Xiao, W. Yao, and X. Xu, "Optical generation of excitonic valley coherence in monolayer WSe_2," *Nature Nanotechnology*, vol. 8, no. 9, pp. 634–638, 2013.

[133] X. Hong, J. Kim, S.-F. Shi, Y. Zhang, C. Jin, Y. S. and Sefaattin Tongay, J. Wu, Y. Zhang, and F. Wang, "Ultrafast charge transfer in atomically thin MoS_2/WS_2," *Nature Nanotechnology*, vol. 9, pp. 682–686, 2014.

[134] Q.-C. Sun, L. Yadgarov, R. Rosentsveig, G. Seifert, R. Tenne, and J. L. Musfeldt, "Observation of a burstein-moss shift in rhenium-doped MoS_2 nanoparticles," *ACS Nano*, vol. 7, no. 4, pp. 3506–3511, 2013.

[135] D. Tsokkou, X. Yu, K. Sivula, and N. Banerji, "The role of excitons and free charges in the excited-state dynamics of solution-processed few-layer MoS_2 nanoflakes," *J. Phys. Chem. C*, vol. 120, no. 40, pp. 23 286–23 292, 2016.

[136] D. Vella, D. Ovchinnikov, N. Martino, V. Vega-Mayoral, D. Dumcenco, Y.-C. Kung, M.-R. Antognazza, A. Kis, G. Lanzani, D. Mihailović, and C. Gadermaier, "Electroabsorption in MoS_2," 2016, Online. DOI: arXiv:1607.00558.

[137] C. Gadermaier, F. Grasse, S. Perissinotto, M. Graf, F. Galbrecht, U. Scherf, E. J. W. List, and G. Lanzani, "Stark spectroscopy of excited-state transitions in a conjugated polymer," *Phys. Rew. Lett.*, vol. 100, no. 5, p. 057 401, 2008.

[138] B. Scharf, T. Frank, M. Gmitra, J. Fabian, I. Žutić, and V. Perebeinos, "Excitonic stark effect in MoS_2 monolayers," 2016, Online. DOI: arXiv:1606.03902.

[139] S. Haastrup, S. Latini, K. Bolotin, and K. S. Thygesen, "Stark shift and electric-field-induced dissociation of excitons in monolayer MoS_2 and hBN/MoS_2 heterostructures," *Phys. Rev. B*, vol. 94, no. 4, p. 041 401, 2016.

[140] V. I. Arkhipov, E. V. Emelianova, and H. Bässler, "Hot exciton dissociation in a conjugated polymer," *Phys. Rev. Lett.*, vol. 82, no. 6, p. 1321, 1999.

[141] L. Onsager, "Initial recombination of ions," *Phys. Rev.*, vol. 54, pp. 554–557, 1938.

[142] D. M. Pai and R. C. Enck, "Onsager mechanism of photogeneration in amorphous selenium," *Phys. Rev. B*, vol. 11, no. 12, pp. 5163–5174, 1975.

[143] E. J. Sie, A. J. Frenzel, Y.-H. Lee, J. Kong, and N. Gedik, "Intervalley biexcitons and many-body effects in monolayer MoS_2," *Phys. Rev. B*, vol. 92, no. 12, p. 125 417, 2015.

[144] K. Wang, J. Wang, J. Fan, M. Lotya, A. O'Neill, D. Fox, Y. Feng, X. Zhang, B. Jiang, Q. Zhao, H. Zhang, J. N. Coleman, L. Zhang, and W. J. Blau, "Ultrafast saturable absorption of two-dimensional MoS_2 nanosheets," *ACS Nano*, vol. 7, no. 10, pp. 9260–9267, 2013.

[145] K. Wang, Y. Feng, C. Chang, J. Zhan, C. W. Q. Zhao, J. N. Coleman, L. Zhang, W. J. Blauab, and J. Wang, "Broadband ultrafast nonlinear absorption and nonlinear refraction of layered molybdenum dichalcogenide semiconductors," *Nanoscale*, vol. 6, pp. 10 530–10 535, 2014.

[146] D. A. B. Miller, D. S. Chemla, T. C. Damen, A. C. Gossard, W. Wiegmann, T. H. Wood, and C. A. Burrus, "Band-edge electroabsorption in quantum well structures: The quantum-confined stark effect," *Phys. Rev. Lett.*, vol. 53, no. 22, pp. 2173–2176, 1984.

[147] G. T. Reed, G. Mashanovich, F. Y. Gardes, and D. J. Thomson, "Silicon optical modulators," *Nature Photonics*, vol. 4, no. 660, pp. 518–526, 2010.

[148] F. Xia, H. Wang, D. Xiao, M. Dubey, and A. Ramasubramaniam, "Two-dimensional material nanophotonics," *Nature Photonics*, vol. 8, pp. 899–907, 2014.

[149] X. Liu, T. Galfsky, Z. Sun, F. Xia, E.-c. Lin, Y.-H. Lee, S. Kéna-Cohen, and V. M. Menon, "Strong light-matter coupling in two-dimensional atomic crystals," *Nature Photonics*, vol. 9, pp. 30–34, 2015.

[150] E. J. Sie, J. W. McIver, Y.-H. Lee, L. Fu, J. Kong, and N. Gedik, "Valley selective optical stark effect in monolayer WS_2," *Nature Materials*, vol. 14, pp. 290–294, 2015.

[151] C. Zhang, H. Wang, W. Chan, C. Manolatou, and F. Rana, "Absorption of light by excitons and trions in monolayers of metal dichalcogenide MoS_2: Experiments and theory," *Phys. Rev. B*, vol. 89, no. 20, p. 205 436, 2014.

[152] B. Miller, E. Parzinger, A. Vernickel, A. W. Holleitner, and U. Wurstbauer, "Photogating of mono- and few-layer MoS_2," *Appl. Phys. Lett.*, vol. 106, no. 12, p. 122 103, 2015.

[153] C. Sciascia, N. Martino, T. Schuettfort, B. Watts, G. Grancini, M. R. Antognazza, M. Zavelani-Rossi, C. R. McNeill, and M. Caironi, "Sub-micrometer charge modulation microscopy of a high mobility polymeric n-channel field-effect transistor," *Adv. Mater.*, vol. 23, no. 43, pp. 5086–5090, 2011.

[154] N. Martino, D. Fazzi, C. Sciascia, A. Luzio, M. R. Antognazza, and M. Caironi, "Mapping orientational order of charge-probed domains in a semiconducting polymer," *ACS Nano*, vol. 8, no. 6, pp. 5968–5978, 2014.

[155] G. Weiser, "Modulation spectroscopy on anisotropic systems," *Surface Science*, vol. 37, pp. 175–197, 1973.

[156] K. L. Seyler, J. R. Schaibley, P. Gong, P. Rivera, A. M. J. and Sanfeng Wu, J. Yan, D. G. Mandrus, W. Yao, and X. Xu, "Electrical control of second-harmonic generation in a WSe_2 monolayer transistor," *Nature Nanotechnology*, vol. 10, pp. 407–411, 2015.

[157] H. J. Conley, B. Wang, J. I. Ziegler, R. F. HaglundJr., S. T. Pantelides, and K. I. Bolotin, "Bandgap engineering of strained monolayer and bilayer MoS_2," *Nano Leters*, vol. 13, no. 8, pp. 3626–3630, 2013.

[158] W. Wu, L. Wang, Y. Li, F. Zhang, L. Lin, S. Niu, D. Chenet, X. Zhang, Y. Hao, T. F. Heinz, J. Hone, and Z. L. Wang, "Piezoelectricity of single-atomic-layer MoS_2 for energy conversion and piezotronics," *Nature*, vol. 514, no. 8, pp. 470–474, 2014.

[159] T. Korn, S. Heydrich, M. Hirmer, J. Schmutzler, and C. Schüller, "Low-temperature photocarrier dynamics in monolayer MoS_2," *Appl. Phys. Lett.*, vol. 99, no. 10, p. 102 109, 2015.

[160] J. Bardeen and W. Shockley, "Deformation potentials and mobilities in non-polar crystals," *Phys. Rev.*, vol. 80, no. 1, pp. 72–80, 1950.

[161] N. S. Sariciftci, *Primary photoexcitations in conjugated polymers: Molecular exciton versus semiconductor band model*. London: World Scientific Publishing, 1997.

[162] N. Ma and D. Jena, "Charge scattering and mobility in atomically thin semiconductors," *Phys. Rev. X*, vol. 4, no. 1, p. 011 043, 2014.

[163] J. Klein, J. Wierzbowski, A. Regler, J. Becker, F. Heimbach, K. Müller, M. Kaniber, and J. J. Finley, "Stark effect spectroscopy of mono- and few-layer MoS_2," *Nano Letters*, vol. 16, no. 3, pp. 1554–1559, 2016.

[164] S. Ghatak, A. N. Pal, and A. Ghosh, "Nature of electronic states in atomically thin MoS_2 field-effect transistors," *ACS Nano*, vol. 5, no. 10, pp. 7707–7712, 2011.

[165] J. A. Schuller, S. Karaveli, T. Schiros, K. He, S. Y. and Ioannis Kymissis, J. Shan, and R. Zia, "Orientation of luminescent excitons in layered nanomaterials," *Nature Nanotechnology*, vol. 8, pp. 271–276, 2013.

[166] O. Ochedowski, K. Marinov, N. Scheuschner, A. Poloczek, B. K. Bussmann, J. Maultzsch, and M. Schleberger, "Effect of contaminations and surface preparation on the work function of single layer MoS_2," *Beilst. J. Nanotech.*, vol. 5, pp. 291–297. 2014.

[167] J. A. Lane, J. Rostalski, C. Giebeler, S. Martin, D. D. C. Bradley, and D. Meissner, "Electroabsorption studies of phthalocyanine/perylene solar cells," *Solar Energy Materials & Solar Cells*, vol. 63, pp. 3–13, 2000.

[168] A. Nawrocka and S. Krawczyk, "Electronic excited state of alizarin dye adsorbed on TiO_2 nanoparticles: A study by electroabsorption (stark effect) spectroscopy," *J. Phys. Chem. C*, vol. 112, no. 27, pp. 10 233–10 241, 2008.

[169] M. Liu, X. Yin, E. Ulin-Avila, B. Geng, T. Zentgraf, L. Ju, F. Wang, and X. Zhang, "A graphene-based broadband optical modulator," *Nature*, vol. 474, pp. 64–67, 2011.

[170] C. Haffner, W. Heni, Y. Fedoryshyn, J. Niegemann, A. Melikyan, D. L. E. and B. Baeuerle, Y. Salamin, A. Josten, U. Koch, C. Hoessbacher, F. Ducry, L. Juchli, A. Emboras, D. Hillerkuss, M. Kohl, L. R. Dalton, C. Hafner, and J. Leuthold, "All-plasmonic Mach-Zehnder modulator enabling optical high-speed communication at the microscale," *Nature Photonics*, vol. 9, pp. 525–528, 2015.

[171] R. R. Nair, P. Blake, A. N. Grigorenko, K. S. Novoselov, T. J. Booth, T. Stauber, N. M. R. Peres, and A. K. Geim, "Fine structure constant defines visual transparency of graphene," *Science*, vol. 320, p. 1308, 2008.

[172] G. Moody, C. K. Dass, K. Hao, C.-H. Chen, L.-J. Li, A. Singh, K. Tran, G. Clark, X. Xu, G. Berghäuser, E. Malic, A. Knorr, and X. Li, "Intrinsic homogeneous linewidth and broadening mechanisms of excitons in monolayer transition metal dichalcogenides," *Nature Communications*, vol. 6, no. 8315, 2015.

[173] S. Tongay, J. Zhou, C. Ataca, K. Lo, T. S. Matthews, J. Li, J. C. Grossman, and J. Wu, "Thermally driven crossover from indirect toward direct bandgap in 2d semiconductors: $MoSe_2$ versus MoS_2," *Nano Letters*, vol. 12, no. 11, pp. 5576–5580, 2012.

[174] M. Mohsin, D. Schall, M. Otto, A. Noculak, D. Neumaier, and H. Kurz, "Graphene based low insertion loss electro-absorption modulator on SOI waveguide," *Optics Express*, vol. 22, no. 12, pp. 15 292–15 297, 2014.

[175] X. Gan, Y. Gao, K. F. Mak, X. Yao, R.-J. Shiue, A. van der Zande, M. E. Trusheim, F. Hatami, T. F. Heinz, J. Hone, and D. Englund, "Controlling the spontaneous emission rate of monolayer MoS_2 in a photonic crystal nanocavity," *Appl. Phys. Lett.*, vol. 103, no. 18, p. 181 119, 2013.

[176] G. Eda and S. A. Maier, "Two-dimensional crystals: Managing light for optoelectronics," *ACS Nano*, vol. 7, no. 7, pp. 5660–5665, 2013.

[177] V. Nicolosi, M. Chhowalla, M. G. Kanatzidis, M. S. Strano, and J. N. Coleman, "Two-dimensional crystals: Managing light for optoelectronics," *Science*, vol. 340, no. 6139, p. 1 226 419, 2013.

[178] A. Castellanos-Gomez, "Why all the fuss about 2D semiconductors?" *Nature Photonics*, vol. 10, pp. 202–204, 2016.

[179] E. A. Obraztsova, L. Lüer, E. D. Obraztsova, A. I. Chernov, D. Brida, D. Polli, and G. Lanzani, "Effect of environment on ultrafast photoexcitation kinetics in single-wall carbon nanotubes," *Phys. Status Solidi B*, vol. 247, no. 11–12, pp. 2831–2834, 1950.

[180] F. Wang, G. Dukovic, E. Knoesel, L. E. Brus, and T. F. Heinz, "Observation of rapid auger recombination in optically excited semiconducting carbon nanotubes," *Phys. Rew. B*, vol. 70, no. 24, p. 241 403, 2004.

[181] A. L. Efros and M. Rosen, "Random telegraph signal in the photoluminescence intensity of a single quantum dot," *Phys. Rew. Lett.*, vol. 78, no. 6, pp. 1110–1113, 1997.

[182] P. A. Frantsuzov and R. A. Marcus, "Explanation of quantum dot blinking without the long-lived trap hypothesis," *Phys. Rew. B*, vol. 72, no. 15, p. 155 321, 2005.

[183] M. S. Strano, C. B. Huffman, V. C. Moore, M. J. O'Connell, E. H. Haroz, J. Hubbard, M. Miller, K. Rialon, C. Kittrell, S. Ramesh, R. H. Hauge, and R. E. Smalley, "Reversible, band-gap-selective protonation of single-walled carbon nanotubes in solution," *J. Phys. Chem. B*, vol. 107, no. 29, pp. 6979–6985, 2003.

[184] K. Matsuda, Y. Kanemitsu, K. Irie, T. Saiki, T. Someya, S. Miyauchi, and S. Maruyama, "Photoluminescence intermittency in an individual single-walled carbon nanotube at room temperature," *Appl. Phys. Lett.*, vol. 86, no. 12, p. 123 116, 2005.

[185] O. Kiowski, S. Lebedkin, F. Hennrich, and M. M. Kappes, "Single-walled carbon nanotubes show stable emission and simple photoluminescence spectra with weak excitation sidebands at cryogenic temperatures," *Phys. Rev. B*, vol. 76, no. 7, p. 075 422, 2007.

[186] T. Koyama, S. Yoshimitsu, Y. Miyata, H. Shinohara, H. Kishida, and A. Nakamura, "Transient absorption kinetics associated with higher exciton states in semiconducting single-walled carbon nanotubes: Relaxation of excitons and phonons," *J. Phys. Chem. C*, vol. 117, no. 39, pp. 20 289–20 299, 2013.

[187] G. Soavi, F. Scotognella, D. Brida, T. Hefner, F. Späth, M. R. Antognazza, T. Hertel, G. Lanzani, and G. Cerullo, "Ultrafast charge photogeneration in semiconducting carbon nanotubes," *J. Phys. Chem. C*, vol. 117, no. 20, pp. 10 849–10 855, 2013.

[188] J. Zheng, H. Zhang, S. Dong, Y. Liu, C. T. Nai, H. S. Shin, H. Y. Jeong, B. Liu, and K. P. Loh, "High yield exfoliation of two-dimensional chalcogenides using sodium naphthalenide," *Nature Communications*, vol. 5, no. 2995, 2014.

[189] W. M. R. Divigalpitiya, S. R. Morrison, and R. Frindt, "Thin oriented films of molybdenum disulphide," *Thin Solid Films*, vol. 186, no. 1, pp. 177–192, 1990.

[190] D. Y. Qiu, F. H. da Jornada, and S. G. Louie, "Optical spectrum of MoS_2: Many-body effects and diversity of exciton states," *Phys. Rev. Lett.*, vol. 111, no. 21, p. 216 805, 2013.

[191] H. Li, Q. Zhang, C. C. R. Yap, B. K. Tay, T. H. T. Edwin, A. Olivier, and D. Baillargeat, "From bulk to monolayer MoS_2: Evolution of raman scattering," *Adv. Funct. Mater.*, vol. 22, no. 4543, pp. 1385–1390, 2012.

[192] C. Gadermaier, E. Menna, M. Meneghetti, W. J. Kennedy, Z. V. Vardeny, and G. Lanzani, "Long-lived charged states in single-walled carbon nanotubes," *Nano Letters*, vol. 6, no. 2, pp. 301–305, 2006.

[193] G. Tränkle, E. Lach, A. Forchel, F. Scholz, C. Ell, H. Haug, G. Weimann, G. Griffiths, H. Kroemer, and S. Subbanna, "General relation between band-gap renormalization and carrier density in two-dimensional electron-hole plasmas," *Phys. Rev. B*, vol. 36, no. 12, pp. 6712–6714, 1987.

[194] C. Georgi, N. Hartmann, T. Gokus, A. A. Green, M. C. Hersam, and A. Hartschuh, "Photoinduced luminescence blinking and bleaching in individual single-walled carbon nanotubes," *Chemphyschem*, vol. 9, no. 10, pp. 1460–1464, 2008.

[195] A. F. Clements, J. E. Haley, A. M. Urbas, A. Kost, R. D. Rauh, J. F. Bertone, F. Wang, B. M. Wiers, D. Gao, T. S. Stefanik, A. G. Mott, and D. M. Mackie, "Photophysical properties of C_{60} colloids suspended in water with triton X-100 surfactant: Excited-state properties with femtosecond resolution," *J. Phys. Chem. A*, vol. 113, no. 23, pp. 6437–6445, 2009.

Bibliography

Publications Related to the Thesis

Journal Articles

D. Vella, V. Vega-Mayoral, C. Gadermaier, N. Vujičić, T. Borzda, P. Topolovšek, M. Prijatelj, I. Tempra, E. A. A. Pogna, and G. Cerullo, "Femtosecond spectroscopy on MoS_2 flakes from liquid exfoliation: Surfactant independent exciton dynamics," *J. Nanophoton.*, vol. 10, no. 1, p. 012 508, 2015.

V. Vega-Mayoral, D. Vella, T. Borzda, M. Prijatelj, I. Tempra, E. A. A. Pogna, S. D. Conte, P. Topolovšek, N. Vujičić, G. Cerullo, D. Mihailović, and C. Gadermaier, "Exciton and charge carrier dynamics in few-layer WS_2," *Nanoscale*, vol. 8, pp. 5428–5434, 2016.

D. Vella, D. Ovchinnikov, N. Martino, V. Vega-Mayoral, D. Dumcenco, Y.-C. Kung, M.-R. Antognazza, A. Kis, G. Lanzani, D. Mihailović, and C. Gadermaier, "Electroabsorption in MoS_2," 2016, Online. DOI: `arXiv:1607.00558`.

D. Vella, D. Ovchinnikov, D. Viola, D. Dumcenco, Y.-C. Kung, A. Kis, G. Cerullo, D. Mihailović, and C. Gadermaier, "Field induced charge separation in monolayer MoS_2," 2016, Submitted.

Patents

D. Vella, C. Gadermaier, D. Ovchinnikov, A. Kis, M.-R. Antognazza, and G. Lanzani, "Electro-optical modulator based on a layered semiconductor crystal structure," *Patent Application GB*, no. 1600549.8, 2016.

Conference Contribution

Conference Talk

D. Vella, D. Ovchinnikov, N. Martino, V. Vega-Mayoral, D. Dumcenco, Y.-C. Kung, M.-R. Antognazza, A. Kis, G. Lanzani, D. Mihailović, and C. Gadermaier, "Giant unconventional electroabsorption in monolayer MoS_2," in *Flatlands: Beyond graphene*, Bled, Slovenia, July 5–8, 2016.

D. Vella, D. Ovchinnikov, D. Dumcenco, N. Martino, M.-R. Antognazza, A. Kis, G. Lanzani, D. Mihailović, and C. Gadermaier, "Giant liner quantum confined stark effect in monolayer MoS_2," in *2nd International Conference Functional Integrated Systems, nanoFIS 2016*, Graz, Austria, June 27–29, 2016.

D. Vella, V. Vega-Mayoral, T. Borzda, D. Ovchinnikov, D. Dumcenco, Y.-C. Kung, E. A. A. Pogna, D. Viola, G. Cerullo, A. Kis, D. Mihailović, and C. Gadermaier., "Field induced dissociation of excitons in MoS_2 monolayer," in *Nonequilibrium phenomena in complex matter: New observations and new theories*, Ambrož,Krvavec, Slovenia, December 13–16, 2015.

Conference Poster

D. Vella, V. Vega-Mayoral, T. Borzda, D. Ovchinnikov, D. Dumcenco, Y.-C. Kung, E. A. A. Pogna, D. Viola, G. Cerullo, A. Kis, D. Mihailović, and C. Gadermaier., "Field induced dissociation of excitons in MoS_2 monolayer," in *Molecular nanostructures: Program, XXXth International Winterschool Euroconference on Electronic Properties of Novel Materials, IWEPNM 2016*, Kirchberg in Tirol, Austria, February 13–20, 2016.

D. Vella, V. Vega-Mayoral, T. Borzda, N. Vujičić, P. Topolovšek, M. Prijatelj, C. Gadermaier, and D. Mihailović., "Femtosecond spectroscopy on MoS_2 films: Effects of synthesis on the electron dynamics," in *Four International Workshop o Nanocarbon Photonics and Optoelectronics*, Polviärvi, Joensuu, Finland, 28 July–1 August, 2014.

D. Vella, V. Vega-Mayoral, T. Borzda, N. Vujičić, P. Topolovšek, M. Prijatelj, C. Gadermaier, I. Tempra, G. Cerullo, and D. Mihailović., "Femtosecond spectroscopy on MoS_2 films: Effects of synthesis on the electron dynamics," in *Flatlands: Beyond graphene*, Dublin, Ireland, 9–11 June 2014, 2014.

Biography

Daniele Vella received his MSc degree in Biomedical Engineering from the University of Pisa in 2013 by presenting his thesis: Near-field optical microscopy on carbon nanotubes based nanosystems. The work was carried out at the Department of Physics E. Fermi (Pisa) where, at a later time, he carried on and collaborated on the realization of a high resolution and high sensitivity confocal-scanning near-field optical microscope. During that period he was involved in an industrial project funded by Continental Automotive Italy S.p.A concerning roughness analysis of complex shaped samples and software development for computing of rough nano-/microstructured surfaces. In October 2013, he joined C. Gadermaier's group at the Jožef Stefan Institute (Department of Complex Matter), Slovenia, as a PhD Marie Curie fellow (ITN Network MoWSeS). His research interests include optical and electronic properties of nanomaterials with specific attention to femtosecond, electric field modulation and Raman spectroscopy on thin films and devices based on two-dimensional semiconducting transition metal dichalcogenides. He spent a part of his PhD in the group of Prof. A. Kis (École Polytechnique Fédérale de Lausanne), from where he started his main research activities on Stark effect and ultrafast generation of charges in single layer MoS_2 field effect transistors.